

Overheating Prediction and Management of Lithium-Ion Batteries

by

Rui Zhao

A thesis submitted to the Faculty of Graduate and Postdoctoral Affairs in partial fulfillment of the requirements for the degree of

Doctor of Philosophy

in

Mechanical Engineering

Carleton University

Ottawa, Ontario

© 2018

Rui Zhao

Abstract

Lithium-ion (Li-ion) batteries have been widely used in portable devices and electric vehicles as power sources due to their high energy density, long lifespan, no memory effect, and low self-discharge rate. However, when overheating occurs, the performance, reliability, durability, and safety of Li-ion batteries can be seriously deteriorated.

Overheating of Li-ion batteries typically takes place during normal high-rate discharges and abnormal discharges such as short circuits. For high-rate discharges, the parasitic heat generation of Li-ion batteries can accelerate the capacity fading. In abnormal discharges, the overheating issue becomes more severe, and the battery temperature could even reach the threshold for exothermic reactions and trigger thermal runaway.

In this thesis, phase change material (PCM)-based and heat pipe-based battery thermal management (BTM) systems were designed to dissipate the heat generated by cylindrical and prismatic batteries respectively during normal discharges. The proposed PCM-based BTM system was developed through innovatively embedding PCM cores in the cylindrical battery centers. Compared to conventional PCM-based BTM systems using PCM externally to batteries, the proposed design consumes less PCM while achieves better cooling effects. For prismatic batteries, ultra-thin heat pipes were sandwiched between the batteries to manage their temperature rises. The implementation of heat pipes notably alleviates the heat accumulation in battery packs, and the cooling performance can be further enhanced when an evaporative cooling strategy is applied to dissipate the heat.

Regarding the more severe overheating issues caused by abnormal discharges, internal and external short circuit experiments were performed on Li-ion batteries, and a modified electrochemical-thermal coupling model was developed to simulate the short circuits. Good correlations were found between experimental and numerical results for non-thermal runaway batteries. For batteries with thermal runaways, the model can predict whether and when the thermal runaway will occur. Besides, strategies that can hinder thermal runaway and its propagation in battery packs were also investigated and verified through experiments.

Acknowledgments

First and foremost, I would like to express my deepest gratitude to my supervisors, Dr. LIU Jie and GU Junjie, for their enthusiastic supervision and patient guidance. This work could not have been accomplished without their knowledge, support, and encouragement.

I would like to express my great appreciation to my PhD committee members, Dr. Xianguo Li (University of Waterloo), Dr. Yuu Ono, Dr. Fidel Khouli, Dr. Steve Ulrich, and Dr. Patrick Dumond (University of Ottawa), for their instructive suggestions and help.

I would like to thank the technical support provided by Mr. Alex Proctor and Mr. David Raude during my experiment setup.

Many thanks to my friends, Chengchao Liang, Zicheng Wei, Long Zhai, Doma Slaman, Menggu He, Kun Zhuang, Yu Ji, Yu Zhang, Zelig Li, Qianyue Qian, Qingfeng Lou, and many others for their friendship and help.

I am indebted, forever, to my parents and my wife's family for their endless understanding, support, and encouragement. I would also like to deeply thank my my wife, Sijie, for her tremendous support and love. I would finally thank my daughter, Annie. I hope you can enjoy your life and be happy. I will love Sijie and Annie forever.

Table of Contents

Abstract.....	ii
Acknowledgments	iii
List of Figures	vii
List of Tables	xi
Nomenclature	xii
Chapter 1. Introduction	1
1.1 Overview and Related Issues.....	1
1.2 Objectives	4
1.3 Thesis Outline and Contributions	5
Chapter 2. Background and Literature Review	7
2.1 Introduction to lithium-ion (Li-ion) Battery.....	7
2.2 Energy Balance in Li-ion Battery.....	9
2.2.1 Heat Dissipation	9
2.2.2 Heat Generation.....	10
2.3 Thermal Management of Normally Discharged Batteries.....	12
2.3.1 Overheating Issues of Normally Discharged Batteries	12
2.3.2 Battery Thermal Management Systems	13
2.3.2.1 Air Cooling.....	13
2.3.2.2 Liquid Cooling	15
2.3.2.3 Heat Pipe Cooling	16
2.3.2.4 Phase Change Material (PCM) Cooling.....	18
2.4 Research on Abnormally Discharged Batteries.....	24
2.4.1 Overheating Issues of Abnormally Discharged Batteries	24
2.4.2 Studies on Abnormally Discharged Batteries	25
Chapter 3. Development of a PCM-Based BTM System for Normally Discharged Cylindrical Li-ion Batteries.....	27
3.1 Overview	27
3.2 Battery and Battery Pack Designs	27

3.3	Experiment and Thermal Model.....	31
3.4	Results and Discussion.....	36
3.4.1	TTC Tests for Model Validation.....	36
3.4.2	Simulations on a Single 18650 Li-ion Battery.....	39
3.4.3	Solidification of the PCM Core.....	43
3.4.4	Core Cooling vs. External Cooling.....	46
3.5	Summary.....	48
Chapter 4. Optimization of the PCM-Based BTM System on Li-ion Battery Packs		50
4.1.	Overview	50
4.2.	Battery Pack Description.....	50
4.3.	Model Setup.....	52
4.4.	Results and Discussion.....	52
4.4.1	Battery Performance Index.....	52
4.4.2	PCM Core Size.....	53
4.4.3	PCM Core Size Distribution	55
4.4.4	Hybrid Cooling System.....	60
4.4.5	Space Utilization in Battery Modules	63
4.5.	Summary.....	64
Chapter 5. Development of a Heat Pipe-Based BTM System for Normally Discharged Prismatic Li-ion Batteries		66
5.1	Overview	66
5.2	Experimental Setup.....	66
5.3	Results and Discussion.....	71
5.3.1	Temperature Control	71
5.3.2	Temperature Difference	73
5.3.3	Large Battery Pack Cooling	76
5.4	Summary.....	79

Chapter 6. Development of a Numerical Model for Simulating Abnormally Discharged Batteries.....	80
6.1 Overview	80
6.2 Experimental Setup.....	80
6.3 Model Description	81
6.3.1 Electrochemical Model	82
6.3.2 Thermal Model.....	86
6.4 Results and Discussion	89
6.4.1 External Short Circuit.....	89
6.4.2 Nail Penetration.....	91
6.5 Summary.....	97
Chapter 7. A Comprehensive Study on Li-ion Battery Nail Penetrations and the Possible Solutions.....	99
7.1 Overview	99
7.2 Experiments	99
7.3 Results and Discussion	102
7.3.1 Simulations on Batteries of Difference Capacities	102
7.3.2 Effects of Battery Resistance and Nail Diameter	105
7.3.3 Comparison of Strategies to Prevent Thermal Runaway	107
7.3.3.1 Decrease State of Charge	107
7.3.3.2 Improve Heat Dissipation.....	110
7.3.3.3 Increase Contact Resistance	115
7.4 Summary.....	117
Chapter 8. Conclusions and Future Work	119
8.1 Conclusions	119
8.2 Future Work.....	121
Bibliography	122

List of Figures

Figure 2.1. Internal structures of a) a prismatic battery and b) a cylindrical battery.....	8
Figure 2.2. Schematic illustrations of a) an electrochemical reaction cell, b) a prismatic battery, and c) a cylindrical battery.....	8
Figure 2.3. Selected characteristics and recent research interests in PCM-based BTM system for Li-ion battery.....	19
Figure 3.1. 4-layer battery packs equipped with a) the proposed internal PCM-based BTM system, and b) the conventional external PCM-based system.....	28
Figure 3.2. Pictures of a disassembled 18650 Li-ion battery and a schematic of the PCM core cooling design.	29
Figure 3.3. Photographs of the thermal test cell and its components, as well as the test setup.	32
Figure 3.4. Comparisons of the experimental and simulated temperatures during the TTC tests at heating powers of a) 1.43 W and b) 3.27 W.	38
Figure 3.5. Simulation results of the single 18650 Li-ion battery: temperature contours of a) the original battery and b) the battery with a 1.25 mm PCM core at the end of the 2.5 A discharges; temperature curves of the battery embedding PCM core of different sizes during discharges at currents of c) 2.5 A and d) 5 A.	40
Figure 3.6. A plot of the capacity ratio against the PCM core radius.....	41
Figure 3.7. The comparison of the temperature curves of a single Li-ion battery embedding pure PCM and PCM/EG composite cores during a 2.5 A discharge.....	42
Figure 3.8. The liquid fractions of a) pure PCM and b) PCM/EG composite at the assigned times during the 2.5 A discharge.	43
Figure 3.9. Experimentally recorded PCM core temperature curves of the TTC filled with a) n-octadecane and b) n-eicosane during the 3.27 W tests under different cooling conditions.....	45
Figure 3.10. Cycle tests of the n-eicosane filled TTC under heating powers of a) 1.43 W and b) 3.27 W.....	46
Figure 3.11. Maximum temperature and temperature difference curves of the 4-layer battery pack equipped with internal and external BTM systems.....	47

Figure 4.1. a) Schematic illustration of a passively cooled 40-cell battery pack; b) Schematic illustration of a hybrid cooling design for the battery pack.	51
Figure 4.2. Maximum temperature profiles of the battery pack embedded with PCM cores of different sizes during a) 0.96 C and b) 1.92 C discharges.....	54
Figure 4.3. Plots of the maximum and minimum temperatures, as well as the temperature differences of the batteries embedded with PCM cores of different sizes at the end of a 1.92 C discharge.....	55
Figure 4.4. Temperature contours of the battery pack using different core size combinations at the end of a 1.92 C discharge under natural convection condition.	56
Figure 4.5. a) The PCM volume ratio of different core size combinations to the combination with uniform 3.8 mm cores; The temperature difference curves between points A and B in the battery pack using different core size combinations during the 5 A discharge under convective cooling with h of b) $1 \text{ W m}^{-2} \text{ K}^{-1}$, and c) $10 \text{ W m}^{-2} \text{ K}^{-1}$	58
Figure 4.6. The liquid fraction of PCM cores (2.8 mm & 4.8 mm combination) at the end of a 1.92 C discharge under natural convection condition.....	59
Figure 4.7. The maximum temperature and temperature difference profiles of the modified battery pack during a 1.92 C discharge during forced convective cooling conditions.	60
Figure 4.8. Comparisons of the temperature and temperature difference profiles of the original battery pack and the PCM-embedded battery pack cooled by air.	61
Figure 4.9. The temperature contours of the cells in a) the original battery pack and d) the modified battery pack; The temperature contours of the air in b) the original battery pack and e) the modified battery pack; The velocity contours of the air in c) the original battery pack and f) the modified battery pack.....	62
Figure 4.10. Temperature profiles of the battery pack cooled by the hybrid cooling system during a 1.92 C discharge.	63
Figure 5.1. Photographs of the a) heat pipe 2 and b) its internal structure.	67
Figure 5.2. a) Schematic illustration of a battery pack sandwiched by heat pipes; b) Locations where the battery temperatures were measured.	69
Figure 5.3. Schematic illustrations of four heat pipe-based BTM systems, a) horizontal heat pipes with cooling fan; b) vertical heat pipes with cooling fan; c) heat pipes in a thermostat water bath and d) horizontal heat pipes with wet cooling.	70

Figure 5.4. Temperature curves of the 3 Ah battery pack cooled by different approaches during the 3 C discharges.....	72
Figure 5.5. Temperature rises of the 3 Ah battery pack cooled through different approaches at the assigned discharge rates.	73
Figure 5.6. Temperature difference curves of the 3 Ah battery pack cooled through different approaches during the 3 C discharges.....	74
Figure 5.7. Temperature difference curves of the inner battery in the 3 Ah battery pack cooled through different approaches during the 3 C discharges.....	75
Figure 5.8. The maximum and minimum temperature curves of the 8 Ah battery pack cooled through natural convection and wet cooling approach during 10 A discharges. ..	76
Figure 5.9. a) Pack-level and b) battery-level temperature difference curves of the 8 Ah battery pack cooled through natural convection and wet cooling approach during 10 A discharges.....	77
Figure 5.10. Temperature curves of the 8Ah battery cooled through a) natural convection and b) wet cooling approaches during cycle tests.....	78
Figure 6.1. Schematics of the nail penetration model: a) A thermal model that includes heat sources from both the battery and the nail location; b) A pseudo-2D electrochemical model.	82
Figure 6.2. Photograph of nailed batteries used for determining nail site resistances.....	88
Figure 6.3. Temperature and voltage curves of a) 0.65 Ah and b) 1.2 Ah batteries externally shorted in ambient conditions.	90
Figure 6.4. Simulated temperature curves of the externally shorted 0.65 Ah battery.	91
Figure 6.5. Comparison of the experimental and simulated temperature curves of the nailed 0.65 Ah battery.....	92
Figure 6.6. The simulated electrode current density of the nailed 0.65 Ah battery.....	92
Figure 6.7. The temperature contours of the nailed 0.65 Ah battery at different times after penetration.....	93
Figure 6.8. Experimentally recorded temperature and voltage curves of the 1.2 Ah batteries that a) did not experience and b) experienced thermal runaway during nail tests.	94
Figure 6.9. Simulated temperature and voltage curves of the nailed 1.2 Ah battery.....	95

Figure 6.10. Temperature and voltage curves of the 5 Ah batteries during nail penetration tests: thick electrode battery (battery No. 3) in a) experiment and b) simulation, and thin electrode battery (battery No. 4) in c) experiment and d) simulation. 96

Figure 7.1. A plot of contact resistance R_n vs. contact area between nail and battery. .. 101

Figure 7.2. Comparison of the a) temperature, b) battery heat source, and c) boundary heat source curves of the three batteries during the 1.8 mm-nail penetration simulations..... 104

Figure 7.3. The maximum temperature contours of the a) 3 Ah and b) 5 Ah batteries in penetration simulations using different nail diameters and battery internal resistance. . 106

Figure 7.4. a) The maximum temperatures of the 3 Ah and 5 Ah batteries with different SOC's during the 1.8 mm-nail penetration simulations; The boundary heat sources of the b) 3 Ah, and c) 5 Ah batteries at different SOC's. 109

Figure 7.5. Plots of the maximum and surface temperatures of the 3 Ah and 5 Ah batteries under different cooling conditions during 1.8-mm nail penetration simulations..... 111

Figure 7.6. Temperature and voltage curves of the a) 0.65 Ah, b) 1.2 Ah, and c) 5 Ah batteries during nail penetration tests in a hydrogel-based BTM system. 112

Figure 7.7. Photographs of the 3 Ah battery pack a) before and b) after thermal runaway propagation test. 113

Figure 7.8. Temperature and voltage curves of a) the 3 Ah battery pack nailed in ambient and b) the 8 Ah battery pack nailed in a hydrogel-based BTM system. 114

Figure 7.9. a) The maximum temperatures of the 3 Ah and 5 Ah batteries in penetrations using different contact resistances; The b) temperature, c) voltage, and d) C-rate curves of the 3 Ah battery during penetrations using different contact resistances. 117

List of Tables

Table 2.1. Summary of the innovative heat pipe-based BTM system for Li-ion batteries.	17
Table 2.2. Paraffin with suitable melting temperatures for Li-ion battery thermal management.	20
Table 2.3. Summary of research on PCM-based BTM systems.	23
Table 2.4. A few notable Li-ion battery induced accidents in recent years.	24
Table 3.1. Physical properties of n-octadecane, n-eicosane, and PCM/EG composite [107, 109, 140].	30
Table 3.2. Specifications and physical properties of the thermal test cell.	31
Table 3.3. Specifications and parameters of the Samsung 18650 LiCoO ₂ battery.	34
Table 3.4. Summary of the experimental results and the calculated heat generations of the 18650-type battery.	35
Table 3.5. Comparisons of the performance indicators of core and external cooling systems.	48
Table 4.1. Summary of the battery performance data of selected battery packs.	64
Table 5.1. Specifications of the 3 Ah and 8 Ah batteries.	68
Table 5.2. Specifications of heat pipes and thermal pads.	68
Table 5.3. Summary of the experimental results of the 3 Ah battery pack.	75
Table 6.1. Specifications of batteries used in short circuit tests.	81
Table 6.2. Electrochemical and thermal parameters of the batteries used in the simulation.	85
Table 6.3. Battery parameters used in the nail penetration model.	88
Table 7.1. Specifications of LiCoO ₂ batteries used in short circuit simulations or tests*.	101
Table 7.2. The stoichiometry of 3 Ah and 5 Ah batteries at the assigned SOCs.	108

Nomenclature

a_s	active surface area per electrode unit volume, $\text{m}^2 \text{m}^{-3}$
A	area, m^2
c	volume-averaged concentration of lithium in a phase, mol m^{-3}
$c_{s,max}$	maximum concentration of lithium in solid phase, mol m^{-3}
$c_{s,0}$	initial concentration of lithium in solid phase, mol m^{-3}
c_p	specific heat capacity of component inside cell, $\text{J kg}^{-1} \text{K}^{-1}$
D	diffusion coefficient of lithium species, $\text{m}^2 \text{s}$
E_{act}^Ψ	Activation energy, J mol^{-1}
F	Faraday's constant, 96487 C mol^{-1}
h	height, m
h	convective heat transfer coefficient, $\text{W m}^{-2} \text{K}^{-1}$
h_f	latent heat, kJ kg^{-1}
I	current, A
i	current density, A m^{-3}
j^{Li}	reaction current density, A m^{-3}
k	conductivity of different components inside cell, $\text{W m}^{-1} \text{K}^{-1}$
k	ionic conductivity, S m^{-1}
l_a	thickness of aluminum foil, m
l_c	thickness of copper foil, m
l_n	thickness of negative electrode, m

l_s	thickness of separator, m
l_p	thickness of positive electrode, m
l	thickness of electrochemical cell, m
m	battery mass, g
P	Average heat generation rate, W
Q	Overall heat generation, J
q	volumetric heat generation rate, W m ⁻³
q_r	volumetric reaction heat generation rate, W m ⁻³
q_e	volumetric reversible heat generation rate, W m ⁻³
q_j	volumetric ohmic heat generation rate, W m ⁻³
q_n	volumetric nail location heat generation rate, W m ⁻³
r	radius or radial coordinate, m
R	universal gas constant, 8.3143 J mol ⁻¹ K ⁻¹
R_b	bulk resistance of battery, mΩ
R_n	nail location resistance, mΩ
R_s	radius of solid particles, m
t	time, s
t_+^0	transference number of lithium-ion with respect to the velocity of solvent
T	temperature, K
U	open circuit potential, V
U_{ref}	reference open-circuit potential of an electrode reaction, V
V	volume, m ³

V	working voltage, V
x	x coordinate
x	negative electrode solid phase stoichiometry
y	positive electrode solid phase stoichiometry

Greek symbols

α	volumetric battery capacity, mAh m ⁻³
ε	volume fraction or porosity of a phase
ε	emissivity
η	surface over-potential of an electrode reaction, V
κ	reaction rate constant
σ	conductivity of solid active materials in an electrode, S cm ⁻¹
σ	Stefan-Boltzmann constant, 5.67×10^{-8} W m ⁻² K ⁻⁴
ρ	density of the battery, kg m ⁻³
θ	capacity ratio
γ	liquid fraction
ξ	Space utilization ratio
Φ	electrical potential in a phase, V
Ψ	A general property

Subscripts

amb	ambient
-------	---------

<i>c</i>	coolant
<i>dis</i>	discharge
<i>e</i>	electrolyte phase
<i>f</i>	conductive filler additive
<i>l</i>	liquid phase
<i>m</i>	melting point
<i>o</i>	initial state
<i>p</i>	polymer phase or in parallel
<i>ref</i>	with respect to a reference state
<i>s</i>	solid phase or in series
<i>s</i>	solid state or solidification

Superscripts

eff	effective value
-----	-----------------

Acronyms

ARC	accelerating rate calorimetry
BTM	battery thermal management
DSC	differential scanning calorimetry
EG	expanded graphite
EV	electric vehicle
NSE	normalized specific energy

PAAS	sodium polyacrylate
PCM	phase change material
PCS	phase change sludge
PHEV	plug-in hybrid electric vehicle
SE	specific energy
SEI	solid electrolyte interface
SOC	state of charge
TTC	thermal test cell

Chapter 1. Introduction

1.1 Overview and Related Issues

The currently available battery electric vehicles (EV) in North America have one thing in common, they employ the lithium-ion (Li-ion) batteries as their power sources. Since the first commercialization in 1991, Li-ion battery technology has shown continuously increasing market share and has attracted a significant amount of research interests in producing batteries with higher energy density, longer life, and lower costs [1]. Although a large amount of power can be supplied from a compact Li-ion battery system, the parasitic heat generation at high discharge rates and the heat surge during short circuits can degrade battery performance and even lead to thermal runaway.

Generally, an operating temperature range between 15°C and 35°C and a temperature difference within 5°C are essential for Li-ion batteries to perform soundly and to have a long service life [2]. However, the heat generation of Li-ion batteries, especially at high rates, can significantly accelerate the temperature elevation and aggravate the temperature nonuniformity of batteries, and the situation is made more severe when the batteries are compactly packed, which may significantly shorten the lifespan of batteries [3, 4]. To control the temperature rise and temperature gradient of batteries within allowable ranges, thus improving the stability and electrochemical performance of the battery system, the battery thermal management (BTM) system is an indispensable component.

Over the past several years, many BTM approaches have been proposed and studied [5]. They can be classified into two categories: active and passive BTM systems. Active BTM systems are typically achieved by using fans or pumps to circulate cooling mediums, such as air [6-10] and liquid [11, 12] so that the heat can be extracted from the battery packs. Passive cooling systems make good use of the physical properties of various cooling mediums implemented between neighboring batteries to absorb the heat released during operation, thereby keeping the battery temperature at a relatively low level. The present passive cooling systems mainly rely on water [13-15] or phase change materials (PCM) [16-20] for heat absorption.

Each BTM system has its advantages in coexistence with disadvantages. For instance, because of the strengths such as the direct access, low viscosity, and light weight of air, as well as the simplicity and low cost of the BTM system, air cooling is one of the most commonly adopted BTM systems in our daily life. However, it still has potential weaknesses including blocked cooling channels or inlets, intake of debris, malfunction of the cooling fan, relatively large temperature gradient during aggressive discharges, etc. Current research on air cooled systems is mainly focused on the optimization of the battery layout and flow configuration to achieve better cooling performance, with less emphasis on the space utilization (energy density) of the entire battery module, which in fact is of great importance for applications with rigorous space constraints.

Another active BTM system, the heat pipe-based BTM system, is also extensively studied in these years. It can be classified into air-cooled [21, 22] and water-cooled [23] systems, according to the cooling strategies applied at the condenser side of the heat pipe. Compared to direct air or water cooling, the heat pipe-based BTM system avoids the direct contact between batteries and cooling mediums, and its high thermal conductivity can ensure even temperature distributions inside battery packs. However, its average cooling potential and relatively high cost make this cooling design less competitive compared to other BTM systems.

As for passive BTM systems, the PCM-based BTM system is extensively studied. It manages the heat generated from batteries by using the latent heat of the PCM stored at the solid-liquid phase transition stage. Compared to the active BTM system, the PCM-based BTM system is simple in structural design and has no parasitic power consumption, but it will add extra weight to the energy storage system. Therefore, the PCM cooling system should be designed using a minimal amount of PCM to manage the temperature of a battery system in an allowable range. Initially, PCM was directly used to envelop batteries in BTM systems [16]. However, several works revealed that the low thermal conductivity of PCM could substantially constrain the thorough exertion of its cooling potential. Thus, expanded graphite (EG) was produced as matrices to contain the PCM to increase the thermal conductivity of entire cooling systems [24, 25]. One merit of this composite is that the liquid state PCM could be immobilized inside the matrix with the strong capillary force

generated by the EG matrix, thus avoiding leaking problems. In practice, this strategy has several limitations. For examples, it was found that at least 30 wt.% EG is required to maintain leakage at a low level, which substantially reduces the latent heat of the PCM cooling system [26, 27]. Also, the manufacturing process and the potential fracture of the PCM composite could increase initial and maintenance costs of the BTM system.

The above mentioned BTM systems can generally handle the overheating of battery packs during normal charges/discharges. However, in more severe overheating conditions, such as during abnormal discharges typical of short circuits, most of the BTM systems are incapable of suppressing the rapid-released heat. Short circuits happen when positive and negative electrodes are electrically contacted due to mechanical abuse, manufacturing defect, or other reasons, and a great amount of heat can be generated in a very short time. If the heat is not dissipated efficiently, the battery temperature will exceed a critical point, above which the electrolyte, active materials, and solid electrolyte interface film can exothermically decompose, eventually leading to thermal runaway and even fire.

To date, the research on battery short circuits mainly includes safety experiments and/or simulations of the electrochemical and thermal behaviors of Li-ion batteries during short circuits [28-34]. It was found that among various abuses such as crushing, external short circuit, internal short circuit (nail penetration), exposure to heat, etc., the nail penetration is one of the most dangerous scenarios for Li-ion batteries due to the concentrated heat generation at the short circuit location, which could initiate the exothermic reactions of active materials and electrolyte, and eventually lead to thermal runaway [5]. In general, experiments can be used to validate the simulation results and are useful for revealing the causes of defects, but they are dangerous to perform and money consuming, and the results vary with types of Li-ion batteries used. Consequently, reliable numerical models can be used as a tool to provide detailed analyses of Li-ion batteries in abnormal discharges. To date, many numerical simulations have been carried out to study the behavior of Li-ion batteries in abusive conditions [35-39], a part of which are focused on Li-ion battery nail penetration [40-43]. An electrochemical-thermal coupling model [44] is generally employed to simulate the penetration process, which is helpful in interpreting the physics of Li-ion batteries by giving a detailed interrelation of the electrochemical

processes and thermal responses. For example, the thermal behaviors of a 5.25 Ah Li-ion battery using a 3 mm steel nail penetration were simulated with the coupling model [42], in which a positive electrode boundary condition was manually set to produce the localized heat at the nailed region. Although the model provided accurate temperature profiles of the penetrated battery, it is unable to capture short circuit scenarios of Li-ion batteries of different capacities. Furthermore, to our knowledge, current research that can provide solutions to suppress thermal runaway and/or prevent thermal runaway propagation in battery packs during nail penetrations is scarce. Efforts are needed to be put into comprehending the causes of thermal runaway and developing advanced techniques to make Li-ion battery safer.

1.2 Objectives

In the previous section, overheating issues of Li-ion battery in normal and abnormal discharges, as well as current research works and their limitations were briefly discussed. To tackle the related issues, in this thesis, two advanced BTM systems and a comprehensive model are developed to improve the thermal performance and safety of Li-ion batteries during normal and abnormal operations, respectively. The specific strategies are summarized as follows:

- 1) To develop a practical BTM system for cylindrical Li-ion batteries. Due to their high energy density, cylindrical Li-ion batteries are more commonly used in pure EVs, in which the batteries are discharged at relatively low rates. The emphasis is placed on simplifying the cooling process and reducing the weight and cost of a phase change material (PCM)-based passive BTM system.
- 2) To develop a robust BTM system for prismatic Li-ion batteries. Hybrid electric vehicles and electric racing vehicles are mainly equipped with prismatic Li-ion batteries due to their high power density. The batteries are more frequently charged and discharged at high rates. Thus, a heat pipe-based active BTM system is developed to handle the heat generation.

3) To develop an electrochemical-thermal coupling model for simulating short circuits of Li-ion batteries. Possible strategies that can prevent thermal runaway of Li-ion batteries are also investigated based on the coupling model.

1.3 Thesis Outline and Contributions

A version of Chapter 2 has been published in *Journal of Power Sources* [Zhao R, Zhang S, Liu J, Gu J. A review of thermal performance improving methods of lithium ion battery: Electrode modification and thermal management system. *Journal of Power Sources* 2015; 299: 557-577.], which provided a brief introduction of Li-ion battery technology, as well as a state of the art review of Li-ion battery modeling, thermal management, and short circuit research.

A version of Chapter 3 has been published in *International Journal of Energy Research* [Zhao R, Gu J, Liu J. Performance assessment of a passive core cooling design for cylindrical lithium-ion batteries. *International Journal of Energy Research* 2018; 42: 2728-2740.], which elaborated the design of a novel PCM-based internal BTM system for cylindrical batteries. In particular, a thermal test cell was first fabricated in the paper, and it was used to verify the cooling effectiveness of the proposed design and to validate a thermal model. Simulations were then conducted based on the validated model to study the cooling effects of the proposed BTM system on authentic batteries. Compared to the conventional PCM-based external BTM system, the proposed system is simple in design, and it uses less PCM and achieves a better cooling effect for cylindrical Li-ion batteries.

A version of Chapter 4 has been published in *Energy* [Zhao R, Gu J, Liu J. Optimization of a phase change material based internal cooling system for cylindrical Li-ion battery pack and a hybrid cooling design. *Energy* 2017; 135: 811-822.], which optimized the PCM-based internal BTM system proposed in Chapter 3. Specifically, a 40-cell battery pack was optimized in both passive and active cooling modes. A uniform temperature distribution can be obtained in the battery pack when relatively thicker PCM cores are embedded in the interior batteries. In addition, without changing the battery appearance, the PCM-embedded batteries can be assembled in battery packs with cooling channels between battery rows to enjoy both the PCM cooling and air cooling.

A version of Chapter 5 has been published in *Journal of Power Sources* [Zhao R, Gu J, Liu J. An experimental study of heat pipe thermal management system with wet cooling method for lithium ion batteries. *Journal of Power Sources* 2015; 273: 1089-1097.]. In this Chapter, ultrathin flat heat pipes were used to sandwich prismatic batteries to manage their heat generation. A heat pipe-wet cooling combined active BTM design was proposed, which was found to be effective in maintaining the battery temperature at a low level even during high-rate discharges.

A version of Chapter 6 has been published in *Applied Energy* [Zhao R, Liu J, Gu J. Simulation and experimental study on lithium ion battery short circuit. *Applied Energy* 2016; 173: 29-39.], in which an electrochemical-thermal coupling model was developed to simulate Li-ion battery external and internal short circuits. The coupling model can simulate the temperature changes of non-thermal runaway batteries, and it can provide good predictions of the likelihood of thermal runaway and its occurrence time of unsafe batteries.

A version of Chapter 7 has been published in *Energy* [Zhao R, Liu J, Gu J. A comprehensive study on Li-ion battery nail penetrations and the possible solutions. *Energy* 2017; 123: 392-401], which gave a comprehensive study on battery nail penetration due to its dangerous character. The effects of several parameters, such as battery resistance, size, and capacity, as well as nail size, on the thermal behaviors of internally shorted batteries were obtained, and the possible solutions in suppressing the thermal runaway and preventing thermal runaway propagation were achieved.

Finally, the concluding remarks and some future research works are summarized in Chapter 8.

Chapter 2. Background and Literature Review

2.1 Introduction to lithium-ion (Li-ion) Battery

Batteries are often classified as primary (non-rechargeable) or secondary (rechargeable) depending on their capability of being electrically recharged, and this is determined mainly by the reversibility of the anodic and cathodic electrode reactions. In 1991, while solving various problems and improving the performance of Li-ion battery, Sony first commercialized the Li-ion battery. Nowadays, Li-ion batteries have emerged as the most promising energy storage technology in recent years due to their higher energy density, lighter weight, no memory effect, and lower self-discharge rate, when compared to other rechargeable battery technologies, such as nickel-cadmium and nickel-metal hydride batteries [1].

To have a better understanding of the working mechanism and to simulate the charging and discharging processes of a Li-ion battery, the internal structure and each component inside the Li-ion battery should be well understood. Fig. 2.1 shows the internal structure of disassembled prismatic and cylindrical Li-ion batteries, in which the white plastics are the separators, and the black ones are either current collectors with positive electrodes (cathode) or negative electrodes (anode). It is seen that a Li-ion battery is composed of many layers of electrochemical cells. In Fig. 2.2, the schematic illustration of an electrochemical reaction cell inside Li-ion battery is drawn. The reaction cell consists of layers of copper current collector, negative electrode, separator, positive electrode and aluminum current collector from left to right, and the electrolyte permeates the positive and negative electrodes and the separator and acts as a medium to transfer the ions during electrochemical reactions. During discharges, equal numbers of lithium ions and electrons are generated at the interface of the anode and electrolyte. The lithium ions transfer through the electrolyte solution and separator to react with the electrons that flow through the electrodes, conductive additives, current collectors, and the external circuit. As an example, the reaction of a $\text{Li}_x\text{Mn}_2\text{O}_4$ battery during the discharge process is given:



Overall reaction: $\text{Li}_{x-y}\text{Mn}_2\text{O}_4 + \text{Li}_y\text{C}_6 = \text{Li}_x\text{Mn}_2\text{O}_4 + \text{C}_6$

With the electrochemical reaction cells stacked or coiled, prismatic (Fig. 2.2b) or cylindrical (Fig. 2.2c) Li-ion batteries can be manufactured, respectively.

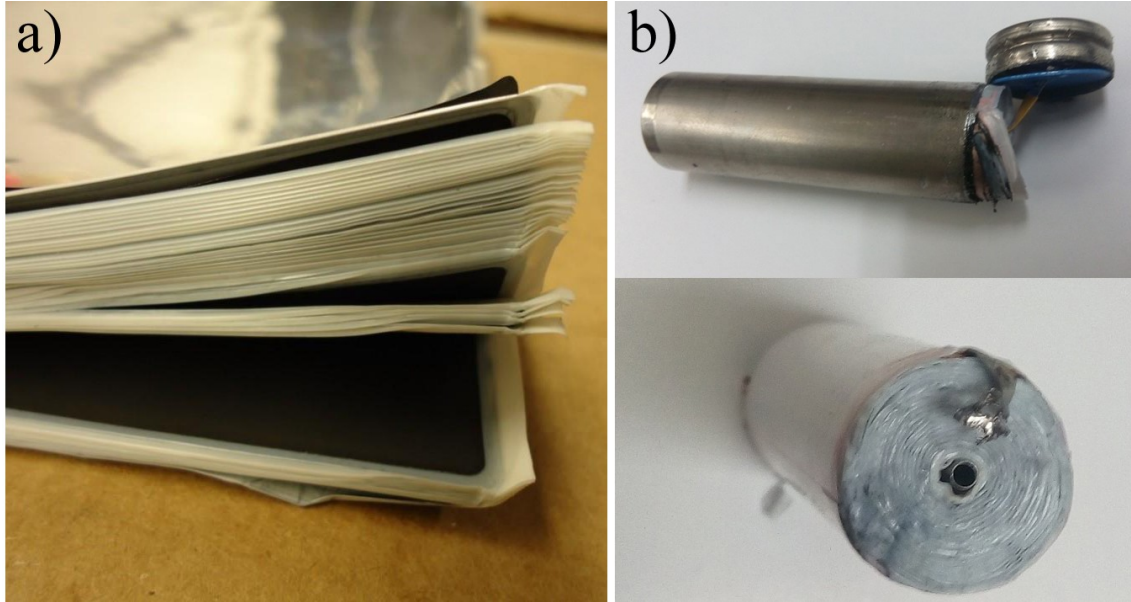


Figure 2.1. Internal structures of a) a prismatic battery and b) a cylindrical battery.

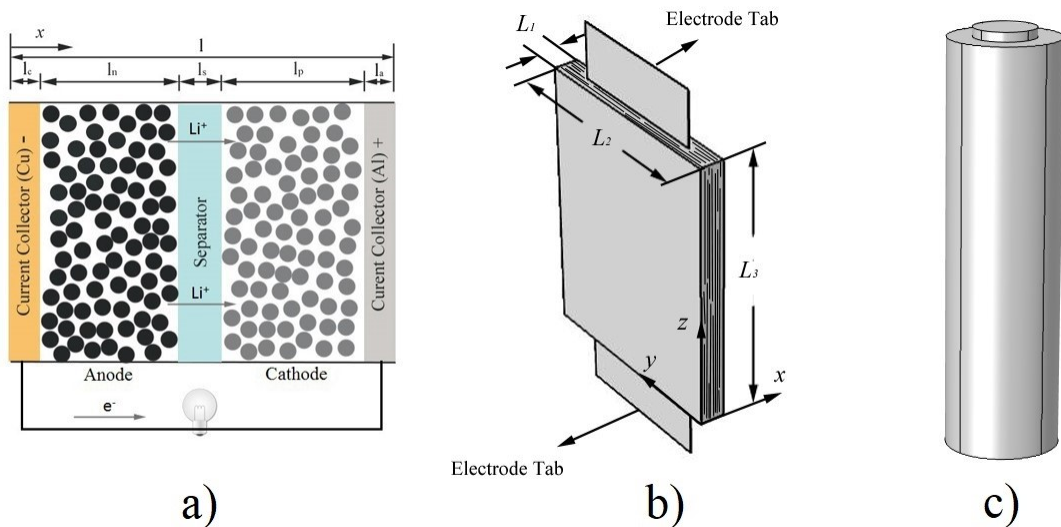


Figure 2.2. Schematic illustrations of a) an electrochemical reaction cell, b) a prismatic battery, and c) a cylindrical battery.

2.2 Energy Balance in Li-ion Battery

The energy balance equation, which guides the determination of temperature change in a Li-ion battery, has a general form of [21]:

$$\rho c_p \frac{dT}{dt} = \nabla \cdot (k \nabla T) + q \quad (2.1)$$

where ρ , c_p , T , t , k , and q indicate battery density, specific heat, temperature, time, thermal conductivity, and battery volumetric heat generation, respectively. The term on the left-hand side represents the heat stored inside the battery. The first term on the right-hand side is the three-dimensional heat conduction term, and it can be represented in a 2D in Cartesian or cylindrical coordinate if the temperature gradient in one direction is ignored [45, 46].

2.2.1 Heat Dissipation

When the Li-ion battery is cooled by air, the boundary condition correlated to the heat conduction term in the x-direction can be written as (similar for the other directions if the same boundary condition is applied):

$$-k \frac{\partial T}{\partial x} = h(T - T_{\text{amb}}) + \varepsilon \sigma (T^4 - T_{\text{amb}}^4) \quad (2.2)$$

where the first term on the right-hand side represents the convective heat transfer, followed by the radiation heat transfer term, which is sometimes omitted for simulation at low temperature. The terms h , ε , σ , and T_{amb} are the convective heat transfer coefficient, emissivity, Boltzmann Constant, and ambient temperature, respectively.

When the battery is directly contacted by coolant (liquid or solid) without phase change, the heat flux across the boundary of the battery and coolant will be same, which gives:

$$k \frac{\partial T}{\partial x} = k_c \frac{\partial T_c}{\partial x} \quad (2.3)$$

and the energy conservation equation in the coolant is:

$$\rho_c c_{p_c} \frac{\partial T_c}{\partial t} = \nabla \cdot (k_c \nabla T_c) \quad (2.4)$$

where the subscript c indicates the properties of the coolant. At the exterior surfaces of the coolant, the convective and radiative cooling boundary conditions are the same as (2.2).

If the coolant experiences phase change during the heat absorption, the apparent heat capacity method can be used to calculate the temperature variation [47]:

$$\rho c_{p,PCM} \frac{\partial T}{\partial t} = \nabla \cdot (k \nabla T) \quad (2.5)$$

where

$$c_{p,PCM} = \left\{ \begin{array}{ll} c_{p,s} & T < T_s \text{ Solid phase} \\ (1 - \gamma)c_{p,s} + \gamma c_{p,l} + \frac{h_f}{T_1 - T_s} & T_s < T < T_1 \text{ Solid/liquid phase} \\ c_{p,l} & T > T_1 \text{ Liquid phase} \end{array} \right\} \quad (2.6)$$

wherein, h_f is the latent heat of solid-liquid phase change, $c_{p,s}$ and $c_{p,l}$ indicate the specific heats of solid and liquid PCM, respectively. γ is the liquid fraction of the PCM, which is given by:

$$\gamma = \frac{T - T_s}{T_1 - T_s}, \quad T_s < T < T_1 \quad (2.7)$$

where T_s and T_1 are the lower and upper bounds of the PCM melting range.

2.2.2 Heat Generation

Different forms of the heat generation term q have been examined by Bandhauer *et al.* for Li-ion battery discharged under normal conditions [48]. In this section, two most frequently used expressions that are obtained from the thermodynamic energy balance and the electrochemical model are introduced as follows.

The most prevalent heat generation form is estimated by Bernardi *et al.* [49] and its simple form yields [50]:

$$q = I(U - V) - I \left(T \frac{\partial U}{\partial T} \right) \quad (2.8)$$

The first term on the right-hand side is the overall contribution of the ohmic loss inside battery cell, the charge transfer overpotential at the interface, and the mass transfer limitations, where U and V are the open circuit potential and cell operating potential, respectively. The second term is the entropy heat generation term or reversible heat term, which is occasionally neglected in high rate discharges. The significance of entropy heat in total heat generation has been explored in Refs. [51, 52].

Another widely used set of heat generation formulas are functions of parameters obtained from an electrochemical-thermal coupling model. From an electrochemistry perspective, by coupling a thermal model, more details about localized reactions and thermal behaviors can be clearly acquired since many electrochemical parameters vary with location and temperature. Compared to (2.8), the computational cost using the coupling model is significantly higher, but such expense is necessary when the heat distribution on an electrochemical cell is of interest, such as during the design of electrodes.

The heat generation calculated from the coupling model has three sources, which are reaction heat, entropy heat, and ohmic heat (or Joule heat) [53]:

$$q_r = \frac{\int_0^{l_n+l_s+l_p} j^{Li} (\Phi_s - \Phi_e - U) dx}{l} \quad (2.9)$$

$$q_e = \frac{\int_0^{l_n+l_s+l_p} j^{Li} T \frac{\partial U}{\partial T} dx}{l} \quad (2.10)$$

$$q_j = \frac{\int_0^{l_n+l_s+l_p} \left[\sigma^{\text{eff}} \left(\frac{\partial \Phi_s}{\partial x} \right)^2 + k^{\text{eff}} \left(\frac{\partial \Phi_e}{\partial x} \right)^2 + k_D^{\text{eff}} \frac{\partial(\ln c_e)}{\partial x} \frac{\partial \Phi_e}{\partial x} \right] dx}{l} \quad (2.11)$$

In the electrochemical cell, since only the electrodes and separator (negative electrode, l_n ; separator, l_s ; positive electrode, l_p , as shown in Fig. 2.2a) are the heat generation components, the volumetric heat generation rate of the entire cell is averaged over the entire thickness (l) of the electrochemical cell. In (2.9), j^{Li} denotes the reaction current density in the electrochemical model; Φ_s , Φ_e , and U are the electrical potentials of solid active material, electrolyte, and a reference potential, respectively. For the joule heating (2.11), the first term of the integrand refers to the ohmic heat generated in the solid electrode, and

the last two terms describe the heat from charge transfer in the liquid electrolyte. The terms σ^{eff} , k^{eff} , k_D^{eff} , c_e are conductivities of electrode and electrolyte, electrolyte diffusional conductivity, and electrolyte concentration, respectively.

With substituting the heat dissipation term and heat generation term into the energy balance equation, the temperature data of the Li-ion battery can be calculated in finite element solvers.

During abnormal discharges, Li-ion batteries may also have the localized heat generation in addition to the discharge heat generation. In [42], a localized short circuit heat generation rate per unit area was proposed:

$$S_{\text{sc}}^{\text{surf}} = \frac{1}{2} r_{\text{nail}} S_{\text{sc}} \quad (2.12)$$

where $S_{\text{sc}}^{\text{surf}}$ is the localized heat generation per unit area at the short circuit region, r_{nail} is the radius of the nail, and S_{sc} is the battery heat generation rate calculated from (2.8) with setting a cathode boundary condition of:

$$\Phi_{s,p} = 0.5 \exp(-0.07t) \quad (2.13)$$

where $\Phi_{s,p}$ is the potential of the positive electrode and t is the time after short circuits.

2.3 Thermal Management of Normally Discharged Batteries

2.3.1 Overheating Issues of Normally Discharged Batteries

A high operating temperature can result in several side effects on Li-ion batteries, such as short lifespan, reduced capacity and power with cycling, and even thermal runaway in some extreme conditions. The capacity fading and power loss of Li-ion battery have been reviewed by Vetter *et al.* [54]. Solid electrolyte interface (SEI) is a passivation layer formed on electrode active materials during the cycling of Li-ions, which will consume active Li-ions and electrolyte. They summarized that the development of solid electrolyte interface (SEI) and SEI dissolution on the carbonaceous anode, the crystal structure instability, active material dissolution, and SEI formation on the cathode [55-58] are all factors that give rise to the depletion of running Li ions and active materials and the

increase of internal resistance, which finally induce capacity fading and power reduction of Li-ion batteries. At high temperatures, these processes can be accelerated and cause severe loss of available energy [59, 60].

Provided that available lithium ion loss and active material decline are the two origins of capacity fading [61], Santhanagopalan *et al.* [62] tested LiCoO₂/C battery at 5 different initial temperatures: 5°C, 15°C, 25°C, 35°C, 45°C and compared the changes of the two factors from the calculated active material weight and non-dimensional lithium concentration inside the electrodes. It was found that at low temperature (5°C), the active material loss only accounted for 1% of the total capacity loss. Conversely this was the predominate factor as the temperature exceeded 35°C. Some other research related to the fading mechanisms of LiMn₂O₄ and LiFePO₄ batteries are also available in Refs. [60, 63]. Although several experiments have shown that the high-temperature performance of Li-ion batteries could be improved by coating or doping cathode materials [64-66], higher capacity fading rates were still observed as the operating temperature increased.

2.3.2 Battery Thermal Management Systems

To ensure long lifespans and smooth operations of Li-ion batteries, battery thermal management (BTM) systems that can create suitable temperature ranges for batteries to charge and discharge are indispensable components. Generally, the BTM system consists of either air cooling, liquid cooling, heat pipe cooling, or PCM cooling. Different BTM systems have both their advantages and disadvantages, and a BTM system should be properly selected for batteries used in different applications. These four categories of BTM systems will be introduced in the following sections:

2.3.2.1 Air Cooling

Air cooling can be classified into two categories, natural convection and forced convection, depending on whether a cooling fan assists with the cooling process. Forced convection attracts more research interest due to its high convective heat transfer coefficient and satisfying effectiveness in cooling.

Because of the advantages such as direct access, low viscosity, and light weight of air, and the simple configuration, low cost, and easy maintenance of the cooling system, air cooling is one of the most commonly adopted cooling strategies in our daily life, widely used in electronics and vehicles [6-10]. Since the specific heat capacity of air is much lower than many other cooling mediums, this method is normally applied to batteries with low to moderate heat generation rates. The development of the air-based BTM system is mainly focused on the optimization of the 1) air flow rate, 2) battery layout, and 3) flow path [67-74].

1) In Ref. [68], the cooling performance of different air cooling designs for cylindrical cell battery pack are investigated through both numerical and analytical analyses. Different inlet Reynolds (Re) numbers were employed and compared, and it was found that a higher Re number could lead to a lower maximum temperature but a relatively uneven temperature distribution. The ratio between the cooling channel size and the battery pack size was also characterized as an important factor that could affect the average temperature of the battery pack.

2) Research on advancing the cell layout aims at designing battery pack with an optimal cell arrangement and spacing to achieve a better cooling effect and a lower energy consumption. In Ref. [67], the temperature distributions in an 8-cell prismatic battery pack with different cell spacings and air flow rates were simulated. It was found that the peak temperature increases but the temperature uniformity improves as the cell gap widened at a constant flow rate, and an unequal spacing is favorable because it offers a relatively unblocked cooling environment for the center cells. The arrangement of cylindrical Li-ion batteries has also been explored [8, 9]. Yang *et al.* [8] studied the thermal behaviors of aligned and staggered 6×10 battery packs during discharges with air cooling and claimed that the aligned battery pack with specific longitudinal and transverse intervals excelled over the staggered layout.

3) In applications that require a fixed battery layout, the cooling performance can be improved by changing the flow paths or the structures of the inlet and outlet [69-72]. Noting that the continuous cooling in one direction can lead to a higher temperature at the outlet, the non-uniformity can be resolved by switching the air flow direction after a certain time

interval. For example, a reciprocating air cooling design attains a 72% drop in temperature difference with a switching time interval of 120 s [69]. In Ref. [71], battery packs with different flow channel configurations were simulated. It was found that the use of a Z-type channel and tapered cooling ducts lowered the maximum temperature and temperature gradient inside the battery pack, and the assembly of orifices at the closed end of the lower duct further promoted the cooling effect by lessening the pressure.

2.3.2.2 Liquid Cooling

When a compact battery pack discharges at a high-rate, both natural and forced air convection will be unable to manage the battery temperature within an allowable range. Having a much higher convective heat transfer coefficient, liquid-based BTM systems could achieve a better performance than air cooling [75], but it generally requires more complicated configurations to achieve.

The liquid cooling can also be categorized into active [76-82] and passive [13-15, 83-84] modes depending on whether the liquid is compelled to circulate during the cooling process. The active liquid cooling method is more efficient than the passive one in controlling the temperature of batteries thanks to the continuous cooling of the coolant in the condenser, but this type of system is more complex and has a higher technical requirement on the overall circulatory system. In comparison, the passive mode cools down the battery by using the energy storage ability of liquids, and the corresponding BTM systems are relatively easy to construct, operate, and oversee throughout operations. The following text presents a brief review of the progress in both active and passive liquid-based BTM systems.

Active liquid-based BTM systems have been investigated in many studies with various focuses. For example, Karimi and Dehghan [85] compared the performance of two mediums, silicon oil and air, in the flow network cooling circulations for Li-ion battery packs. Recently, the cold plate has emerged as a popular tool to achieve the active liquid cooling due to its compactness [77-80]. The cold plate cooling method relies on the circulation of liquid inside the mini-channels that are closely arranged in the plate. When the fluid cools down in the condenser, the cold plate can continuously offer excellent

performance in dissipating the heat [77]. A three-dimensional thermal model was developed in Ref. [11] to examine the performance of the cold plate with water as the medium. By adjusting the number of channels, the flow rate, and the flow directions inside the channels, the optimal parameters were obtained. The effect of the channel geometry was also test in another study by looking at the temperature uniformity, mean temperature, and pressure drop in different serpentine-channel designs [79].

Attempts have also been made to advance passive liquid-based BTM systems. Boiling liquid cooling is one of passive liquid cooling methods that take advantage of the evaporation of the low boiling point liquids to absorb heat. For example, hydrofluoroether liquid (NovecTM 7000) is an environmentally friendly inflammable liquid with a high electric resistance, and it has a boiling temperature of 34°C. In Ref. [83], Hirano *et al.* experimentally tested the performance of NovecTM 7000 as the medium in a battery pack. It was found that the maximum temperature of the battery pack (ten 1Ah battery cells in series) was able to be kept at around 35°C even at a high discharge rate of 20 C (20 C means the battery is fully discharged in 1/20 hours).

2.3.2.3 Heat Pipe Cooling

A typical heat pipe is composed of a sealed pipe and its compatible working fluid that is kept at the saturation pressure of the fluid at the corresponding fluid temperature. During heat transfer, the fluid boils at the hot surface and condenses at the cold surface. The movement of the fluid can quickly transfer the thermal energy between the evaporator and condenser of the heat pipe. Owing to high thermal conductivity, heat pipes have been widely used in electrical devices, e.g., laptops, to transfer heat from the heat source to the condenser side for dissipation. For usage on Li-ion batteries, the capillary-based heat pipes patented by General Motors [86] are commonly used because of their compactness and flexibility, which can accommodate different battery geometries. The latest research on heat pipe-based BTM systems is summarized in Table 2.1.

Table 2.1. Summary of the innovative heat pipe-based BTM system for Li-ion batteries.

Heat pipe type	Method	Heat Source	Cooling source	Battery pack	Variables	Authors
Ultra-thin flat heat pipe	Experiment	Battery pack	Natural convection Forced convection Water bath Wet cooling	4S1P 3Ah 4S1P 8Ah Pouch batteries	Angle of heat pipe Cooling source Spray frequency	Zhao <i>et al.</i> [87]
Flat heat pipe	Experiment	Electric heater	Natural convection Forced convection	-	Wind speed Heat sink vs. heat pipe + heat sink	Tran <i>et al.</i> [22]
-	Experiment Simulation	One cell	Natural convection Forced convection	12 Ah cylindrical battery	Natural convection vs. heat pipe	Wu <i>et al.</i> [21]
Tube heat pipe with flat condenser	Experiment	Electric heater	Thermostat bath	-	Heating power Angle of heat pipe	Rao <i>et al.</i> [23]
Oscillating heat pipe	Experiment	Electric heater	Thermostat bath	-	Heating power Angle of heat pipe	Rao <i>et al.</i> [88]
Tube heat pipe	Experiment	Electric heater	Adiabatic Forced convection	-	Fan inlet area Air flow direction Angle of heat pipe Heating power	Tran <i>et al.</i> [89]
Tube heat pipe with flat condenser	Experiment	Simulated battery container	Liquid box	-	Heating power Heat pipe cold exposure temperature	Wang <i>et al.</i> [90]
Pulsating heat pipe	Experiment	Heating cartridges	Forced convection	-	Heating power Working fluid Air velocity and temperature Angle of heat pipe	Burban <i>et al.</i> [91]
Tube heat pipe	Analytical and numerical simulation	Constant heat source, $q = 240 \text{ kW m}^{-3}$	Constant T Forced convection	Equivalent 20 Ah battery at 100 A discharge rate	Simulation model Cooling solution	Greco <i>et al.</i> [92]

For heat pipe-based BTM systems, optimization of the contact between pipe and heat sources, as well as the improvement of cooling at the condenser side are the two main approaches to enhance the cooling performance. Tran *et al.* [22] investigated the flat heat pipe-based BTM system by applying constant heat fluxes to the evaporation side of heat pipes instead of using real battery packs. In the experimental tests, a heat pipes-heat sinks combined system was shown to be more effective in controlling the temperature than the system using heat pipes alone.

Tube heat pipes are also of great interest to researchers [88-92]. However, because the geometry of tube pipes limits their contact with batteries, tube heat pipes are usually welded or attached to a copper/aluminum plate, or pre-manufactured with a flattened evaporation section, so as to enlarge the contact area with the batteries [90]. Four working fluids: water, acetone, methanol, and n-pentane, were investigated with different heating powers and inclination angles, and it was demonstrated that acetone and n-pentane were suitable for low powers and low air temperatures (e.g., below 100 W and 30°C, respectively) while the other two fluids were good for relatively higher heating powers and air temperatures [91]. A theoretical and computational study was also conducted on the heat pipe-based BTM system in Ref. [92], wherein a one-dimensional battery model was built and connected with a thermal circuit network of heat pipes. It was found that the results from the one-dimensional model showed good consistency with that of the analytical model and the three-dimensional model [92].

2.3.2.4 Phase Change Material (PCM) Cooling

PCM was initially exploited to store thermal energy for buildings, where plenty of research has been conducted [93-97]. PCM-based BTM systems were firstly introduced by Al-Hallaj and Selman for a 18650 Li-ion battery pack, and the paraffin mixture of pentacosane and hexacosane was used as the PCM [16]. As a branch of the passive BTM system, the PCM-based system has many advantages, such as being compact, low cost, and no need of a circulatory network, which has made PCM-based BTM systems of particular research interest over the past few years. Nevertheless, there are several drawbacks with

this BTM system, which are summarized in Fig. 2.3 together with potential solving strategies.

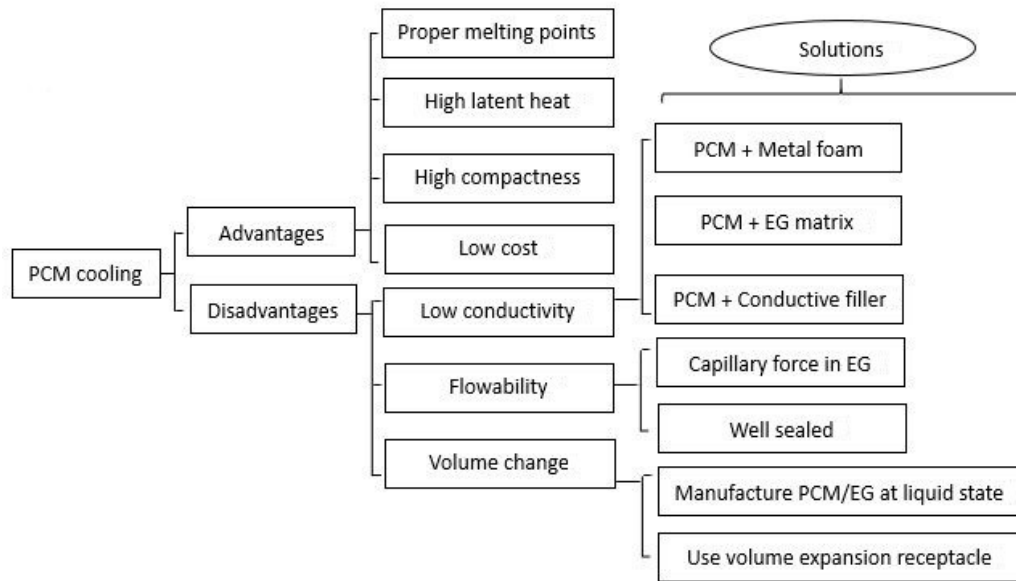


Figure 2.3. Selected characteristics and recent research interests in PCM-based BTM system for Li-ion battery.

All the works reviewed in this section on PCM-based BTM systems only include the materials that experience solid-liquid phase change. The most widely researched PCM for Li-ion battery thermal management is paraffin wax, which is the mixture of various hydrocarbon groups and exhibits the following superiorities: a hard-to-decompose character, a widely acceptable unit price, and a broad range of phase change temperatures varying with the number of main chain carbon atoms. In Table 2.2, the paraffin with suitable phase change temperatures for Li-ion battery thermal management is listed. Different PCMs can be chosen from the list for Li-ion batteries used for different tasks. The PCM-based BTM system can be classified into systems that use 1) PCM only, 2) PCM with metal foam or expanded graphite (EG), 3) PCM with conductive fillers, and 4) hybrid cooling.

Table 2.2. Paraffin with suitable melting temperatures for Li-ion battery thermal management.

Name of straight chains	No. of carbon atoms	Melting point (°C)	Latent heat of fusion (kJ kg ⁻¹)	Density (kg m ⁻³)
Octadecane	18	28.0 – 30.0	244	777
Nonadecane	19	32.0 – 34.0	222	786
Eicosane	20	36.7	246	789
Heneicosane	21	40.5	200	792
Docosane	22	42.0	249	778
Tricosane	23	48.0 – 50.0	232	797
Tetracosane	24	52.0	255	797
Pentacosane	25	54.0	238	801

1) PCM only

Since its first use in Li-ion batteries, PCM-based BTM systems have gained widespread attention. In 2002, Al-Hallaj and Selman discussed the advantages of PCM-based BTM systems over an active BTM system for Li-ion battery cooling [98]. The work in Ref. [99] incorporates mixtures of PCMs into a BTM system. Four kinds of phase change substances were employed in simulations: capric acid, eicosane, Na₂(SO₄)·10H₂O, and Zn(NO₃)₂·6H₂O. In the conditions of combining capric acid with either one of the other three materials, the capacities of the double-shell PCM cooling system were compared with the single shell one. The results indicated that the double-shell design had higher exergy efficiency than the single-shell system in most cases.

2) PCM with metal foams/EG

The main disadvantage of PCMs is their low thermal conductivity (below 0.5 W m⁻¹ K⁻¹), which makes their response tard to the heat surge of a discharged battery pack, especially when a thick layer of PCM is used. Therefore, composite matrices were introduced and studied to increase the overall thermal conductivity of BTM systems.

The PCM/metal foam matrix can raise the thermal conductivity by one order ($\sim 3\text{--}10 \text{ W m}^{-1} \text{ K}^{-1}$). Khateeb et al. [100] proposed a PCM/Al foam matrix for cooling a battery pack in scooters, in which the foam used was the Duocel aluminum foam with a porosity of 90–92% and had 40 pores per inch. The testing results showed that the use of the Al foam can decrease the temperature rise and flatten the temperature distribution. The PCM/copper foam cooling matrix has also been studied [101], and a low porosity was recommended due to the preferable heat conduction. Both the PCM/Al and PCM/copper matrices have also been numerically studied [102, 103].

Although metal foams can improve the heat transfer of PCM-based BTM systems, proper sealing strategies need to be carried out to handle leakage of melted PCM. Mills *et al.* first proposed an expanded graphite (EG) matrix to address this issue, and the production method of EG was elaborated in Ref. [18]. Their findings showed that the average thermal conductivity of the PCM composite could be increased to $16.6 \text{ W m}^{-1} \text{ K}^{-1}$ after integrating the EG matrix, which is almost 2 orders greater than that of the pure PCM used (RT 42 paraffin with a thermal conductivity of $0.2 \text{ W m}^{-1} \text{ K}^{-1}$). A merit of this PCM/EG composite was that the liquid state PCM could be immobilized inside the matrix with capillary force, thus avoiding leakage. In practices, this strategy has several limitations. For examples, it was found that at least 30 wt.% EG is required to maintain leakage at a low level, which substantially lowers the latent heat of the PCM-based BTM system [26, 27]. Also, the manufacture and potential fracture of the PCM composite could increase the initial and maintenance costs on the BTM system.

3) PCM with conductive fillers

Conductive fillers, such as graphene, carbon fiber, and carbon nanotube, have also been utilized to enhance the thermal conductivity of PCMs in previous research [104, 105]. For instance, Goli et al. [104] found that the thermal conductivity of the PCM could reach above $10 \text{ W m}^{-1} \text{ K}^{-1}$ with 1 wt.% graphene added. In Ref. [105], four types of carbon fibers were prepared with the average lengths of 2, 3, 5, and 8 mm and were composited with the PCM for testing. It was observed that the PCM with 2 mm long carbon fibers at a mass fraction of 0.46 % could achieve the smallest temperature gradient in the battery pack.

4) PCM integrated hybrid cooling

Since PCM-based BTM systems manage battery temperature by relying on the high latent heat of PCM, the cooling effect of the BTM system degrades dramatically as all the PCM melts. Thus, for high-rate continuous cycle operations, an active cooling system could be integrated to ensure the enduring cooling effectiveness of the PCM-based BTM system [25, 106].

In Ref. [107], a battery pack equipped with PCM-based BTM system was tested in a wind tunnel. The results showed that a sole PCM matrix was unable to cool the battery pack during a high-current continuous charging and discharging test. When tested in the wind tunnel with an air flow velocity of 3 m s^{-1} , the maximum temperature of the battery pack decreased significantly, and the battery pack operated safely in the cycling test. A thermodynamic assessment of an active cooling/heating system using phase change slurry (PCS) was studied in Ref. [17]. The PCS was made up of encapsulated PCM (1–20 μm) and water or a water/glycol solution. Two PCMs, octadecane ($T_{\text{melting}} = 28^\circ\text{C}$) and pentadecane ($T_{\text{melting}} = 10^\circ\text{C}$), were employed as the cooling and heating mediums in the PCS, respectively, and the air in the vehicle cabin acted as the cooling/heating source. These designs are effective in managing battery temperature, but they require special structural designs and add complexity to the BTM system.

A summary of the state-of-the-art PCM-based BTM systems is provided in Table 2.3, which can be combined with Fig. 2.3 to give a whole picture of the research trends on the PCM-based BTM system.

Table 2.3. Summary of research on PCM-based BTM systems.

PCM cooling system	Research method	Phase change material	Thermal conductivity (W m ⁻¹ K ⁻¹)	Latent heat (kJ kg ⁻¹)	Melting point (°C)	Specific heat capacity (kJ kg ⁻¹ K ⁻¹)	Density (kg m ⁻³)	Authors
PCM	Simulation	Pentacosane & hexacosane	0.29 (solid) 0.21 (liquid)	195	56	1.77	910 (solid) 822 (liquid)	Al-Hallaj, Selman [16]
PCM	Experiment	Paraffin wax (RT28 HC)	-	245	28	-	-	Hemery <i>et al.</i> [108]
PCM	Simulation	n-octadecane	0.358 (solid) 0.152 (liquid)	225	28 – 30	2.15 (solid) 2.18 (liquid)	814 (solid) 724 (liquid)	Javani <i>et al.</i> [109]
PCM	Simulation	Caprid acid	2	153	31.4	2.09	884	Ramandi <i>et al.</i> [99]
		Eicosane	0.27	241	36.7	1.90	778	
		Na ₂ (SO ₄)·10H ₂ O	0.544	254	32.3	1.93	1485	
		Zn(NO ₃) ₂ ·6H ₂ O	0.31	147	36.3	1.34	2065	
PCM/Al foam	Experiment Simulation	Pentacosane & hexacosane	$k = k_{Al}\epsilon + k_{pcm}(1 - \epsilon)^*$	-	40 - 44	-	$\rho = \rho_{Al}\epsilon + \rho_{pcm}(1 - \epsilon)^*$	Khateeb <i>et al.</i> [100]
PCM/Copper foam	Experiment	Paraffin wax (RT44 HC)	0.8 – 11.33 (varying with porosity and pore density)	270.7 (PCM)	44	2.25 (PCM)	810 (PCM)	Li <i>et al.</i> [101]
PCM/EG	Experiment	Paraffin wax (RT42 HC)	16.6	185	42	1.98	789	Mills <i>et al.</i> [18]
PCM/EG	Simulation	Paraffin wax (RT42 HC)	16.6	127	42	1.98	789	Mills and Al-Hallaj [110]
PCM/EG	Simulation (thermal runaway)	Paraffin wax (RT42 HC)	16.6	185	42	1.98	789	Kizilel <i>et al.</i> [111]
PCM/EG + graphite sheet	Experiment	Paraffin	3.95	132.6	21.6 – 25.5	2.39	842	Lin <i>et al.</i> [112]
PCM/graphene	Experiment Simulation	Paraffin wax (IGI - 1260)	15 – 45 (varying with mass ratio of graphene)	-	70	2.5	900	Goli <i>et al.</i> [104]
PCM/carbon fiber	Experiment	Paraffin mixture	0.21 (PCM)	242	42 – 49	-	912	Babapoor <i>et al.</i> [105]
PCM/EG + Air cooling	Experiment Simulation	Paraffin wax (RT44 HC)	7.85	181	44	2.5	714	Ling <i>et al.</i> [107]

2.4 Research on Abnormally Discharged Batteries

2.4.1 Overheating Issues of Abnormally Discharged Batteries

Safety is the priority for all energy storage systems. In a Li-ion battery cell, oxidizer (cathode) and fuel (anode) are kept in a sealed container. In normal operating conditions, anodes and cathodes are unable to be electrically contacted, and the chemical energy can be smoothly transferred to electrical energy. However, as the temperature of the cell reaches the threshold of thermal runaway, typically between 130°C and 200°C [113], the cell may experience a series of exothermic chemical reactions and generate a great amount of heat and gas, which may further cause shrinkage of the separator and lead to more extensive heat release processes, with the maximum temperature soaring to as high as 500°C.

Routine use of Li-ion batteries usually cannot bring about thermal runaway, even at high rate discharge conditions. However, improper charge and discharge [114-116] and short circuit during operations [30, 117, 118] may give rise to this danger. A few notable Li-ion battery safety accidents in recent years are listed in Table 2.4.

Table 2.4. A few notable Li-ion battery induced accidents in recent years.

Date	Accident	Causes
May 2018	Tesla Model S caught fire	Vehicle hit a crash barrier
March 2018	Tesla Model S caught fire	Vehicle crashed with cars
March 2017	Tesla Model S caught fire	Charging
October 2013	Tesla Model S caught fire	Vehicle hit metal debris
January 2013	Boeing 787 emergency landing	Battery overcharge
May 2012	BYD e6 caught fire	Collision accident
June 2011	EV bus caught fire	Li-ion battery overheated
June 2011	Chevrolet Volt caught fire	Crash testing
September 2010	Boeing 747-400F cargo plane caught fire	Auto-ignition of cargo pallet with Li-ion batteries
April 2010	Acer recalled 2700 laptop batteries	Potential overheating and fire hazards

Despite the relatively low probability of thermal abuse, Li-ion battery systems should be well designed and be able to overcome the dramatic heat release in case it happens. In recent years, improved electrolytes [119-122], electrolyte additives [123-128], separators [129-132], as well as BTM systems [15, 111] have been continuously introduced and investigated to address this thermal issue of Li-ion batteries with the utilization of chemical (end reactions) and physical (fast absorption of heat) mechanisms.

2.4.2 Studies on Abnormally Discharged Batteries

Pretend that Li-ion batteries are equipped with suitable BTM systems during charges and discharges, short circuits will be the most likely causes of the Li-ion battery-related accidents. For example, during EV crashes, the batteries may be damaged and shorted. Significant amount of heat will be generated and generally cannot be controlled by the original BTM systems. Therefore, research needs to be done to better understand the short circuit behaviors of Li-ion batteries, which is imperative to the research on battery thermal runaway prediction and management. To date, much research has been done on Li-ion battery short circuits [113, 133, 134-137]. Three main categories, material analyses, battery tests, and numerical simulations, were mainly explored.

In terms of material analyses, accelerating rate calorimetry (ARC), differential scanning calorimetry (DSC), and heating reactor are generally used to test the exothermic behaviors of a whole battery or battery materials [31, 113, 133, 138]. For instance, Doughty and Roth published a general discussion on Li-ion battery safety [113], in which a summary of variables, such as cathode/anode materials, overcharge limit, and state of charge (SOC), on the battery safety performance was given based on ARC and DSC testing results. In Ref. [133], the onset, transition, and peak temperatures of three popular Li-ion batteries (LiNiMnCoO_2 , LiCoO_2 , and LiFePO_4) were recorded through heating Li-ion batteries in a reactor. The testing results are significantly valuable for research regarding battery modeling and safety.

Meanwhile, experiments such as the nail penetration test, pinch test, internal nail test, were performed on Li-ion batteries and packs [30, 31, 41, 117, 118] to simulate the damaged batteries in accidents. For example, Cai *et al.* did pinch tests on several Li-ion

batteries with different parameters, and it was found that the increase of battery voltage and capacity can dramatically stimulate the occurrence of thermal runaway [118]. Regarding safety tests on battery pack level, thermal runaway propagation is of particular interest, and relevant research has been conducted [30-32]. For instance, Lamb *et al.* at Sandia National Laboratories investigated the thermal runaway propagation in 18650-type and pouch-type battery packs with different electrical configurations [30]. It was found that the parallel configuration is more dangerous for Li-ion battery packs due to the continuous delivery of energy from the other batteries in the battery pack to the shorted battery.

Simulations also play an important role in battery short circuit research [35-42, 138]. Hatchard *et al.* first developed a 1D thermal model with a chemical heat generation component [35], and the model was proved accurate in simulating the temperature of a Li-ion battery in an oven test. The model was then reproduced and extended by Kim *et al.* [37] to a 3D model to consider the geometry features. Subsequently, several comprehensive models considering battery state, electrochemical reactions, and battery shape changes were developed to capture the battery statuses after short circuits. For example, in Ref. [42], nail penetration of a 5.25 Ah Li-ion battery was simulated by combining an electrochemical model with a reaction model. At the nail site, the localized heat source was created by setting a boundary condition for the positive electrode, and the heat generated by the battery bulk was calculated with the reaction functions based on Arrhenius-type equation sets. Zhang *et al.* developed a mechanical-electrical-thermal coupling model to predict a Li-ion battery under mechanical abuse [36]. The model is successful in predicting the onset of mechanical crush induced short circuits, and in giving the subsequent voltage and temperature evolutions.

Chapter 3. Development of a PCM-Based BTM System for Normally Discharged Cylindrical Li-ion Batteries

3.1 Overview

Battery thermal management (BTM) systems are an indispensable component for large-size lithium-ion battery packs used in aerospace and automotive applications. Besides providing a proper temperature range for batteries to operate, thus improving their efficiency, lifespan, and safety, BTM systems also need to be well designed while considering the cost, weight, and practicability. In this Chapter, a novel internal passive BTM system is proposed for cylindrical Li-ion batteries. The design embeds a phase change material (PCM) filled mandrel in the cylindrical Li-ion battery core to achieve the cooling effect. It is the first time that PCM is used internally as a cooling medium for cylindrical batteries. In this Chapter, a thermal test cell is first fabricated and tested in a wind tunnel, and is also used to validate a numerical thermal model. The PCM-based BTM system is further investigated through the model and found to be able to create a preferable environment for batteries to operate. Specifically, the internal BTM system consumes less PCM and achieves a lower temperature rise and a more uniform temperature distribution than an external BTM system. The proposed BTM system can also fully exert its latent heat to manage the heat generated from the battery without using a thermally conductive matrix, which is usually composited with PCM in external BTM systems.

3.2 Battery and Battery Pack Designs

Batteries in external PCM-based BTM systems are immersed in the PCM or PCM composite to achieve cooling effect, as shown in Fig. 3.1b, where the system should be well sealed or the PCM composite needs to be produced with exact sizes of holes to tightly embrace the batteries. Thermal management for cylindrical batteries can be attained with low complexity when assembling the sealed PCM-filled mandrels (PCM cores) during the battery manufacturing stage.

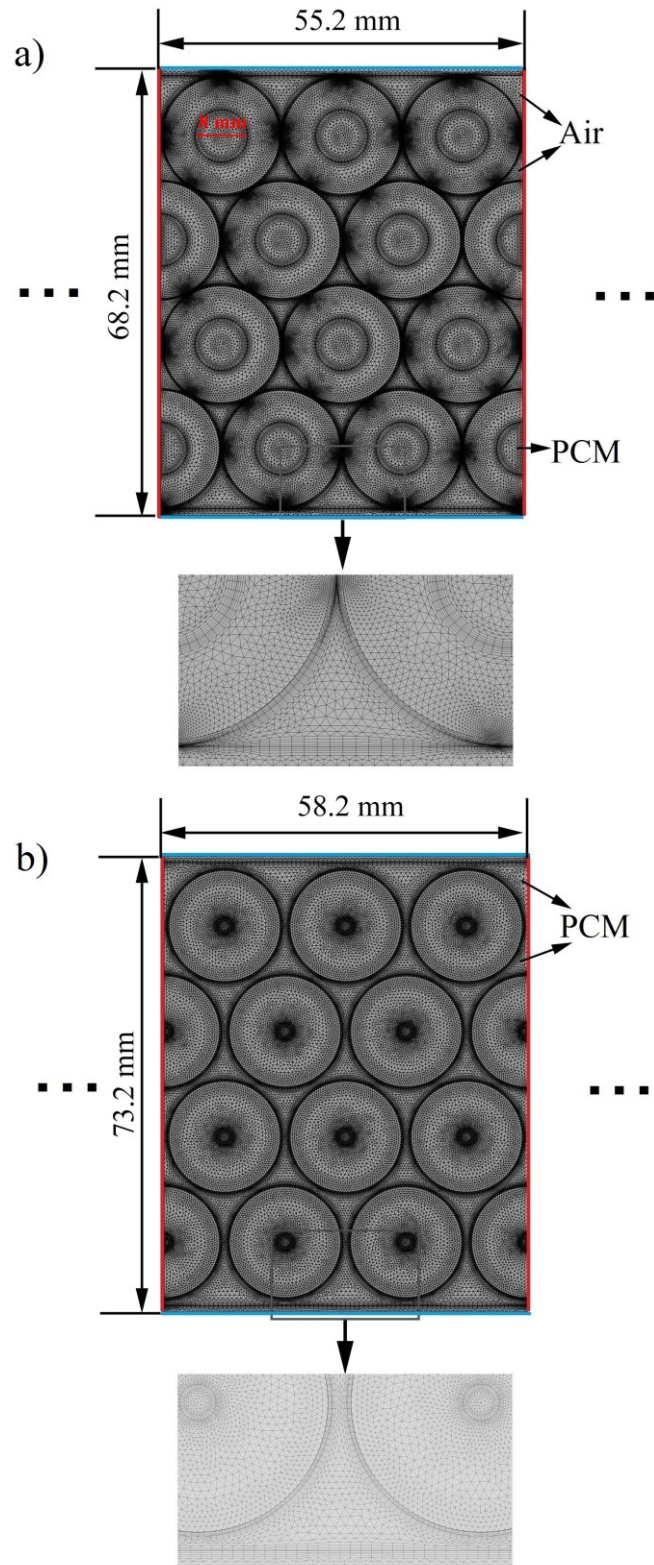


Figure 3.1. 4-layer battery packs equipped with a) the proposed internal PCM-based BTM system, and b) the conventional external PCM-based system.

Photos of a disassembled 18650 Li-ion battery are provided on the left plot of Fig. 3.2. It is seen that the Li-ion cell is wrapped on a hollow mandrel ($r_m = 1.25$ mm), which is designed for electrolyte injection and gas emission during thermal runaway. For the internal BTM system, the hollow mandrel is replaced by a PCM core, which acts as a heat sink to absorb the heat generated from the battery, as shown on the right plot of Fig. 3.2. At the manufacturing stage, the liquid PCM can be injected and sealed in a thin wall mandrel to avoid leaking issues, and a groove can be machined on the mandrel to ensure electrolyte injection and gas release.

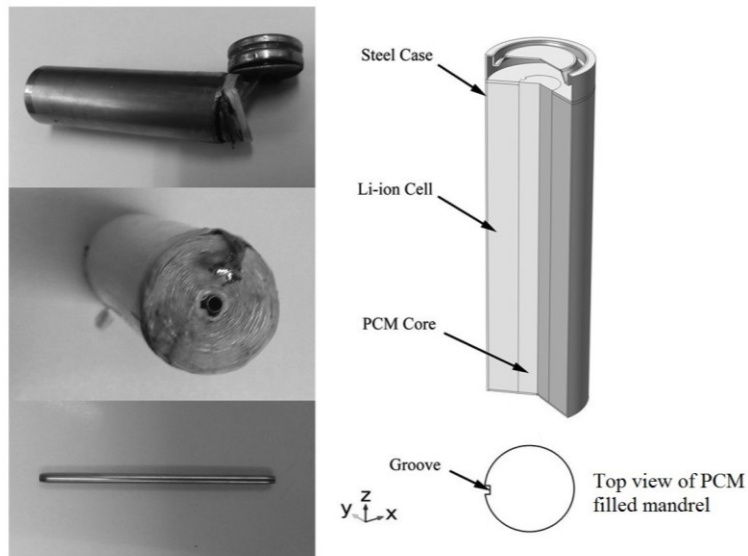


Figure 3.2. Pictures of a disassembled 18650 Li-ion battery and a schematic of the PCM core cooling design.

In Fig. 3.1a and b, schematics of 4-layer battery packs equipped with the internal and external BTM systems are given, respectively. The schematics are the meshed geometries of two BTM systems obtained in Comsol Multiphysics, which will be explained in Section 3.3.2. Since the battery pack can have a large dimension in the horizontal direction, repeating units with a 3-battery width are selected for this study to reduce the computational cost. Correspondingly, an adiabatic boundary condition is applied on the left and right sides of the packs, as indicated by the red lines in Fig. 3.1a and b, while on the top and bottom surfaces, indicated by the blue lines, a natural convection boundary condition is used. In the internal BTM design, PCM cores with 4 mm radius are embedded in the batteries, and all the batteries are closely packed. For the external cooling design,

original batteries are used in the pack with 1 mm spaces left between batteries for accommodating the PCM. For both battery packs, aluminum frames are used to wrap the batteries, and the dimensions of both packs are shown in the figures.

Two PCMs, *n*-octadecane and *n*-eicosane, with a purity of 99% from Sigma-Aldrich were used in this work, and their physical properties are listed in Table 3.1. In general, paraffin wax has a lower density at liquid state than the solid state; it will thus experience expansion during the melting stage. Therefore, liquid state PCM was injected into the mandrel before sealing, which eliminated the PCM expansion issue. To ensure the design is safe, we sealed a PCM-filled aluminum pipe (wall thickness of 0.2 mm, 1 mm deep groove on its side) with thermoplastic glue and polyurethane adhesive, as shown in the bottom center of Fig. 3.3. The pipe underwent 10 heating/cooling cycles in an oven (70°C) and ambient (23°C). During the test, no leakage was observed, and the outer diameter of the pipe remained constant during the test. In practical designs, stainless steel lids may be used to seal the pipes.

Table 3.1. Physical properties of n-octadecane, n-eicosane, and PCM/EG composite [107, 109, 139].

Property	<i>n</i> -octadecane	<i>n</i> -eicosane	PCM/EG
Specific heat, solid (J kg ⁻¹ K ⁻¹)	2150	2150	1864
Specific heat, liquid (J kg ⁻¹ K ⁻¹)	2180	2275	1964
Thermal conductivity, solid (W m ⁻¹ K ⁻¹)	0.358	0.425	7.85
Thermal conductivity, liquid (W m ⁻¹ K ⁻¹)	0.152	0.152	7.85
Density, solid (kg m ⁻³)	814	814	714
Density, liquid (kg m ⁻³)	724	771	714
Latent heat (kJ kg ⁻¹)	244	247	181
Melting temperature range (°C)	28.0-30.0	35.7-37.1	-

3.3 Experiment and Thermal Model

3.3.1 Fabrication of a Thermal Test Cell (TTC)

Considering the high level of complexity of both the material and equipment requirements in assembling a Li-ion battery, a TTC is usually fabricated in research to simulate the heat generation of a battery [140]. Fig. 3.3 shows the components in a TTC and the setup of the experiment. In the TTC, the stainless steel foil tape (3M™) acts as the heating component, which has a length of 2400 mm and width of 60 mm, and the thicknesses of the stainless steel layer and acrylic adhesive layer are 51 μm and 35 μm , respectively. The thicknesses were measured at different locations of the tape and they are uniform along the tape. The aluminum vial is used to contain the PCM. It was machined on a lathe with inner and outer radii of 3.5 and 3.95 mm, respectively. To fabricate the TTC, the foil tape was cleaned and dried with ethanol and tightly wrapped around the vial. The acrylic adhesive layer can ensure a minimal amount of air exists in between layers and prevent the stainless steel from short-circuiting itself. The detailed specification and physical properties of the TTC and its components are listed in Table 3.2.

Table 3.2. Specifications and physical properties of the thermal test cell.

Parameters	Value	Parameters	Value
St. steel thickness (μm)	51	St. steel specific heat ($\text{J kg}^{-1} \text{K}^{-1}$)	502
Adhesive thickness (μm)	35	St. steel thermal conductivity ($\text{W m}^{-1} \text{K}^{-1}$)	16.3
Foil length (mm)	2400	Adhesive specific heat ($\text{J kg}^{-1} \text{K}^{-1}$)	1470
Foil width (mm)	60.0	Adhesive thermal conductivity ($\text{W m}^{-1} \text{K}^{-1}$)	0.178
Foil weight (g)	61.4	Al specific heat ($\text{J kg}^{-1} \text{K}^{-1}$)	900
Vial outer diameter (mm)	7.9	Al thermal conductivity ($\text{W m}^{-1} \text{K}^{-1}$)	201
Vial inner diameter (mm)	7.0	Al density (kg m^{-3})	2700
Vial weight (g)	2.2	PCM volume (ml)	2.3
Cell outer diameter (mm)	18.6	Input power (W)	1.43, 3.27
Average density (kg m^{-3})	4597	Volumetric heat generation (W m^{-3})	107019,
Average specific heat ($\text{J kg}^{-1} \text{K}^{-1}$)	896		244723
Radial thermal conductivity ($\text{W m}^{-1} \text{K}^{-1}$)	0.431	Axial thermal conductivity ($\text{W m}^{-1} \text{K}^{-1}$)	9.74

Two groups of tests were performed on the TTC: a control group with an empty vial

and a group with the vial filled with PCM. To validate the cooling effectiveness of the internal BTM system and accuracy of the numerical model, two heating powers, 1.43 W and 3.27 W, were applied on the TTC through a power supply. Two k-type thermocouples were connected with a Pico-08 data logger to record the temperatures at a frequency of 1 Hz, and the layout is shown on the bottom left corner of Fig. 3.3, where T_s and T_c indicate the surface and center temperatures, respectively. To eliminate the temperature fluctuation due to air flow, T_s was taken at the layer adjacent to the surface layer. All the thermocouples were calibrated in ice water. The accuracy and resolution of the k-type thermocouples are $\pm 0.5^\circ\text{C}$ and 0.025°C , respectively.

For the TTC filled with PCM, a study of the PCM solidification time was also carried out using two PCMs, *n*-octadecane and *n*-eicosane under different convective cooling conditions (different air velocities). All of the tests were performed in a low-speed wind tunnel, which can provide a stable air flow with wind velocity up to 10 m s^{-1} .

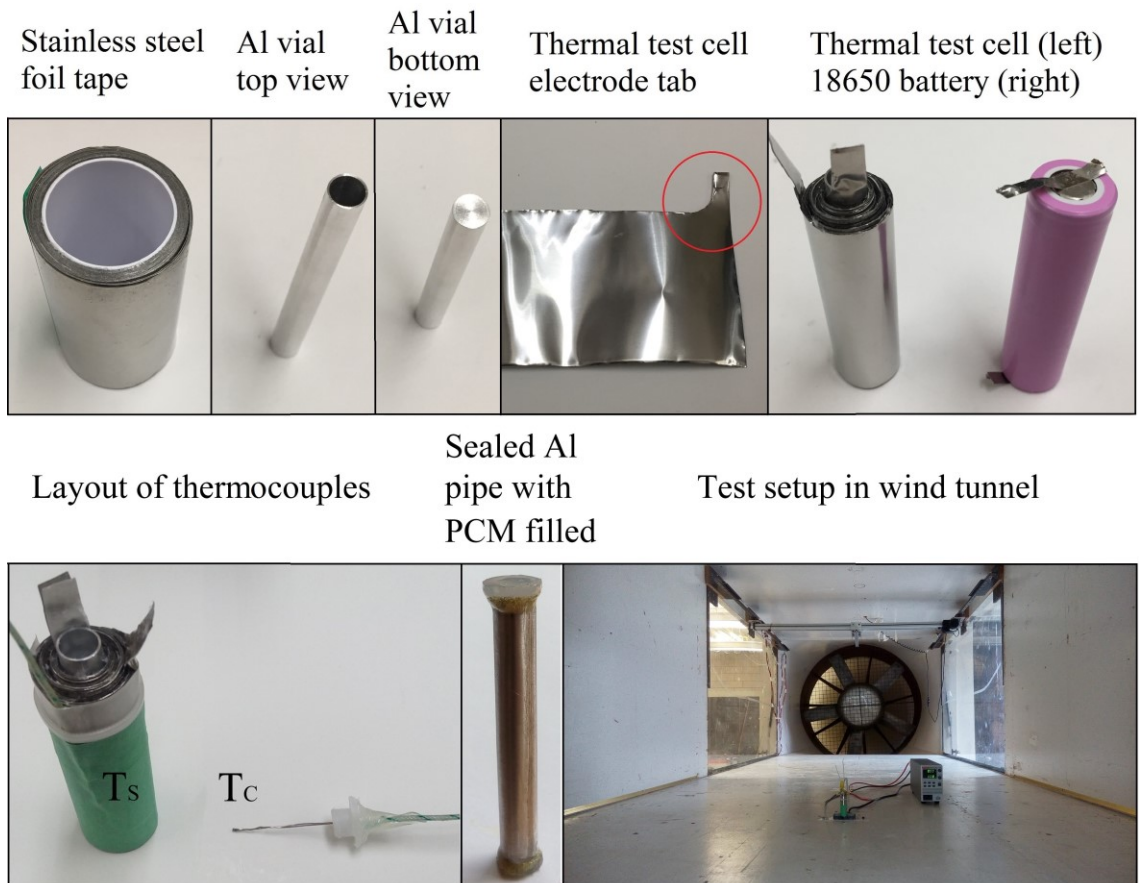


Figure 3.3. Photographs of the thermal test cell and its components, as well as the test setup.

The role of the TTC tests is to verify the effectiveness of the PCM-based internal cooling system and the accuracy of the model. Although the TTC and real battery (jelly roll) are different in their thermal properties, they are same in exterior geometries and both generate the heat through the roll. If the experimental results of the TTC tests agree well with the numerical results in different heating powers and cooling conditions, the model is credible to solve the energy balancing process that involve heat generation, phase change, and convection for batteries with different thermal properties. This is because the model is implemented to calculate the thermal-related equations explained in Section 3.3.2 using a set of known data for the meshed domains. If it can correct solve the equations with one set of data from the TTC, it is able to provide correct results with another set of data from the batteries.

3.3.2 Battery Heat Generation

The heat generation inside a Li-ion battery is a complicated process that involves electrochemical reaction heat, Joule heat, and reversible heat [51]. With detailed battery parameters, a delicate electrochemical and thermal coupling model could provide an accurate prediction of battery temperatures during discharges. Nevertheless, a constant heat generation rate is generally used during the design of a BTM system for simplicity [6, 9, 141], and it can be used for adequately examining the cooling performance of a BTM system.

In this work, a commercial cylindrical Li-ion battery was implemented to develop the model, and its physical parameters and heat generation rates were used in the model setup. Table 3.3 tabulates the specifications of the Li-ion battery. Prior to acquiring heat generation rates, the cylindrical battery was prerun at 24°C by cycling five times using a battery analyzer (PCBA 5010-4) with a cut-off voltage of 3 V and 4.2 V for discharging and charging, respectively. The constant charging and discharging currents were set to 1.3 A with a cut-off current of 50 mA at the potentiostatic stage.

Table 3.3. Specifications and parameters of the Samsung 18650 LiCoO₂ battery.

Parameter	Value	Parameter	Value
Nominal capacity (mAh)	2600	Cathode thickness (μm)	66.0
Nominal voltage (V)	3.63	Separator thickness (μm)	20.0
Height (mm)	65.0	Steel case thickness (mm)	0.300
Diameter (mm)	18.4	Radial thermal conductivity (W m ⁻¹ K ⁻¹)	1.97
Weight (g)	44.0	Axial thermal conductivity (W m ⁻¹ K ⁻¹)	28.1
Maximum discharge current (mA)	5200	Average cell specific heat (J kg ⁻¹ K ⁻¹)	830[35]
Discharge operating temperature (°C)	-20 – 60	Average jelly roll density (kg m ⁻³)	2580[35]
Steel rod diameter (mm)	2.50	Steel thermal conductivity (W m ⁻¹ K ⁻¹)	16.3
Jelly roll height (mm)	60.0	Steel specific heat (J kg ⁻¹ K ⁻¹)	502
Jelly roll length (mm)	650	Steel density (kg m ⁻³)	7861
Cu foil thickness (μm)	10.0	Frame thermal conductivity (W m ⁻¹ K ⁻¹)	201
Al foil thickness (μm)	18.0	Frame specific heat (J kg ⁻¹ K ⁻¹)	900
Anode thickness (μm)	72.0	Frame density (kg m ⁻³)	2700

To calculate the battery heat generation rates, the Samsung 18650 battery was insulated by wrapping air bubble insulating layers and discharged at currents of 2.5 A (0.96 C), and 5 A (1.92 C). A temperature logger (Pico TC-08) with K-type thermocouples was used to log battery surface temperature at a 1 Hz frequency, which was then combined with the energy balance equation to calculate the average heat generation rate:

$$P = \frac{Q}{\Delta t} = \frac{c_p m \Delta T}{\Delta t} \quad (3.1)$$

where c_p and m indicate the average specific heat and mass of the battery, respectively; Q is the total heat generated from the battery; Δt and ΔT are the battery discharge time and battery temperature change during the discharge, respectively. An assumption made here is that the heat loss during discharge from the insulating layers is negligible.

The volumetric heat generation rate, q , is calculated by dividing the heat generation rate P with the volume of the jelly roll (Li-ion battery reaction cell):

$$V = h_j(\pi r_2^2 - \pi r_m^2) \quad (3.2)$$

where h_j indicates the height of the jelly roll, r_2 and r_m represent the outer radii of the jelly

roll and steel mandrel, respectively. Table 3.4 summarizes the experimental results and the corresponding volumetric heat generation rates at the assigned discharge rates.

Table 3.4. Summary of the experimental results and the calculated heat generations of the 18650-type battery.

I (A)	ΔT (°C)	Q (J)	Δt (s)	P (W)	q (W m ⁻³)
2.5 (0.96 C)	18.83	687.7	3750	0.1834	12527
5 (1.92 C)	44.87	1639	1890	0.8672	59235

3.3.1 Thermal Model

The thermal model is governed by the energy conservation equation [21] given below for the Li-ion battery and TTC:

$$\rho c_p \frac{dT}{dt} = \nabla \cdot (k \nabla T) + q \quad (3.3)$$

where the first term is the heat stored in the battery/cell, k represents the thermal conductivity, and q indicates the volumetric heat generation rate.

In the equation, the thermal conductivities of the Li-ion battery and TTC in radial and axial directions are calculated through equations (3.4) and (3.5), respectively:

$$k_s = \frac{\sum_i l_i}{\sum_i \frac{l_i}{k_i}} \quad (3.4)$$

$$k_p = \sum_i \frac{l_i}{l} k_i \quad (3.5)$$

where the subscripts s and p indicate the properties in series and parallel directions, respectively. l_i is the thicknesses of different components in the cell, i.e., anode, cathode, separator, current collectors. l is the total thickness of the electrochemical reaction cell.

For the PCM region, the equations used in the simulation are given in Section 2.2.1 from (2.5) to (2.7).

The energy conservation equation of the steel case, hollow mandrel, and aluminum frame can be expressed the same as (3.3), but without the heat source term. As tested in Section 3.2, a 0.2 mm thick aluminum pipe can well handle the phase change of the PCM, the thickness can be further reduced in the future through advanced manufacturing processes on high mechanical strength stainless steel pipes. To simplify the simulation process, especially the meshing step for the thin pipe layer, PCM is directly embedded in the battery center in all the battery geometries used in the simulations.

For simulations involving convection cooling at battery or battery pack surface, the cooling is described by [21]:

$$k \frac{\partial T}{\partial x} = h(T - T_{amb}) \quad (3.6)$$

A finite element solver, COMSOL Multiphysics, was used to solve the temperature variations of the battery, TTC, and battery packs. A Solid Heat Transfer Model was selected to simulate the heat transfer and phase change processes in batteries and battery packs. The model solves the processes like a black box. With all the physical properties and meshed geometries, it can solve the time and spatial related equations given above. To discretize the geometry, extremely fine free triangular meshes were generated on the geometries. At the interfaces between the PCM (or air) and Li-ion battery, PCM (or air) and battery case, as well as PCM (or air) and aluminum frames, 10 inflation layers were generated to refine the interface meshes, as shown in the zoomed figures of Fig. 3.1a and b. Convergence studies were performed on all simulations to ensure that the grid sizes had no effect on the simulation results.

3.4 Results and Discussion

3.4.1 TTC Tests for Model Validation

In the tests, the TTC was heated for 1500 s and 1000 s under the heating powers of 1.43 W and 3.27 W, respectively. To create a similar environment as in a battery pack, where batteries are not directly exposed to ambient air for natural convection cooling, the TTC was placed inside a sealed cylindrical container during the test. The convective heat

transfer coefficient was determined by comparing the cooling curve of the TTC with the simulation, and a value of $9 \text{ W m}^{-2} \text{ K}^{-1}$ was obtained and used in the simulations. The convective heat transfer coefficient obtained is only related to the geometry of the heat source and its surface cooling condition, which is not affected by the physical properties of the heat source. In Fig. 3.4, the temperature curves of the TTC with and without the PCM added are obtained from experiments and simulations for comparison, where the dots indicate the experimental data (due to the high frequency of data acquisition, the dots turn to black solid lines) and the lines in other colors are the simulation results. In the figures, T_s and T_c represent the experimentally obtained surface and center temperatures of the TTC, while in simulations, T_1 , T_2 , and T_3 were recorded, and they are the temperatures at the center of the cooling core, at the corner of the cooling core, and at the TTC surface, respectively, and the corresponding positions are shown in the inset of Fig. 3.4a, which is the temperature contour of the PCM-filled TTC at the end of the 1.43 W heating test.

In the upper plots of Fig. 3.4a and b, the surface temperature curves of the TTC with and without PCM under the heating powers of 1.43 W and 3.27 W are plotted. It is seen that the simulation results agree well with the experiments for both heating powers. For the temperature curves in the TTC core, as shown in the lower plots of Fig. 3.4a and b, the simulation results (T_1) match well with the experiment (T_c) when the mandrel is empty, while discrepancy is observed at the phase transition stage in the PCM filled TTC, as shown in the inset of Fig. 3.4a bottom plot. This is because the buoyancy of the melted PCM may affect the location of the thermocouple. Consequently, T_c falls in between the core center temperature (T_1) and the core corner temperature (T_2).

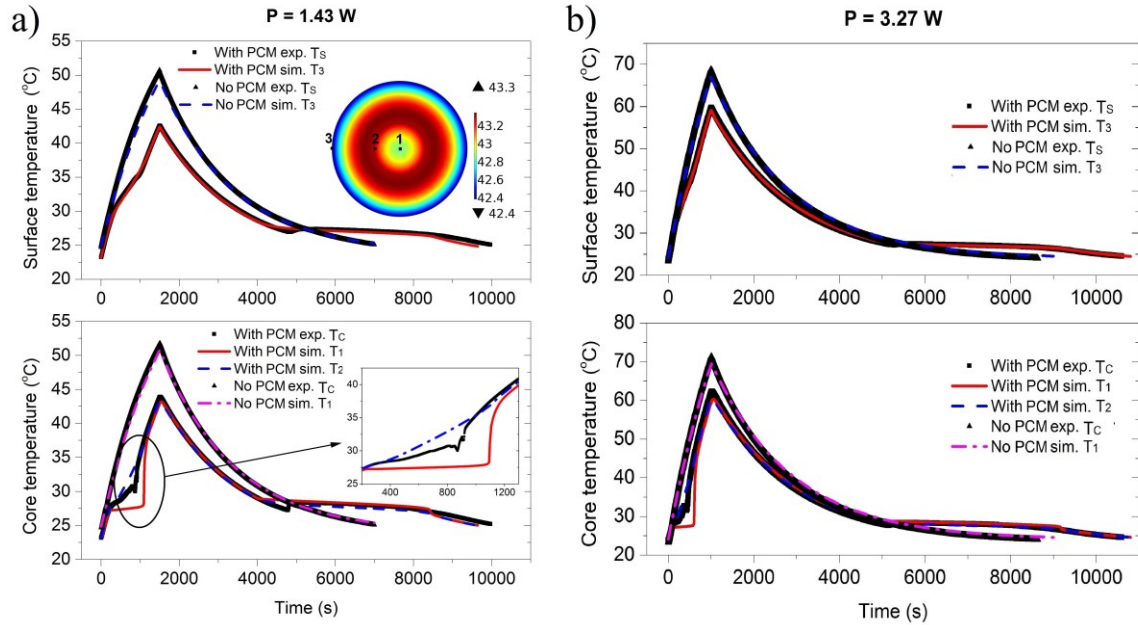


Figure 3.4. Comparisons of the experimental and simulated temperatures during the TTC tests at heating powers of a) 1.43 W and b) 3.27 W.

When comparing the temperature curves of the PCM embedded group and the blank control group, it is seen that the addition of PCM can decrease the maximum temperature by 8°C and 9°C under the heating powers of 1.43 W and 3.27 W, respectively. Compared to the TTC, the real Li-ion battery has a relatively low heat storage term, i.e., the ρC_p term of the real battery is about half that of the TTC, which will make the real battery more sensitive to the cooling capacity of the PCM in the mandrel. In addition, the real battery is more thermally conductive on both axial and radial directions than the TTC, as shown in Table 3.2 and 3.3, thus it is more effective in dissipating heat at the battery surface. Consequently, the reduction in the maximum temperature will be more notable for Li-ion batteries. The relevant numerical studies are carried out in Section 3.4.2. Furthermore, it is noticed that the PCM embedded TTC takes longer to cool after the heating tests compared to the blank control group due to the solidification of the PCM. This issue will be discussed and addressed in Section 3.4.3.

3.4.2 Simulations on a Single 18650 Li-ion Battery

With the validated model, simulations are then performed on a single battery. Fig. 3.5a and b show the temperature contours of the battery at the end of the 2.5 A discharge with the original design and the core cooling design. For both cases, the adiabatic boundary condition is applied to clearly view the cooling effect of the PCM on the battery. As can be seen, when replacing the hollow mandrel of the Li-ion battery with a PCM core, the maximum temperature has a slight drop of 1.46°C. The cooling capability of the PCM-based internal BTM system can be further improved by increasing the core size. The corresponding simulations are carried out on the battery by varying the radius of the PCM core from 2 to 5 mm, and the obtained temperature profiles during the 2.5 A and 5 A discharges are given in Fig. 3.5c and d, respectively. It is seen that as the discharge rate increases, more PCM is needed to maintain the battery temperature at a low level, and the cooling capability of the internal BTM system improves as the radius of PCM core increases. However, the improvement of cooling performance is achieved with a sacrifice to the battery capacity. To investigate this effect, the capacity ratio (θ) of the modified battery to the original battery described by (3.7) is plotted against the PCM core radius in Fig. 3.6.

$$\theta = \frac{\alpha\pi(r_{cell}^2 - r_{core}^2)}{\alpha\pi(r_{cell}^2 - r_m^2)} \quad (3.7)$$

where α is the volumetric battery capacity, r_{cell} , r_{core} , and r_m are the radiuses of the battery, PCM core, and mandrel, respectively.

As can be seen, the capacity ratio ranges from 100% to 70% as the PCM radius increases from 1.25 mm to 5 mm. Nevertheless, the space and weight saved in the compactly packed core cooling batteries will offset the sacrificed capacity at the pack level. In Section 3.4.4, the internal PCM-based BTM system will be further compared with the external PCM-based BTM system in their specific energies (energy per unit mass).

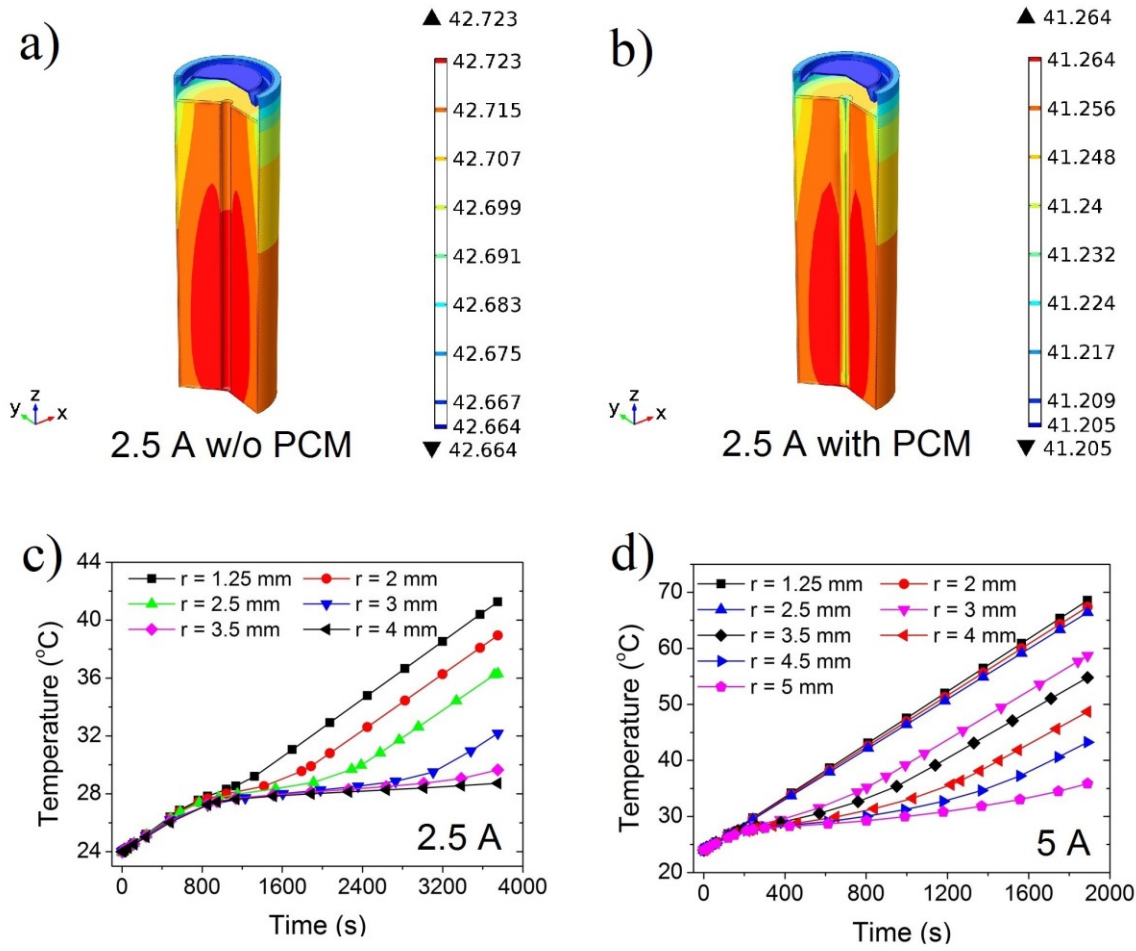


Figure 3.5. Simulation results of the single 18650 Li-ion battery: temperature contours of a) the original battery and b) the battery with a 1.25 mm PCM core at the end of the 2.5 A discharges; temperature curves of the battery embedding PCM core of different sizes during discharges at currents of c) 2.5 A and d) 5 A.

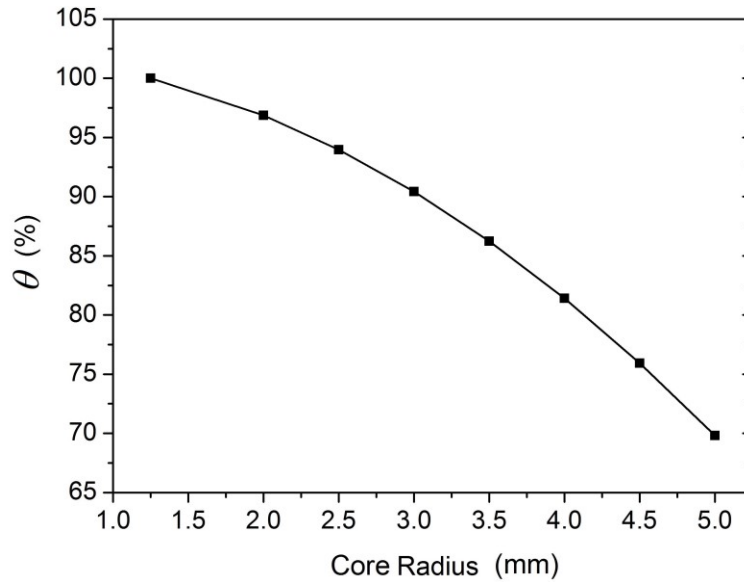


Figure 3.6. A plot of the capacity ratio against the PCM core radius.

Several research studies have emphasized the importance of using a thermally conductive PCM matrix in external cooling systems to exert their cooling potential [110, 111]. To investigate the effect of the conductive matrix on the internal cooling system, comparisons are made between batteries embedding a pure PCM core and a PCM/expanded graphite (EG) composite core. In Ref. [107], the PCM composite employed in the test is a mixture of RT44HC (a pure PCM) with EG that has a mass fraction of 20%. Because RT44HC has similar thermal properties as the n-octadecane used in this work except for the phase change temperature, the physical properties of the PCM/EG composite are adopted in the simulation, with the relevant physical properties given in Table 3.1.

In Fig. 3.7, the maximum and minimum temperatures of the Li-ion battery as well as the temperature at the PCM core center during the 2.5 A discharge are plotted for both batteries with cores of 3 mm radius. It is seen that with using the PCM/EG composite, the three temperature curves are overlapped, which is attributed to the fact that the high thermal conductivity of the PCM/EG composite can quickly even the temperatures between the Li-ion battery and the cooling core. As for the battery embedding a pure PCM core, although temperature differences are observed between the battery and PCM core during the PCM melting stage, the maximum and minimum temperature curves of the Li-ion battery are basically overlapped, which ensures a uniform temperature distribution across the

electrochemical cell. Interestingly, it is seen that the use of the high conductive PCM composite does not reduce the maximum temperature, and contrarily has a bigger temperature change than the pure PCM filled battery, with peak temperatures of 35.2°C and 32.3°C, respectively. This is because the addition of the conductive matrix will reduce the proportion of PCM, thus lowering the latent heat of the BTM system.

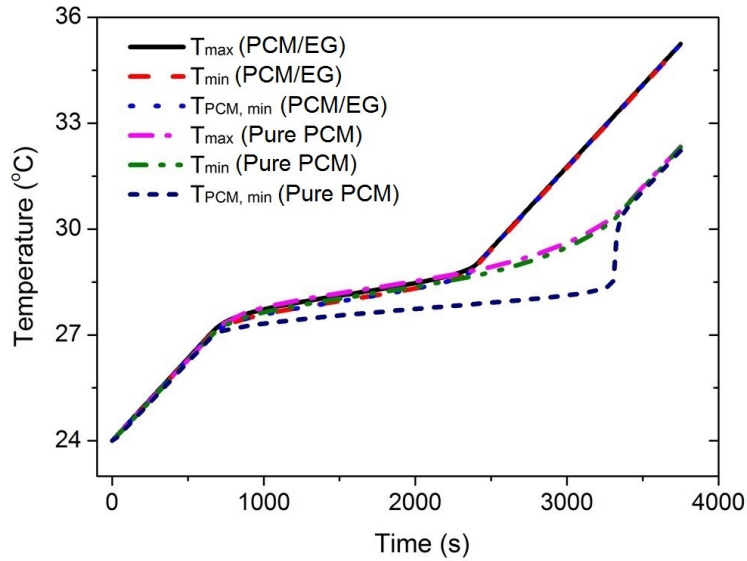


Figure 3.7. The comparison of the temperature curves of a single Li-ion battery embedding pure PCM and PCM/EG composite cores during a 2.5 A discharge.

In Fig. 3.8a and b, the liquid fractions of the pure PCM core and the PCM/EG composite core at the assigned times are shown. It is seen that the PCM in the composite core is fully melted at 2400 s, which is much shorter than the pure PCM (at 3300 s) due to its lower PCM content. To conclude, the conductive matrix is unsuitable for the core cooling system because the PCM core is thin, and the short heat transfer length ensures that the PCM can respond timely to the heat surge. Also, the use of a thermally conductive matrix will reduce the latent heat potential of the BTM system and will not play a positive role. In applications, pure PCM can be directly used to fill mandrels and used as cooling cores for cylindrical Li-ion batteries, which will eliminate the manufacturing cost of the thermally conductive matrix.

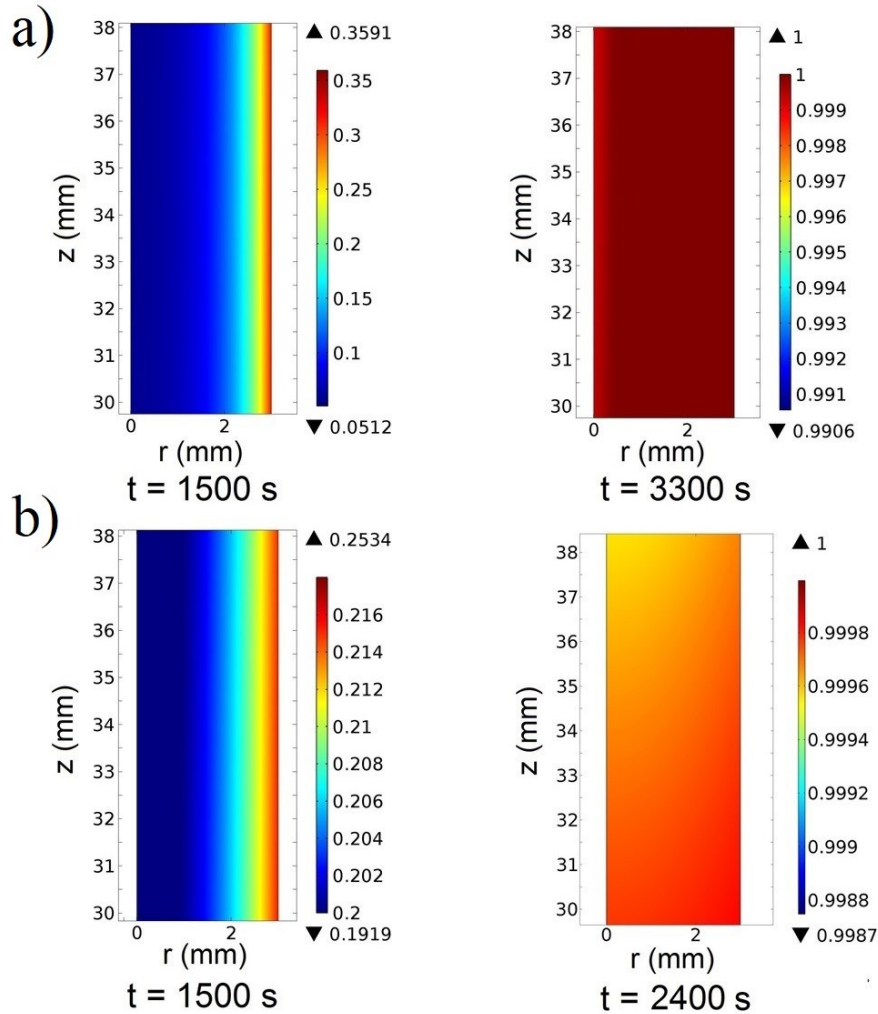


Figure 3.8. The liquid fractions of a) pure PCM and b) PCM/EG composite at the assigned times during the 2.5 A discharge.

3.4.3 Solidification of the PCM Core

Besides keeping the battery temperature at a low level, the BTM system should also be able to be restored to its initial state as quickly as possible after discharging to ensure a proper operation in the following cycles. To investigate the solidification process of the PCM in the internal BTM system, the TTC was tested in a low-speed wind tunnel under different wind velocities, and the temperature at the PCM core center was recorded for comparison, as shown in Fig. 3.9a, where the wind velocity was measured by a hot-wire anemometer. It is seen that the time spent for cooling was significantly reduced as natural convection turned to forced convection. At a wind velocity of 3 m s^{-1} , it only took 2330 s

to restore to the initial state, and the further increase in wind velocity did not play a dominant role.

In the tests, it was observed that the melting temperature of the PCM can also affect the solidification time. To study its effect, the PCM in the TTC was changed from *n*-octadecane to *n*-eicosane, which has a higher melting temperature of 35.7°C, and a series of cooling tests were carried out under a heating power of 3.27 W, as shown in Fig. 3.9b. Attributing to its higher melting temperature, thus a higher heat dissipation rate during the solidification, it is quicker for the TTC to restore to its initial state. For example, when tested in the sealed container, the solidification time after replacing the *n*-octadecane by *n*-eicosane reduced from 9600 s to 7800 s, which is close to the cooling time of the original battery, 7640 s, as shown in Fig. 3.4b.

In addition, it is seen that the temperature has a concave shape during solidification, for example, at around 2500 s and 5000 s of the red and black curves in Fig. 3.9b, respectively. This phenomenon is probably due to a supercooling effect. When the liquid PCM on the thermocouple starts to freeze, the formation of nucleuses absorbs energy and lowers the temperature. Because the thermocouple may not be exactly located at the PCM core center, after the solidification of the PCM on the thermocouple, the temperature of the thermocouple bounces back. The supercooling effect was not observed on the blue and green curves in Fig. 3.9b, which is because the effective forced convection cooling makes the PCM remain solid on the thermocouple during the entire test.

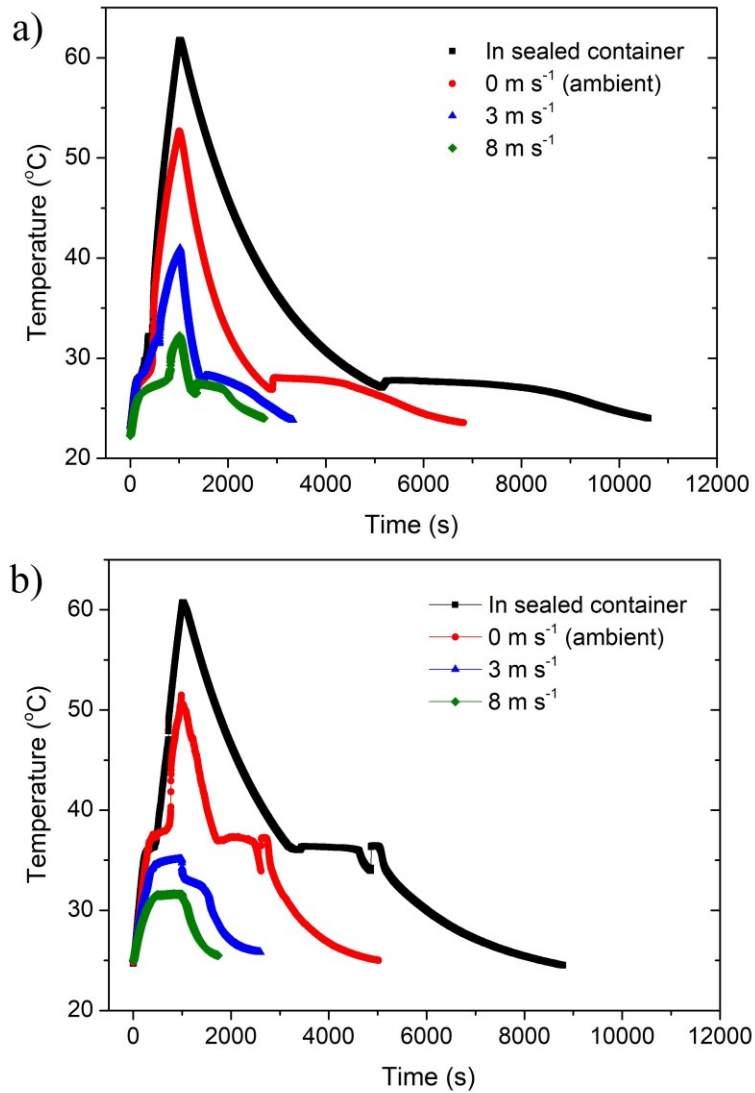


Figure 3.9. Experimentally recorded PCM core temperature curves of the TTC filled with a) n-octadecane and b) n-eicosane during the 3.27 W tests under different cooling conditions.

An intense heating and cooling cycle test was then carried out on the *n*-eicosane filled TTC under an ambient condition (0 m s^{-1}). The cycle test was first run under a heating power of 1.43 W, with the heating and cooling time lengths of 1500 s, as shown in Fig. 3.10a. It is seen that the temperature of the TTC becomes stable after the first cycle. As the heating power increases to 3.27 W, the heating and cooling times were adjusted to 1000 s and 2000 s, respectively. As shown in Fig. 3.10b, the PCM cannot be fully solidified due to the insufficient time allocated for cooling. Nevertheless, the TTC operates stably after the third cycle.

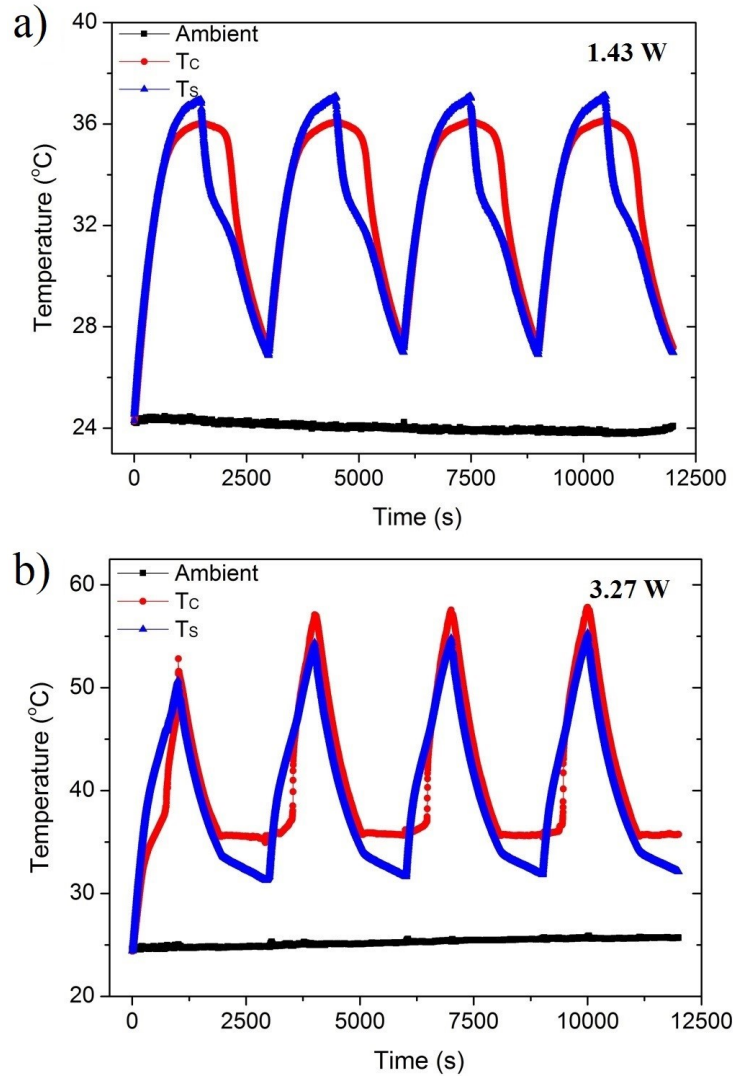


Figure 3.10. Cycle tests of the n-eicosane filled TTC under heating powers of a) 1.43 W and b) 3.27 W.

3.4.4 Core Cooling vs. External Cooling

An effective PCM-based BTM system should also have the capability of maintaining the temperature and temperature difference of battery packs at a low level while using the minimal amount of PCM. In this section, the internal and external BTM systems are compared on a 4-layer battery pack, as shown in Fig. 3.1. For the external BTM system, both the pure PCM and PCM/EG composite are studied. In simulations, both battery packs

are discharged at a rate of 5 A with a natural convection boundary condition ($h = 10 \text{ W m}^{-2} \text{ K}^{-1}$) applied on the top and bottom surfaces of the packs.

In Fig. 3.11, the maximum temperature and temperature difference curves of the 4-layer battery pack under internal and external cooling conditions are shown. Among three cooling designs, the battery pack equipped with the internal BTM system has the lowest peak temperature, which is 0.42°C and 2.57°C lower than the external cooling systems that employ pure PCM and PCM/EG composite, respectively. In the bottom plot of Fig. 3.11, it is seen that the use of PCM/EG reduces the temperature difference in the external system. Among the three cooling designs, the internal BTM system provides the most uniform temperature distribution for the battery pack, with the maximum temperature difference below 3°C .

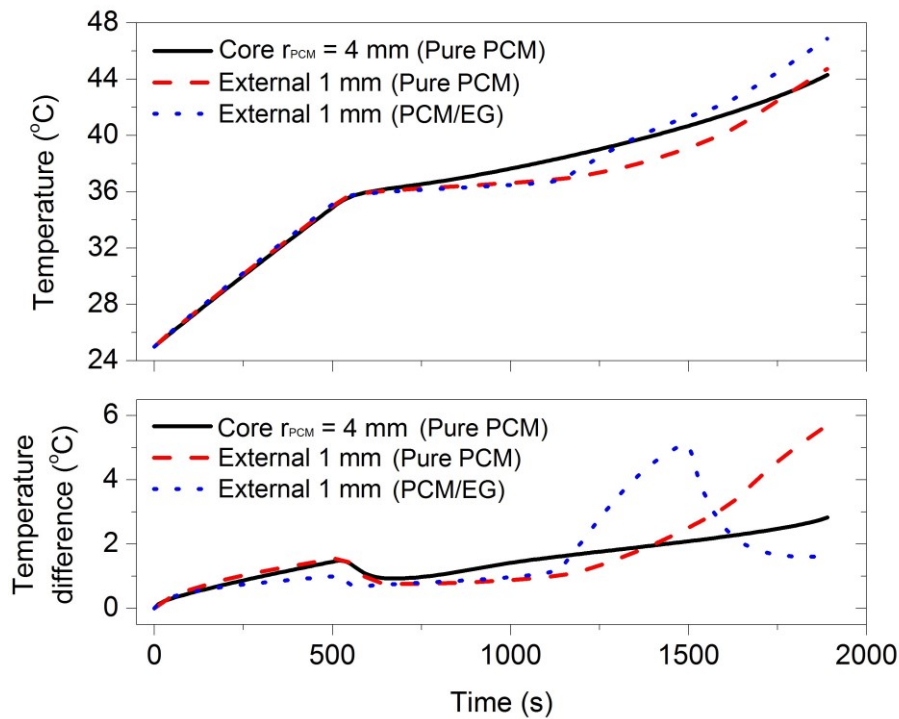


Figure 3.11. Maximum temperature and temperature difference curves of the 4-layer battery pack equipped with internal and external BTM systems.

Finally, PCM usage and the normalized specific energy of the battery pack equipped with three BTM systems are compared in Table 3.5, in which the PCM amount is calculated based on the PCM area, and the normalized specific energy (NSE) is calculated by dividing

the specific energy of the battery pack equipped with BTM systems by that of the original battery pack, which can be expressed by the following equation:

$$NSE = \frac{SE_w}{SE_o} = \frac{\frac{\alpha A_{cell,w}}{A_{PCM}\rho_{PCM,l} + A_{cell,w}\rho_{cell}}}{\frac{\alpha A_{cell,o}}{A_{cell,o}\rho_{cell}}} = \frac{1}{1 + \frac{\rho_{PCM,l}}{\rho_{cell}} \frac{A_{PCM}}{A_{cell,w}}} \quad (3.8)$$

where SE is the specific energy, A indicates the area, α represents the volumetric battery capacity. The subscript w , o , and l mean battery packs with BTM systems, the original battery pack, and the liquid state PCM, respectively.

Table 3.5. Comparisons of the performance indicators of core and external cooling systems.

BTM systems	PCM amount (mm ²)	NSE	Peak temperature (°C)	Peak temperature difference (°C)
Core ($r_{PCM} = 4$ mm)	603	0.930	44.3	2.84
External (pure PCM)	953	0.911	44.7	5.69
External (PCM/EG)	953	0.917	46.9	5.10

Among three cooling designs, the core BTM system consumes the least amount of PCM. Meanwhile, owing to its efficient use of the PCM, the core cooling system has a higher NSE value than that of the other two external cooling designs, indicating that the core cooling design is the most lightweight design. To sum up, the proposed PCM-based core BTM system is a lightweight design that uses the least amount of PCM and is able to control the temperature rise and difference of the battery pack at low levels.

3.5 Summary

A PCM-based internal BTM system is proposed in this Chapter for cylindrical Li-ion batteries. Both experiments and simulations are performed to verify the effectiveness of the design in cooling and its strengths over the PCM-based external BTM systems. The concluding remarks of this design are summarized as follows:

- 1) The PCM-based internal BTM system is safe and feasible for cylindrical battery applications.
- 2) The addition of a PCM core can effectively alleviate the temperature rise and achieve a uniform temperature in both batteries and battery packs.
- 3) An appropriate PCM is helpful in reducing the solidification time and ensuring a safe operation in continuous cycles.
- 4) Battery packs equipped with PCM cores consume less PCM and have higher specific energy, lower temperature rise, and more uniform temperature distribution than packs equipped with PCM-based external BTM systems.
- 5) The internal BTM system is simple in design and can directly employ pure PCMs as its cooling medium, which reduces the complexity of the system and the relevant cost.

Chapter 4. Optimization of the PCM-Based BTM System on Li-ion Battery Packs

4.1. Overview

An effective and compact thermal management system is essential for modern lithium-ion (Li-ion) battery-powered vehicles, which involve rigorous constraints on weight and volume. In this Chapter, the PCM-based internal battery thermal management (BTM) system introduced in Chapter 3 is numerically studied on a Li-ion battery submodule consisting of 40 cylindrical batteries. Variables including PCM core size and PCM core size distribution are optimized in the BTM system to achieve a better cooling performance. The results show that the PCM cores can effectively alleviate the temperature rise inside the battery pack, and a uniform temperature distribution can be obtained when thicker PCM cores are embedded in the interior batteries. A battery pack compactness study indicates that the internal BTM system is a space-saving design that facilitates the achievement of a high energy density in the battery pack. Finally, an air cooling system is integrated with the PCM-embedded battery pack to form a hybrid cooling system, and its cooling performance is examined in a conjugate heat transfer model.

4.2. Battery Pack Description

Fig. 4.1a gives the geometry of a submodule with 40 cells assembled in parallel. Four rows of cells are closely arranged in the battery pack to achieve a high energy density. A 2 mm thick aluminum frame physically retains the cells, and it also serves as the outer surface for convection cooling. The vacancies in the upper-left and lower-right corners of the battery pack are left for wiring and fixation intents. The “o” and “i” in the schematic indicate the locations of the cells in the module and will be discussed in Section 4.4 for BTM system optimization purposes. In Fig. 4.1b, a hybrid cooling design is introduced into the battery pack by integrating air cooling. The red line on the left of the pack indicates the inlet, while the blue line on the right represents the outlet. For these two battery packs, all relevant dimensions are shown in the figure. Simulations are also carried out on the

battery pack consisting of original batteries for comparison, and the battery layouts are kept the same with the battery pack shown in Fig. 4.1a & b.

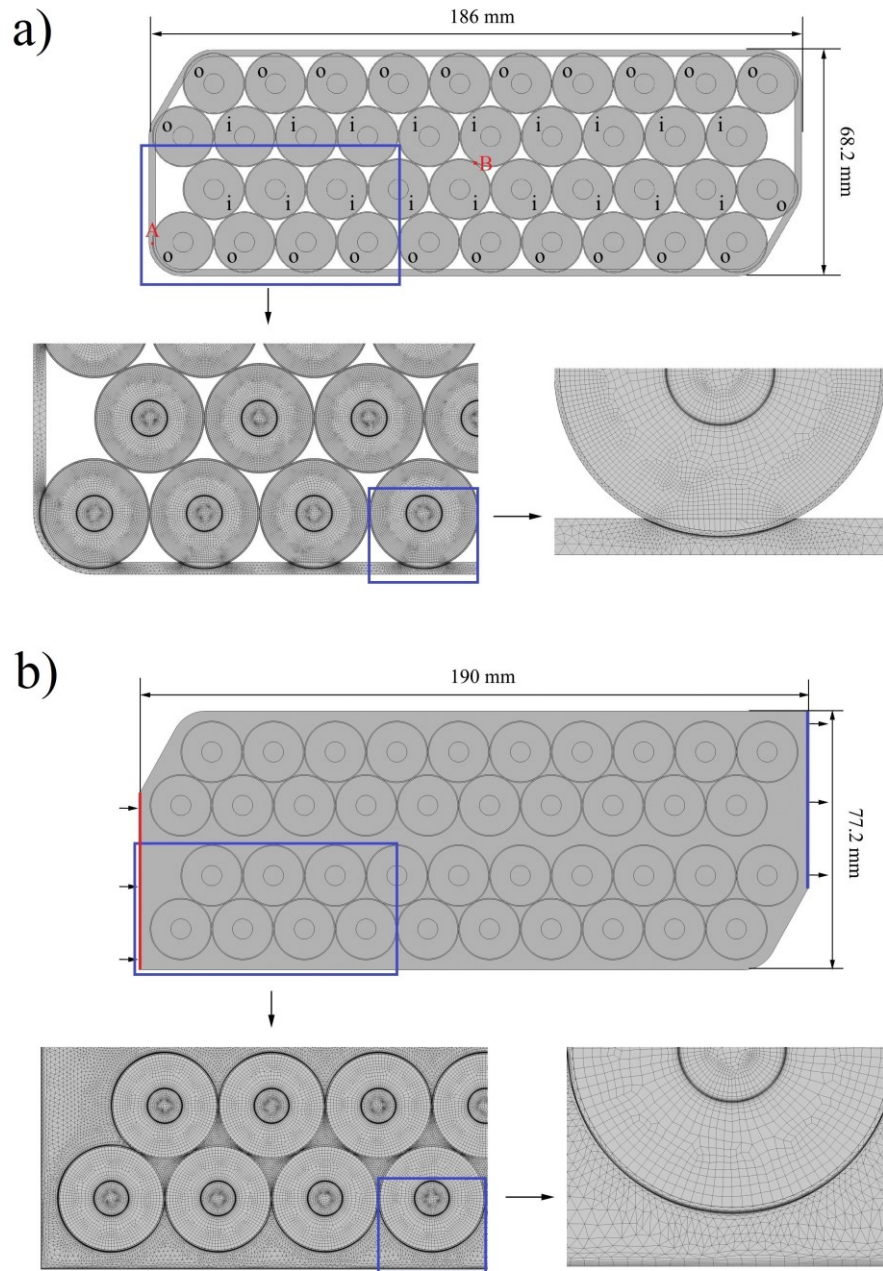


Figure 4.1. a) Schematic illustration of a passively cooled 40-cell battery pack; b) Schematic illustration of a hybrid cooling design for the battery pack.

The proposed PCM-based internal BTM system has the following advantages versus the external passive BTM system: 1) the battery roll can be directly wrapped on the cooling

core during the battery manufacturing stage, which is simpler than external PCM matrix designs; 2) instead of using PCM/metal foam or PCM/EG matrix, pure PCM can be directly used as the cooling material in the core due to the short heat transfer length, which ensures a high latent heat and low cost; 3) the BTM system is a compact design and once built, no maintenance would be required; 4) the modified battery has the same appearance as the original battery, which improves the flexibility of integrating other BTM systems, such as forced air or liquid cooling systems, into the battery module.

4.3. Model Setup

The Solid Heat Transfer Model described in Chapter 3 is used in this Chapter to simulate the thermal responses of the battery packs and phase changes in the cores. When considering the forced air cooling, a 2D conjugate heat transfer model is employed. The model includes a fluid zone and solid zone to model the cooling air and batteries. The Reynolds stress and renormalization group turbulent model, $k-\varepsilon$ model, was employed to obtain the flow field of cooling air between batteries. The boundary conditions are velocity inlet ($u = 1 \text{ m s}^{-1}$, $T_{\text{in}} = 24^\circ\text{C}$), pressure outlet (0 gauge static pressure), no-slip at wall surfaces, and insulated top and bottom walls. For the simulations, the initial condition is:

$$T = T_0 = 24^\circ\text{C} \quad (4.1)$$

When generating the meshes, the same inflation layers as in Chapter 3 were also created at the interfaces. Grid sensitivity studies were carried out to ensure the simulation results are independent of the grid size. Sample meshes are shown in Fig. 4.1a and b, and a total number of 186,477 and 254,316 grids were generated for these two designs, respectively.

4.4. Results and Discussion

4.4.1 Battery Performance Index

The cooling performance of a BTM system can be evaluated by using the following indices: T_{peak} , ΔT , t_s , ξ , and θ , which mean the peak temperature during discharge, the

maximum temperature difference among batteries, the PCM solidification time, the space utilization ratio (the battery volume over the battery pack volume), and the capacity ratio (the volumetric capacity of the battery pack equipped with the BTM system over the original battery pack), respectively. The first three parameters need to be minimized while the last two should be maximized in the BTM system. Sections 4.4.2 to 4.4.3 discuss the optimization of the passive cooling design (Fig. 4.1a). The simulation results of the hybrid cooling design (Fig. 4.1b) are given in Section 4.4.4. The space utilization of different designs is discussed and compared with previous works in Section 4.4.5.

4.4.2 PCM Core Size

For PCM-embedded batteries, although the increase of the PCM core size can enhance the cooling capacity of the system, overloaded PCM will lower the overall energy density of the battery system. The design criteria provided by the industrial partner for this project is to manage the peak temperature of the battery pack below 50°C under an unfavorable cooling condition ($h = 1 \text{ W m}^{-2} \text{ K}^{-1}$) during a 1.92 C discharge.

The maximum temperature profiles of the battery pack loaded with different amounts of PCM during 0.96 C and 1.92 C discharges are compared in Fig. 4.2a and b, respectively. It is seen that for the 0.96 C discharge, the peak temperature becomes stable at 36°C as the PCM radius increases to 2.5 mm. For the 1.92 C discharge, the peak temperature can be maintained below 50°C as the PCM radius reaches 3.8 mm. For both discharge rates, significant temperature drops can be observed after incorporating the PCM cores into the battery pack.

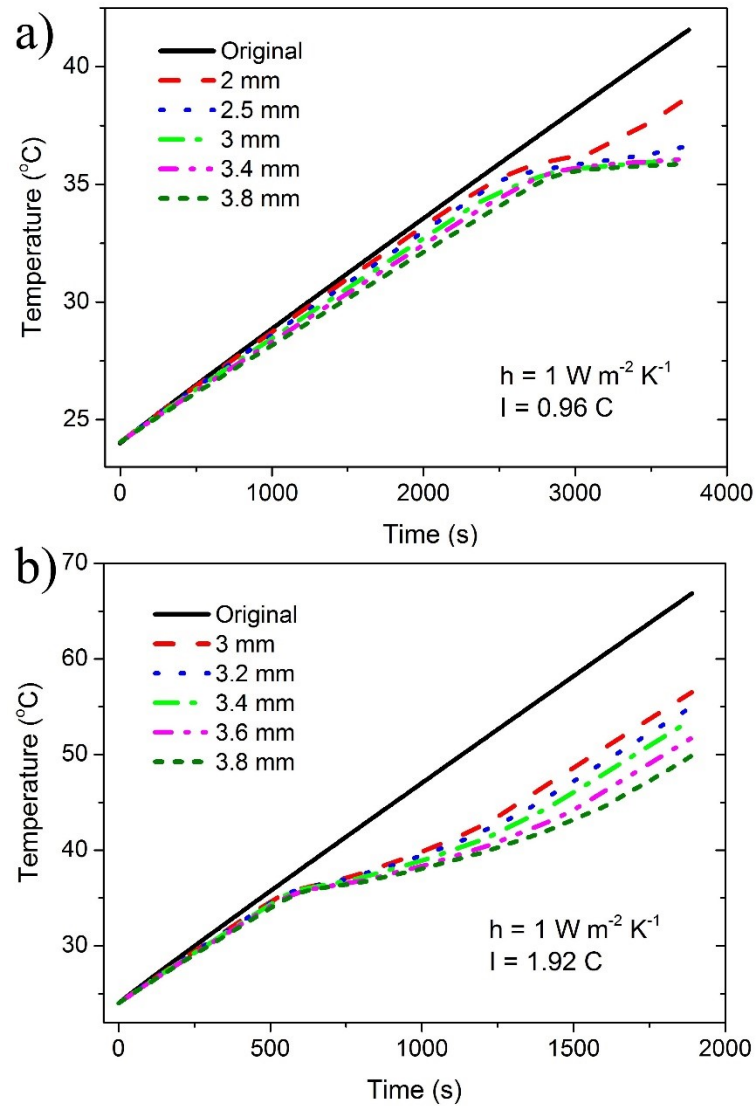


Figure 4.2. Maximum temperature profiles of the battery pack embedded with PCM cores of different sizes during a) 0.96 C and b) 1.92 C discharges.

A uniform temperature distribution across battery packs is also desirable to ensure the evenness of the capacity fading rate between batteries and to improve the reliability of the battery system. In simulations, bigger temperature differences can be found in the high-rate discharged battery pack under a natural convection condition ($10 \text{ W m}^{-2} \text{ K}^{-1}$). In Fig. 4.3, the maximum and minimum temperatures of the 40 batteries and the corresponding temperature differences at the end of 1.92 C discharge are plotted versus the PCM core radius. It is seen that the incorporation of the PCM core can effectively improve the temperature uniformity inside the battery pack. As the PCM radius increases to 3.8 mm,

the maximum temperature difference reduces to 3.24°C, which is 1.23°C lower than the original battery pack. Compared to the original battery pack, the PCM cores in the modified battery pack can provide an additional cooling source for the battery pack besides the natural convection and are helpful in alleviating the heat accumulation.

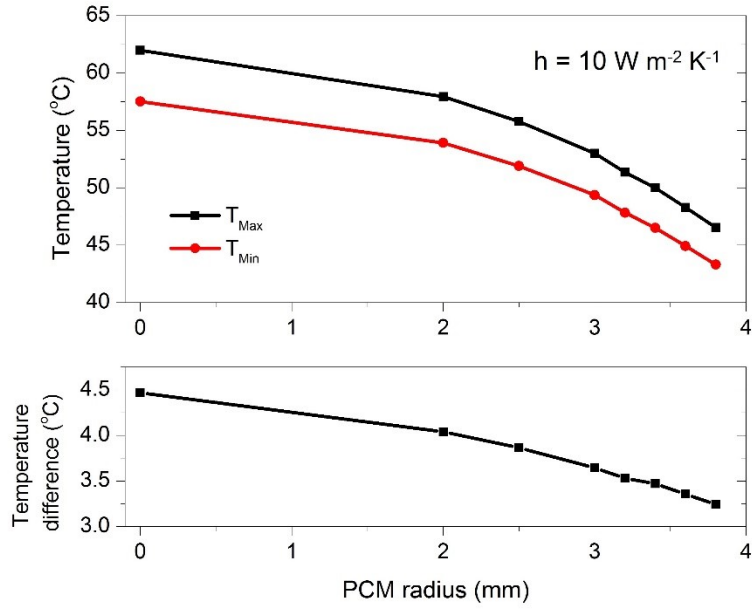


Figure 4.3. Plots of the maximum and minimum temperatures, as well as the temperature differences of the batteries embedded with PCM cores of different sizes at the end of a 1.92 C discharge.

4.4.3 PCM Core Size Distribution

In previous simulations, all the cells in the battery pack have the same PCM core size. Though it shows significant improvements compared to the original battery pack, the temperature uniformity within the battery pack can be further improved if the PCM core size for different batteries could be determined based on their heat dissipation environments. Fig. 4.4a shows the temperature contour of the battery pack using uniform 3.8 mm PCM cores. Higher temperatures can be observed in batteries located at the pack center. Thus, the batteries are divided into two groups, “i” and “o” as shown in Fig. 4.1a, which represent the batteries that only contact with batteries and the batteries that also contact with the pack case, respectively. In total, there are 18 “i” cells and 22 “o” cells.

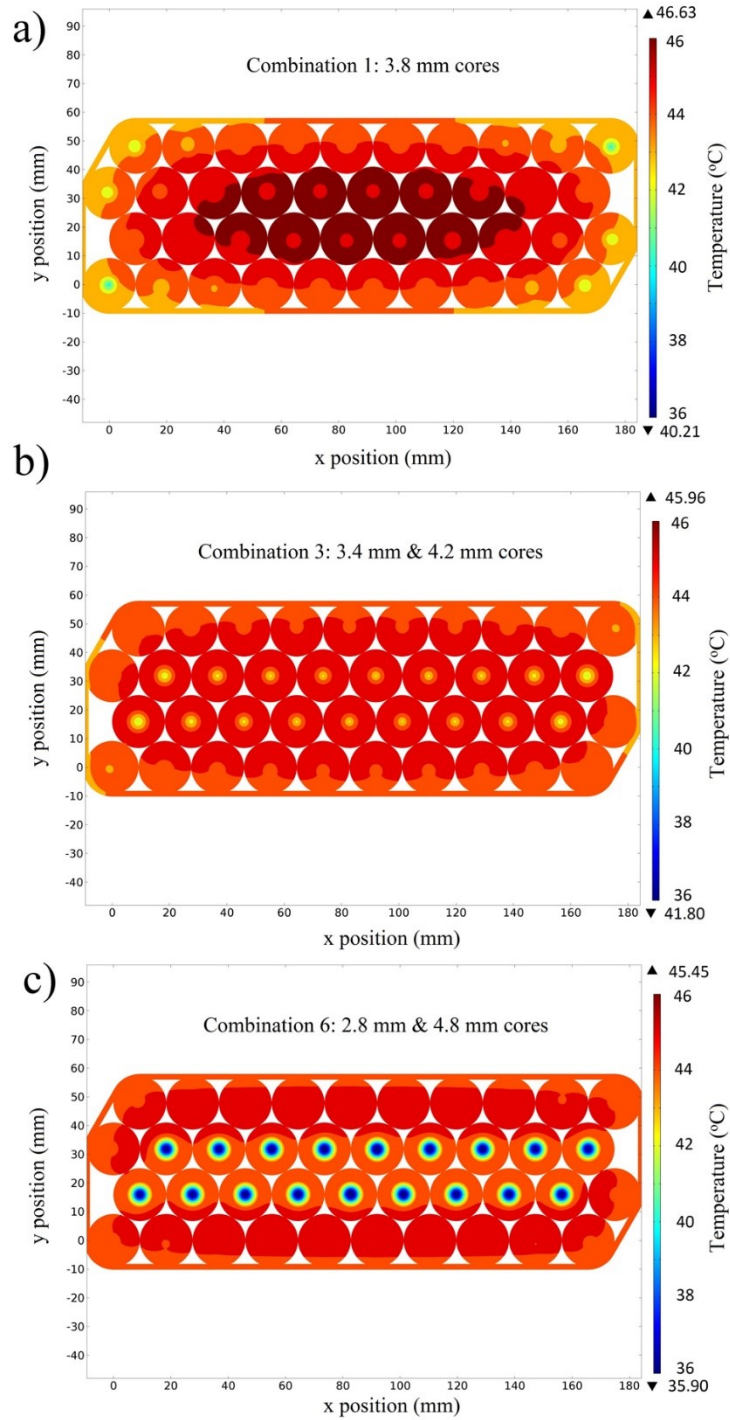


Figure 4.4. Temperature contours of the battery pack using different core size combinations at the end of a 1.92 C discharge under natural convection condition.

To fully exert the cooling potential of the PCM cores and even the temperature distribution inside the battery pack, thicker PCM cores are embedded in the “i” batteries,

while thinner cores are incorporated in the “o” batteries. With the change of the core sizes, the total PCM volume varies slightly. Fig. 4.5a shows the PCM volume ratio of different combinations to the pack with uniform 3.8 mm PCM cores. It is seen that the combination 3 ($r_o = 3.4$ mm & $r_i = 4.2$ mm) consumes the least PCM while the combination 6 ($r_o = 2.8$ mm & $r_i = 4.8$ mm) uses the most PCM. Six sets of combinations were simulated in this work. More combinations of inner and outer cores will be studied in the future work.

In Fig. 4.5b and c, the temperature differences between points A (marked in Fig. 4.1a, battery pack center) and B (battery pack corner) of the battery pack when using different PCM core size combinations during a 1.92 C discharge are plotted for comparison. Under the natural convection condition, it is found that the increase of PCM core size in the “i” batteries is effective in reducing the temperature difference. However, when h equals to $1 \text{ W m}^{-2} \text{ K}^{-1}$, too thick PCM cores in the “i” batteries lead to a lower temperature at the battery pack center than the corner and eventually make the temperature difference bigger.

The temperature contours of the selected three combinations (3.8 mm, 3.4 mm & 4.2 mm, and 2.8 mm & 4.8 mm) at the end of a 1.92 C discharge under natural convection are shown in Fig. 4.4a, b & c, respectively. It is seen that the rearrangement of the PCM size can effectively alleviate the heat accumulation at the battery pack center. Particularly, the combination of 3.4 mm and 4.2 mm cores achieves a highly uniform temperature distribution across the entire battery pack with the maximum temperature difference between jelly rolls within 2°C . Meanwhile, at the end of the discharge, the PCM is fully melted while having a close temperature to the jelly rolls. This further proves that the pure PCM can be directly used to fill the cooling core with an excellent performance, which makes the design feasible, cost-effective, and competitive.

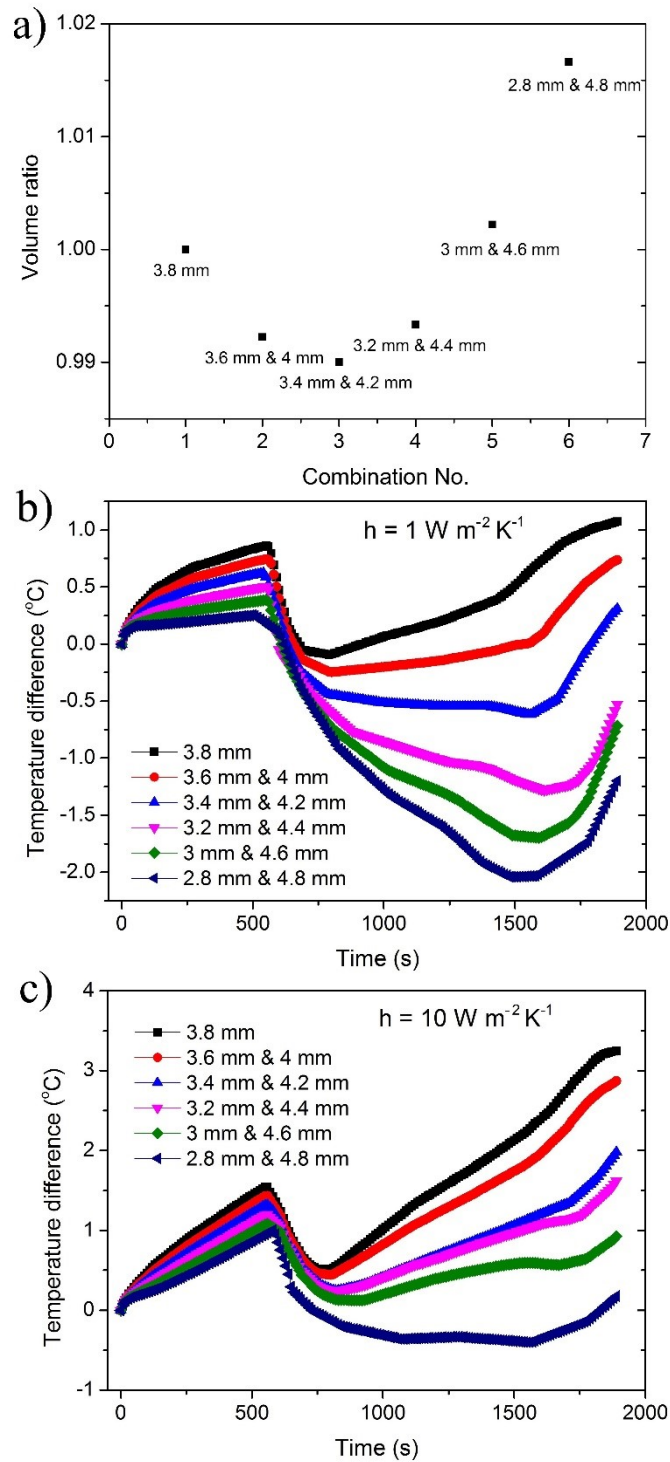


Figure 4.5. a) The PCM volume ratio of different core size combinations to the combination with uniform 3.8 mm cores; The temperature difference curves between points A and B in the battery pack using different core size combinations during the 5 A discharge under convective cooling with h of b) $1 \text{ W m}^{-2} \text{ K}^{-1}$, and c) $10 \text{ W m}^{-2} \text{ K}^{-1}$.

Although thicker PCM cores can mitigate the heat accumulation at the battery pack center, too thick PCM cores (e.g., $r = 4.8$ mm) are not suggested for the “i” batteries, which is due to the following reasons: more PCM is consumed in the BTM system; it leads to bigger temperature differences at low h values; and it does not fully utilize the latent heat of the PCM, as shown in Fig. 4.6. It is seen that the PCM in the “i” batteries is not fully melted at the end of a 1.92 C discharge.

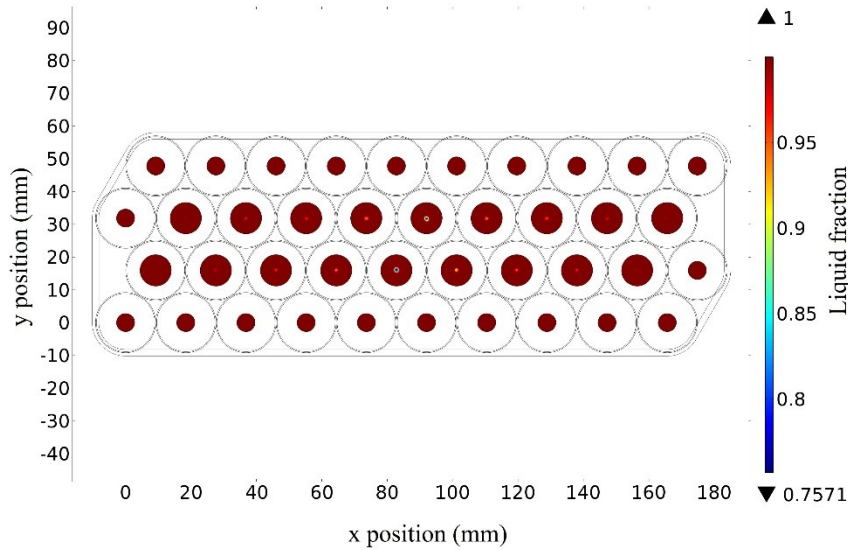


Figure 4.6. The liquid fraction of PCM cores (2.8 mm & 4.8 mm combination) at the end of a 1.92 C discharge under natural convection condition.

The optimized battery pack with embedded 3.4 mm & 4.2 mm PCM cores then undergo simulations with higher h values to study the corresponding thermal responses. In Fig. 4.7, the maximum temperature and temperature difference curves during a 1.92 C discharge are plotted. It is seen that as the h value increases to 30 and 50 $\text{W m}^{-2} \text{K}^{-1}$, the maximum temperature difference increases to 4.79°C and 5.55°C, the peak temperature decreases to 41.67°C and 39.71°C and the time spent for the battery module to restore to the initial state reduces to 8130 s and 4940 s, respectively.

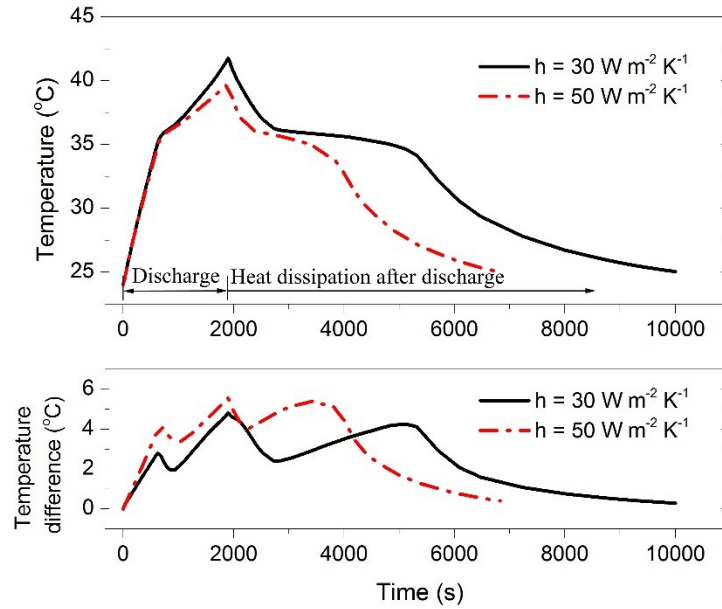


Figure 4.7. The maximum temperature and temperature difference profiles of the modified battery pack during a 1.92 C discharge during forced convective cooling conditions.

4.4.4 Hybrid Cooling System

One merit of the core cooling design is that it does not alter the appearance of cylindrical batteries, which facilitates the integration of additional cooling systems to improve the robustness of the BTM system to overcome the overheating issues of the battery system during high-intensity discharge scenarios. In this section, a forced air cooling system is introduced and combined with the PCM-based internal BTM system to form a hybrid BTM system, as shown in Fig. 4.1b. Simulations are carried out on both the original battery pack and the PCM-embedded battery pack for comparison.

In Fig. 4.8, both battery packs are compared in terms of their temperature and temperature difference profiles under a forced-air cooling condition with an inlet air velocity of 1 m s^{-1} . It is seen that after replacing the original cells with PCM-embedded cells, the thermal performance of the battery packs is remarkably improved. The peak temperature drops from 47.4°C to 39.38°C and the maximum temperature difference reduces from 10.8°C to 4.7°C .

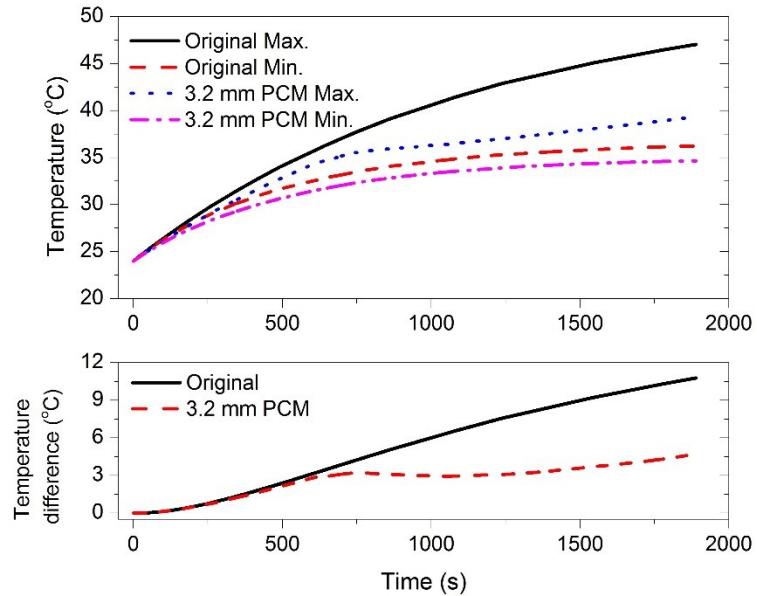


Figure 4.8. Comparisons of the temperature and temperature difference profiles of the original battery pack and the PCM-embedded battery pack cooled by air.

Figure 4.9a and d compares the temperature contours of the cells in two battery packs at the end of a 1.92 C discharge. It is seen that after replacing the original cells with the modified cells, the temperature distribution within the battery pack becomes more uniform. Due to the higher battery temperature, the cooling air along the channel in the original battery pack is more heated than the modified battery pack, as shown in Fig. 4.9b and e, which finally causes an insufficient cooling of the batteries close to the exit. Figure 4.9c and f show the velocity contours of the two battery packs. Since the batteries are the same in appearance, the velocity distributions inside these two battery packs are almost identical. The maximum velocity in the original battery pack is slightly larger due to the higher air temperature.

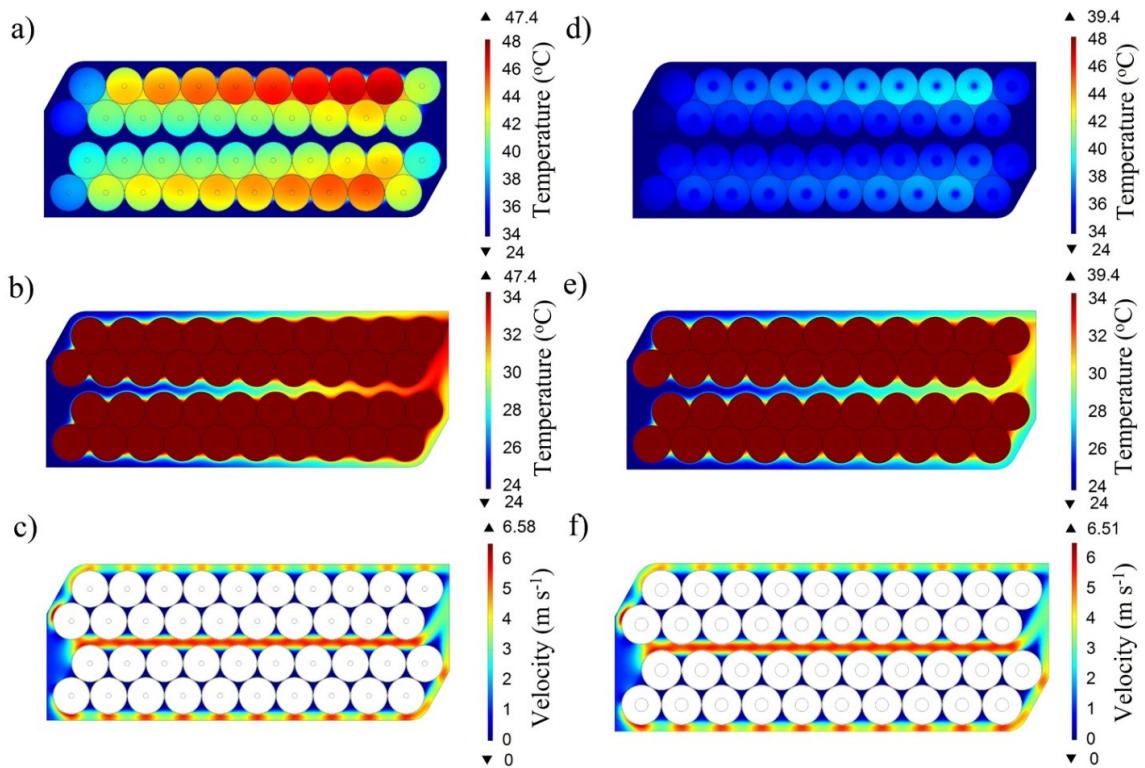


Figure 4.9. The temperature contours of the cells in a) the original battery pack and d) the modified battery pack; The temperature contours of the air in b) the original battery pack and e) the modified battery pack; The velocity contours of the air in c) the original battery pack and f) the modified battery pack.

In Fig. 4.10, the maximum temperature profiles of the hybrid cooled battery pack during a 1.92 C discharge are plotted. It is seen that the additional forced air cooling can quickly dissipate the heat stored inside battery module during the discharge process. It takes only 3762 s to manage the maximum temperature below 25°C.

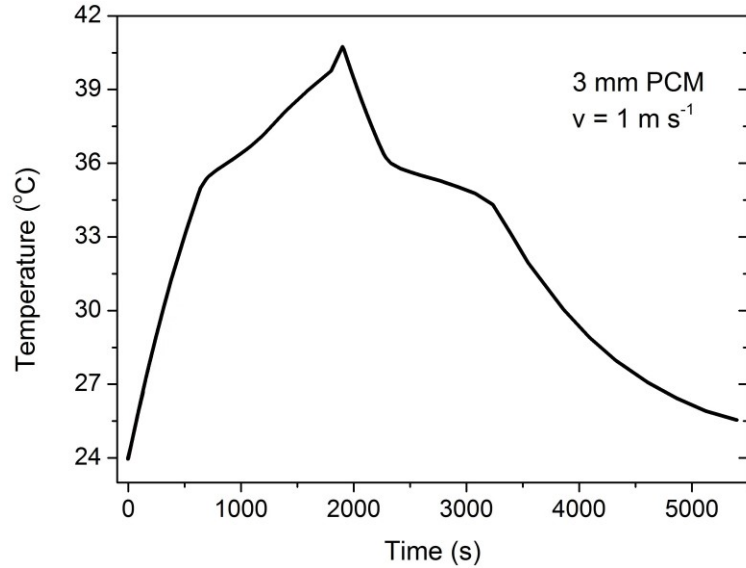


Figure 4.10. Temperature profiles of the battery pack cooled by the hybrid cooling system during a 1.92 C discharge.

4.4.5 Space Utilization in Battery Modules

The space utilization ratio (ξ) is crucial when developing compact systems, and it can directly affect the energy density of the entire battery system. In Table 4.1, the battery performance indices including the ξ values of the selected battery packs studied in this Chapter are listed. The product of ξ and the capacity ratio (θ) indicates the overall space utilization ratio while taking into account the effect of the space occupied by the PCM. In the literature regarding cylindrical battery pack thermal management systems, the space utilization ratios are between 49.82% and 57.96% in the work of Wang *et al.* [9], 54.43% in the work of He and Ma [141], 48.80% in the work of Yang *et al.* [8], 53.17% in the work of Mills *et al.* [18]. It could be summarized that PCM core cooling is a space-saving design and it can fundamentally improve the thermal performance of cylindrical batteries and make batteries ready for compact layouts and hybrid cooling designs.

Table 4.1. Summary of the battery performance data of selected battery packs.

	T_{\max}	ΔT	θ	ξ	$\theta * \xi$
Original battery pack, NC*	62.0	4.47	100%	86.0%	86.0%
Battery pack (3.8 mm cores), NC	46.6	3.24	83.4%	86.0%	71.7%
Battery pack (3.4 mm & 4.2 mm cores), NC	46.0	1.98	83.6%	86.0%	71.9%
Original battery pack, forced air cooling	47.4	10.8	100%	74.1%	74.1%
Hybrid cooling (3.2 mm cores)	39.4	4.70	88.8%	74.1%	65.8%

* NC: Natural convection cooling applied at the battery pack surface, $h = 10 \text{ W m}^{-2} \text{ K}^{-1}$.

4.5. Summary

In this Chapter, the PCM-based internal BTM system is numerically studied and optimized on a battery submodule containing 40 cylindrical batteries, in which the battery parameters and heat generation rates are obtained from a commercial 18650-type Li-ion battery. Solid and conjugate heat transfer models are applied to simulate the cooling performance of the proposed battery thermal management system. Variables including PCM core size and PCM core size distribution are taken into the simulations to optimize the BTM system. A hybrid cooling design is also studied by integrating a forced air cooling system with the PCM-embedded battery module. The concluding remarks are given as follows:

- 1) As the PCM core radius increases to 3.8 mm, the peak temperature of the battery module can be managed below 50°C under an unfavorable convective cooling condition ($h = 1 \text{ W m}^{-2} \text{ K}^{-1}$).
- 2) By adjusting the PCM core size distribution inside the battery pack, the maximum temperature difference between jelly rolls can be maintained within 2°C under natural convection. Also, the latent heat of the PCM cores can be fully utilized, which proves the feasibility of using pure PCM in the design.
- 3) Without altering the battery appearance, the core cooling design facilitates the integration of a forced air cooling system within the battery pack. The hybrid cooling

design with a 1 m s^{-1} inlet air velocity and 3.2 mm PCM cores can effectively manage the battery temperature below 40°C and the temperature difference within 5°C .

As a final note, while providing an internal cooling option, the PCM-embedded batteries in the battery pack can be arranged in a more compact layout than previous works, which can notably enhance the energy density of the entire battery system.

Chapter 5. Development of a Heat Pipe-Based BTM System for Normally Discharged Prismatic Li-ion Batteries

5.1 Overview

Due to their higher power density, prismatic Li-ion batteries are generally equipped on hybrid electric vehicles and electric racing vehicles and frequently charged and discharged at high rates. In this Chapter, an ultrathin heat pipe and wet cooling combined active BTM system is developed to handle the thermal surge of prismatic Li-ion batteries during high-rate discharges. The BTM system utilizes the high thermal conductivity of ultrathin heat pipes to transfer the heat from the battery side to the condenser side, where wet cooling is carried out to dissipate the heat. The heat pipe-wet cooling combined design is for the first time applied to battery cooling. Two battery packs, 3 Ah and 8 Ah, with different condenser lengths are used and tested through a series of high-intensity discharges to examine the cooling effects of the proposed BTM system. Different cooling strategies are also implemented on the condenser side of the heat pipes to investigate their effect, and comparisons were also made between them and the natural convection. The experimental results show that the novel heat pipe-wet cooling combined BTM system has significantly improved cooling ability than other heat pipe-based BTM system. The proposed BTM system can be further equipped on electric racing cars for competitions. The water consumed due to evaporation could be refilled during pit stops.

5.2 Experimental Setup

Two battery packs, four series-connected 3 Ah batteries and four series-connected 8 Ah batteries, were used in the experiments. The specifications of the batteries in the two battery packs are listed in Table 5.1. Depending on whether heat pipes are involved in the BTM system, the BTM systems used in the tests are classified as two main groups: pack without heat pipes (natural convection) and pack with heat pipes. For natural convection condition, all the battery packs were tested as received, where the batteries were closely attached to each other. While in the heat pipe-based BTM system, heat pipes were

sandwiched between the batteries, and the condensers were exposed externally to the packs. Heat pipes of different dimensions were selected to match the sizes of the battery packs. Thermally conductive silicone pads were also placed between the batteries and heat pipes to increase their thermal contact. The specifications of the heat pipes and thermal pads are given in Table 5.2. The selection of battery packs and heat pipes was also due to their availability. The heat pipes were chosen to have close widths as the batteries. After assembly, the condenser lengths (the lengths of the exposed heat pipe sections) were 125 mm and 70 mm in the 3 Ah and 8 Ah battery packs, respectively.

Ultrathin heat pipes have been widely used for electronic cooling due to their compactness [142]. Fig. 5.1 shows the heat pipe 2 used in the work. The ultrathin heat pipe is made of aluminum and consists of arrays of hollow channels filled with acetone staying at vapor and liquid coexisting phases. Once heated by the batteries, the acetone boils at the evaporator side and flows to the condenser side for condensation. The movement of the acetone can quickly transfer the thermal energy between the evaporator and condenser of the heat pipes and can alleviate the temperature increase of the sandwiched batteries.

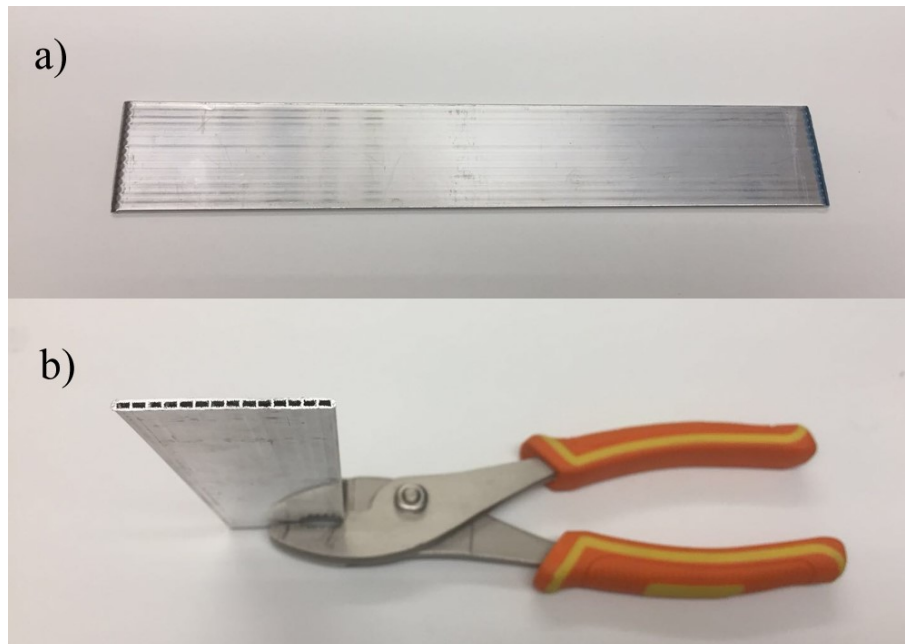


Figure 5.1. Photographs of the a) heat pipe 2 and b) its internal structure.

Table 5.1. Specifications of the 3 Ah and 8 Ah batteries.

	Battery 1	Battery 2
Length (mm)	125	180
Width (mm)	40	45
Height (mm)	5.5	9
Weight (g)	70	185
Nominal voltage (V)	3.7	3.7
Nominal capacity (mAh)	3000	8000
Maximum charge rate (C)	5	5
Maximum discharge rate (C)	25	25
Working temperature range (°C)	-20 – 60	-20 – 60

Table 5.2. Specifications of heat pipes and thermal pads.

	Heat pipe 1	Heat pipe 2	Thermal pad 1 (2)
Length (mm)	250	250	125 (175)
Width (mm)	40	50	40 (45)
Thickness (mm)	2	2.5	0.5
Weight (g)	25	40	4 (6.5)
Material	Aluminum	Aluminum	Silicone compound
Wick structure	Groove	Groove	-
Working fluid	Acetone	Acetone	-
Working temperature (°C)	-50 – 125	-50 – 125	-40 – 200
Thermal conductivity ($\text{W m}^{-1} \text{K}^{-1}$)	-	-	3.2

The schematic illustration of the heat pipe sandwiched 8 Ah battery pack is shown in Fig. 5.2a. This schematic is similar to the 3 Ah battery pack except for their difference in battery dimensions. Fig. 5.2b shows the locations where K-type thermocouples were used to record the battery temperatures. Through comparing the recorded temperatures from T_1 to T_6 , the temperature difference in the battery pack level can be obtained. Similarly, the battery level temperature uniformity can be found by comparing the temperatures from T_a to T_e .

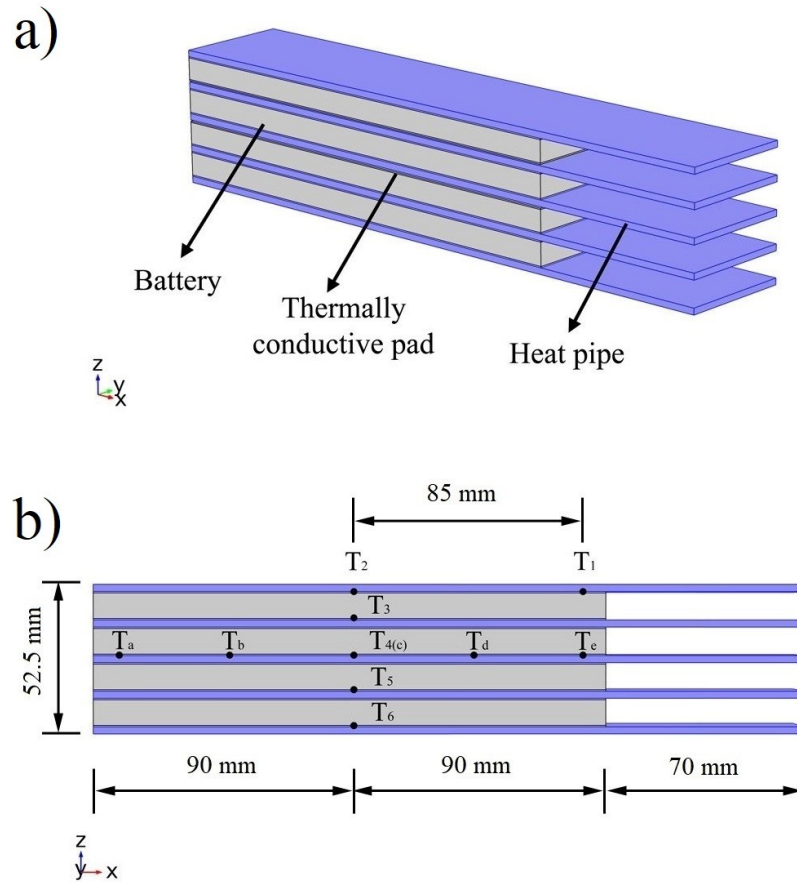


Figure 5.2. a) Schematic illustration of a battery pack sandwiched by heat pipes; b) Locations where the battery temperatures were measured.

For the heat pipe-based BTM system, five cooling strategies were applied on the condenser: 1) condenser cooled by ambient air (named as ‘heat pipes in ambient’ in figure legends), 2) condenser cooled by a horizontal fan (hori-pipe with fan), 3) condenser cooled by a vertical fan (verti-pipe with fan), 4) condenser cooled by thermostat water bath (heat pipe in water bath), and 5) condenser cooled through wet cooling (hori-pipe with wet cooling). The schematic illustrations of methods 2) – 4) are shown in Fig. 5.3. In the systems involving a cooling fan, the distance between the fan and the heat pipes was kept at 5 cm, and the radius and rotation speed of the fan were 4 cm and 1500 rpm, respectively. The temperature of the water in the thermostat bath was 25°C. For wet cooling strategy, the water volume per spray was 0.7 ml, and the frequencies of spray was 1 min⁻¹ and 0.5 min⁻¹ for the 3 Ah and 8 Ah battery packs, respectively. These two spray frequencies were selected because the water evaporation rates on the condensers matched well with the water

supply rates, i.e., the condensers were kept moist and there was no water dripping from the condensers during the cooling stage. To improve the adhesion of water to the condensers, thin layers of water absorbent fibers were wrapped around the condenser.

The relative humidity is related to the evaporation rate of water and the energy that can be taken away from the condensers of heat pipes. With a higher relative humidity, the evaporation rate will be reduced, and the cooling performance of the heat pipe-wet cooling combined BTM will be degraded. For all the tests were done, the relative humidity was within the range between 30% and 35%.

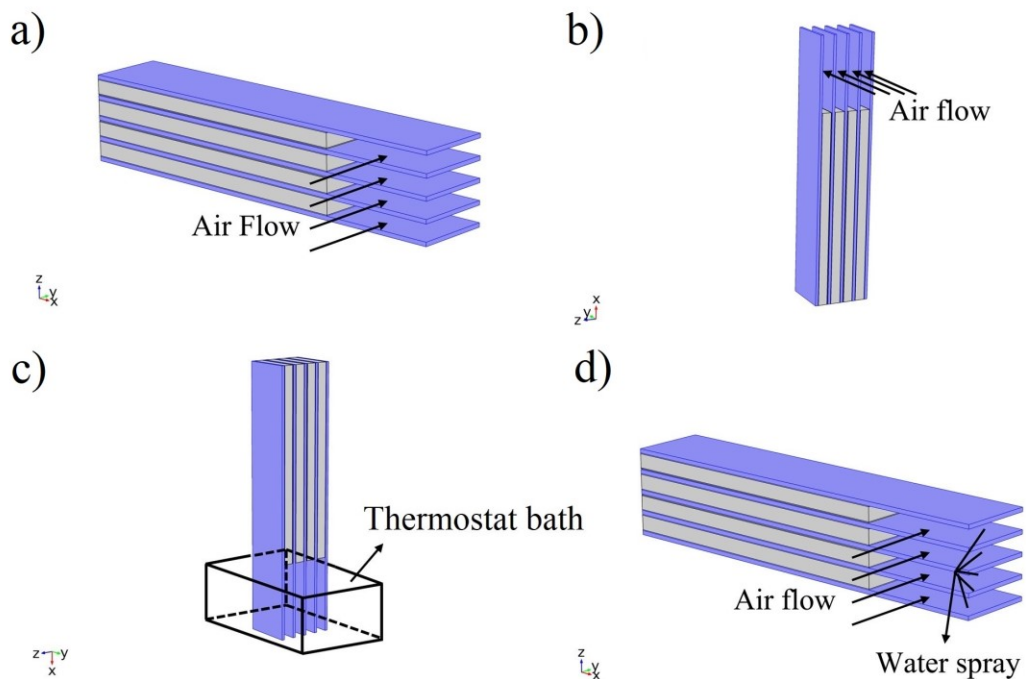


Figure 5.3. Schematic illustrations of four heat pipe-based BTM systems, a) horizontal heat pipes with cooling fan; b) vertical heat pipes with cooling fan; c) heat pipes in a thermostat water bath and d) horizontal heat pipes with wet cooling.

To ensure the comparability of the cooling results and to avoid the difference between battery packs, one battery pack for each capacity was used for all the tests with equipping different BTM systems. The capacity fading of the battery packs during the tests can be neglected since all the Li-ion batteries were labeled with a cycle life of 1000 retaining 80% of their total capacities. To reduce the uncertainties, such as air flow, all the tests were taken in a 0 m s^{-1} closed wind tunnel. Other uncertainties, such as accuracy of the

thermocouples and the discharge currents, were attributed to the accuracy of the apparatuses. Tests were repeated three times for every testing configuration, i.e., a battery pack equipped with one BTM system discharged at a certain rate, and it was found that the temperature curves were overlapped for each testing configuration. Therefore, the temperature curve obtained from the first test was recorded for presentation.

Both the 3 Ah and 8 Ah battery packs were charged and discharged using a battery analyzer, model PCBA 5010-4, from the Energy Storage Instruments. Prior to tests, both battery packs were conditioned at room temperature (298 K) by cycling 5 times at 1 C rate using an ESI battery analyzer (PCBA 5010-4) with a cut-off voltage of 3 V and 4.2 V during discharges and charges, respectively, which allows the formation of solid electrolyte interface (SEI) and eliminates the impact of irreversible capacity fade of new Li-ion batteries [143]. The constant charging and discharging currents during the conditioning stage were set to 1.3 A with a cut-off current rate of 1/50 C at the potentiostatic charge stage. During the tests, the 3 Ah battery pack was discharged at rates of 1 C, 2 C, and 3 C, while the 8 Ah battery pack was discharged at a current of 10 A, which is the maximum discharge current of the battery analyzer. Prior to all discharges, the BTM systems were turned on to stabilize the temperature of the battery packs.

5.3 Results and Discussion

5.3.1 Temperature Control

In Fig. 5.4, the maximum temperature curves of the 3 Ah battery pack cooled by different BTM systems are compared in 3 C-rate discharges. It is seen that the battery pack has the highest temperature when discharged in ambient air, which is attributed to the small cooling area and the accumulated heat in the battery pack center. With the assembly of heat pipes, the cooling performance is significantly improved. Though discharged in ambient, the maximum temperature dropped to 41°C. The use of the thermostat bath did not greatly further improve the cooling effect, and the main reason is that the dissolved air bubbles came out of the water because of the temperature increase and gathered at the surfaces of the condenser, which hindered the heat transfer between the heat pipes and the water.

A comparison is then made between the fan cooling on the battery pack equipped with heat pipes of different inclination angles. Although previous researchers observed that heat pipes had different performance at different inclination angles, the micro-channeled heat pipes perform similarly in different inclination angles. In the ultra-thin heat pipe, the gas and liquid inside the microchannel are discontinuously connected. When there exists a temperature difference between the evaporator and condenser of the heat pipes, the coolant can circulate inside the channel to dissipate the heat generated by the battery pack. The capillary force also minimizes the effect of the gravity on the coolant.

For the wet cooling approach, the battery pack had the lowest initial temperature due to the evaporation of water reduced the temperature of the battery pack. In comparison, it is seen that the heat pipe and wet cooling combined BTM system is the most effective method in managing the temperature rise of batteries among all the methods, with the maximum temperature of 21°C at the end of the 3C discharge.

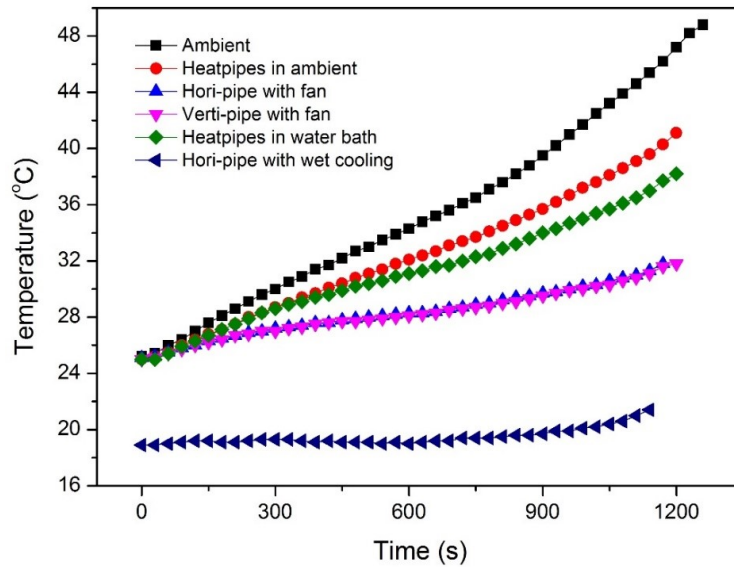


Figure 5.4. Temperature curves of the 3 Ah battery pack cooled by different approaches during the 3 C discharges.

Besides the 3 C rate discharge, 1 C and 2 C discharges were also carried out. Due to the overlap of the temperature profiles of the BTM system with different pipe inclination angles, as well as the unsatisfactory cooling performance of the thermostat water bath, 1 C and 2 C discharges were only performed on the 3 Ah battery packs equipped with the other

four cooling approaches: ambient, heat pipes in ambient, horizontal pipes with fan cooling, and horizontal pipe with wet cooling. The temperature rises of the four cooling approaches are summarized in the bar chart as shown in Fig. 5.5. The fan cooling and wet cooling outperform the other cooling approaches. Particularly, the wet cooling approach achieves the lowest temperature rises for all discharge rates, which demonstrates its superiority over other cooling approaches in managing the heat generated from Li-ion batteries.

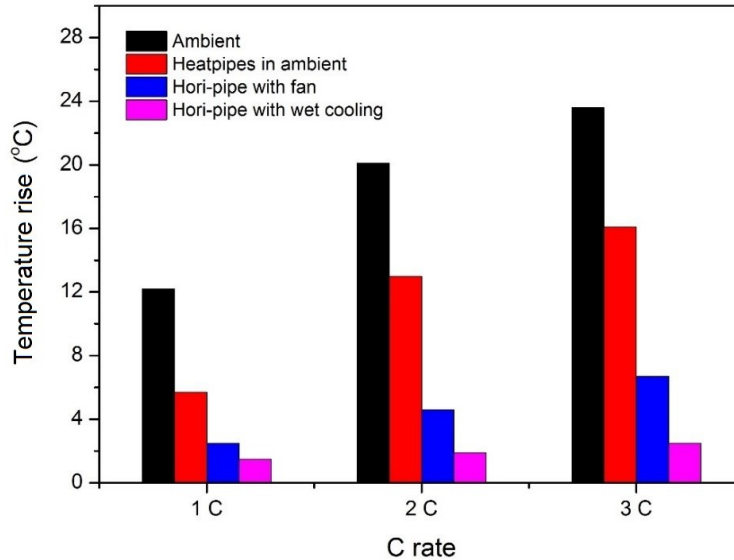


Figure 5.5. Temperature rises of the 3 Ah battery pack cooled through different approaches at the assigned discharge rates.

5.3.2 Temperature Difference

Temperature uniformity in a Li-ion battery system is an important factor that can affect its long-term performance. A nonuniform temperature in the battery level and the pack level can lead to different capacity fading rates and unbalanced voltages between batteries.

Fig. 5.6 shows the temperature difference profiles of the 3 Ah battery pack cooled through different approaches during the 3 C discharge. As can be seen, the temperature difference of the battery pack discharged in ambient experiences a dramatic rise as discharge proceeds, and at the end of discharge, the temperature difference reaches 6.8°C.

The big temperature difference is attributed to the heat accumulation in the battery pack center. In comparison, the maximum temperature differences are all within 3°C in the heat pipes-sandwiched battery packs, and the maximum temperature difference is even lower than 1.5°C when the wet cooling approach is applied on the condenser side of the heat pipes. Compared with natural convection, the improved temperature uniformity in the heat pipe-equipped battery pack is due to the fact that the heat pipes can efficiently transfer the heat from the center of the battery pack to the condenser for dissipation, thus alleviating the heat accumulation.

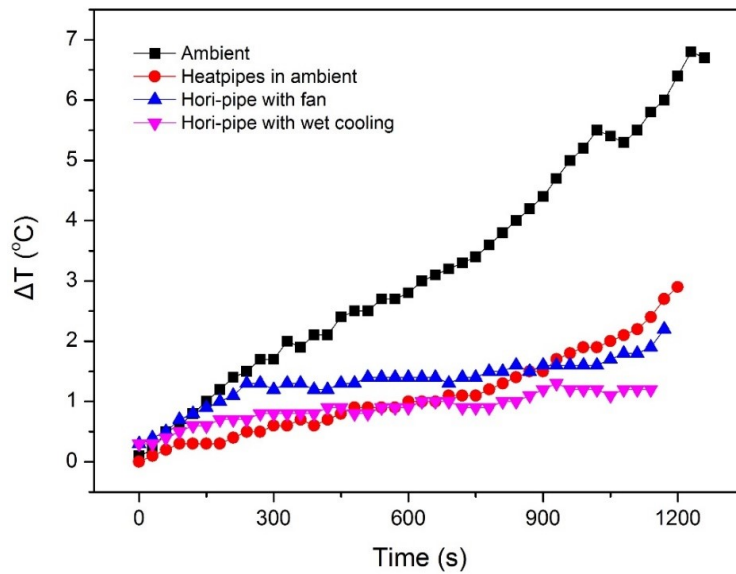


Figure 5.6. Temperature difference curves of the 3 Ah battery pack cooled through different approaches during the 3 C discharges.

The temperature difference curves of the inner battery cooled through different approaches are plotted in Fig. 5.7. As shown, the trends of the battery-level temperature difference curves are similar to that of the pack-level, but the temperature differences are much smaller and are below 2.5°C, which is because the inner battery has a simpler and a more uniform surrounding for heat transfer than the battery pack. In Table 5.3, the experimental results of the 3 Ah battery are summarized. In the table, T_{\max} and T_{rise} indicate the maximum temperature and the maximum temperature rise of the battery pack during discharges, respectively. ΔT_{pack} and ΔT_{cell} mean the maximum temperature differences in the battery pack and battery cell during discharges, respectively.

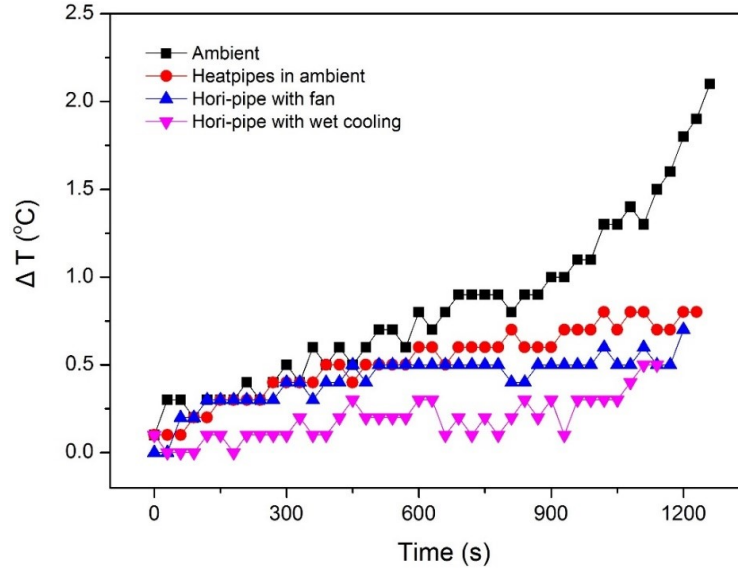


Figure 5.7. Temperature difference curves of the inner battery in the 3 Ah battery pack cooled through different approaches during the 3 C discharges.

Table 5.3. Summary of the experimental results of the 3 Ah battery pack.

Cooling methods	C rate	T_{max} (°C)	T_{rise} (°C)	ΔT_{pack} (°C)	ΔT_{cell} (°C)
Ambient	1 C	37.2	12.2	–	–
	2 C	45	20.1	–	–
	3 C	48.8	23.6	6.8	2.1
Heat pipes in ambient	1 C	30.7	5.7	–	–
	2 C	38	13	–	–
	3 C	41.1	16.1	2.9	0.8
Horizontal pipes with fan	1 C	27.5	2.5	–	–
	2 C	29.6	4.6	–	–
	3 C	31.8	6.7	2.2	0.7
Vertical pipes with fan	3 C	31.8	6.8	2.2	0.7
Heat pipes in water bath	3 C	38.2	13.2	6.2	1.5
Horizontal pipe with wet cooling	1 C	20.5	1.5	–	–
	2 C	21	1.9	–	–
	3 C	21.5	2.5	1.2	0.5

5.3.3 Large Battery Pack Cooling

A compact battery pack is necessary for some mission-critical applications, and the space occupied by the BTM system should be reduced. To examine the heat pipe and wet cooling combined BTM system in cooling a large-size battery pack with a reduced cooling area, an 8 Ah battery pack is used, and the length of the heat pipe condenser is shortened from 12 cm in the 3 Ah battery pack to 6.5 cm. Meanwhile, the spraying frequency is decreased from 1 spray per minute to 0.5 sprays per minute.

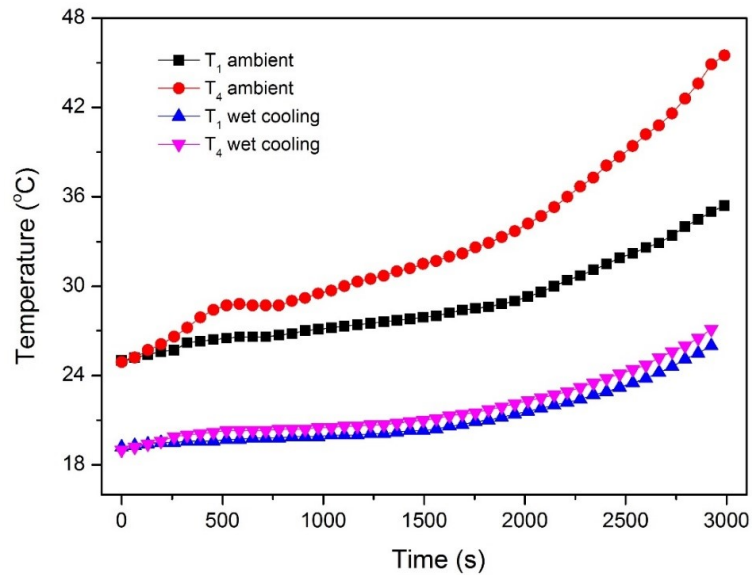


Figure 5.8. The maximum and minimum temperature curves of the 8 Ah battery pack cooled through natural convection and wet cooling approach during 10 A discharges.

In Fig. 5.8, the maximum and minimum temperature curves of the 8 Ah battery pack cooled through natural convection and wet cooling are given. The heat pipe and wet cooling combined BTM system outperforms the natural convection in control of the battery pack temperature. Although the cooling performance of the combined system is slightly degraded compared to that equipped on the 3 Ah battery pack, the battery temperature is much lower than that of the upper limit of the optimum temperature range, and there is a lot of room to make the BTM system more compact. The pack-level and battery-level temperature difference curves of the 8 Ah battery pack cooled through natural convection and wet cooling are given in in Fig. 5.9a and b, respectively. When natural convection was applied, the pack-level and battery-level temperature differences reach as high as 9.3°C and

3.5°C at the end of the 10 A discharge, respectively. While for the heat pipe and wet cooling combined system, the pack-level and battery-level temperature differences of the battery pack are managed to 1.1°C and 0.4°C, respectively, which ensures a uniform capacity fading rate for all batteries and guarantees a high energy output and long lifespan.

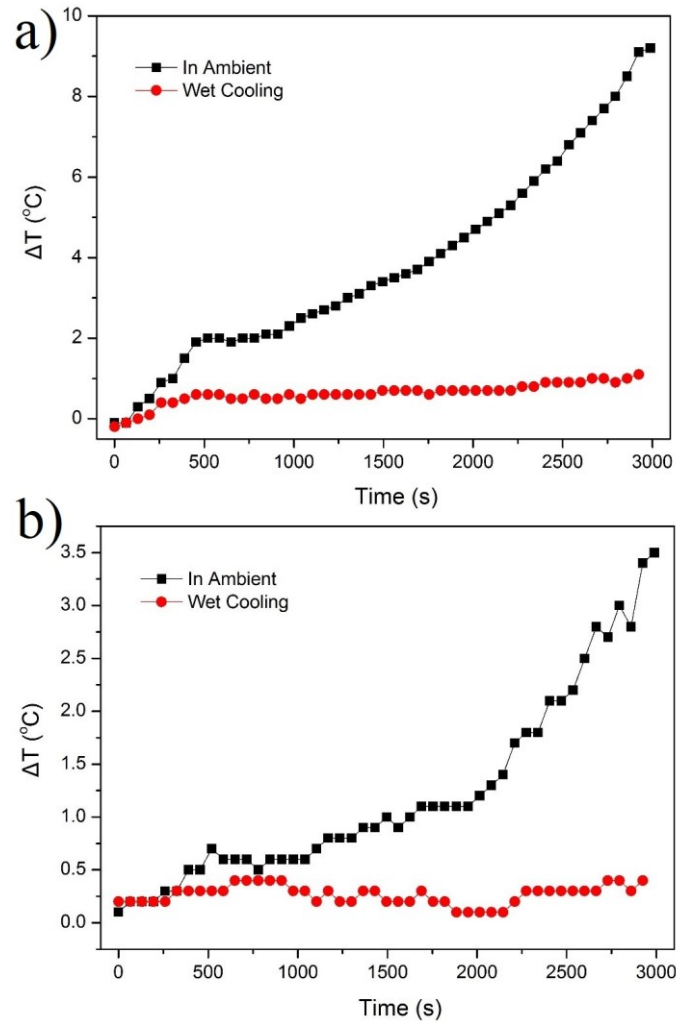


Figure 5.9. a) Pack-level and b) battery-level temperature difference curves of the 8 Ah battery pack cooled through natural convection and wet cooling approach during 10 A discharges.

Cycle tests were then carried out on the 8 Ah battery pack cooled through natural convection and wet cooling approach. During the tests, the charging and the discharging currents were set to 10 A, and the cut-off current at the potentiostatic charging stage was set to 160 mA. In Fig. 5.10, the temperatures at points 1 and 4 are plotted for both systems,

and the temperature difference curves are given on the bottom of each figure. As shown, when the battery pack is discharged in ambient, the maximum temperature reaches 51.5°C at the end of the 2nd and 3rd cycles, having a maximum temperature difference of 12.4°C. It also takes 3 cycles for the battery pack to operate under stable conditions (same initial temperature prior to discharging). In comparison, the battery pack equipped with the heat pipe and wet cooling combined BTM system returned to its initial temperature after the first cycle, and the maximum temperature during the test was as low as 26°C. Meanwhile, the pack-level temperature difference was the same for both cycles with a maximum value of 1°C.

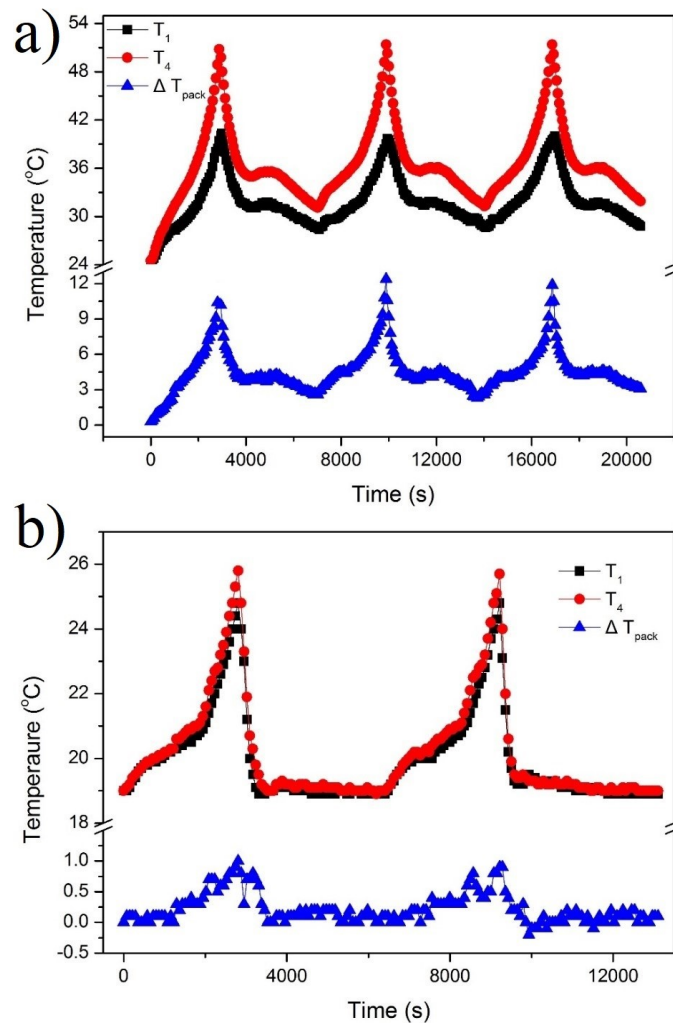


Figure 5.10. Temperature curves of the 8Ah battery cooled through a) natural convection and b) wet cooling approaches during cycle tests.

5.4 Summary

In this Chapter, a heat pipe-based BTM system was experimentally studied on prismatic Li-ion batteries. Different cooling strategies were implemented on the condenser side of the heat pipes to investigate their effect, and comparisons were also made between them and natural convection.

For tests on the 3 Ah battery pack, natural convection is insufficient to cool down the battery pack discharged at high rates, and it also leads to a large temperature gradient inside the battery pack. After embedding the heat pipes, an improved temperature uniformity and a relatively alleviated temperature rise was found in the battery pack discharged in ambient. The use of a cooling fan further improved the cooling capability of the heat pipe-based BTM system. By evaporating water on the heat pipe condenser, wet cooling managed the battery heat more effectively than all the other implemented cooling strategies. It could maintain the battery temperature and temperature difference at much lower levels. Even with a reduced condenser length and water spraying frequency, the heat pipe and wet cooling combined BTM system performed outstandingly in managing the temperature of an 8 Ah battery pack.

Chapter 6. Development of a Numerical Model for Simulating Abnormally Discharged Batteries

6.1 Overview

Safety is the priority in lithium-ion (Li-ion) battery applications. A large portion of electrical and thermal hazards caused by Li-ion batteries are associated with short circuits. During short circuits, Li-ion batteries discharge the stored energy at extremely high rates, which could cause heat surge in batteries and even lead to thermal runaway. In this Chapter, both external and internal short circuit tests are conducted on Li-ion batteries and battery packs of different capacities. The results indicate that external short circuits are dangerous for smaller size batteries due to their higher internal resistance, and this type of short can be well managed by assembling fuses. In internal short circuit tests, higher chance of failure is found on larger capacity batteries. A modified electrochemical-thermal model is proposed, which incorporates an additional heat source at the nail location and proves to be successful in depicting temperature changes of non-thermal runaway batteries and estimating the occurrence and the approximate start time of thermal runaway of unsafe batteries.

6.2 Experimental Setup

The LiCoO₂ batteries used in experiments are listed in Table 6.1. Among them, batteries No. 3 and 4 have the same capacity but are different in electrode thicknesses and maximum discharge C-rates. All the batteries are new without additional safety designs to prevent short circuits. They are preconditioned under a constant current of 0.1 C between 3.0 V and 4.2 V for 5 cycles while finishing at a charged state prior to tests.

External short circuit tests are performed by clamping positive and negative tabs with a 20 mΩ wire, while internal short circuit tests (or nail penetration tests) are implemented with the use of stainless steel nails with a diameter of 2.5 mm. In external short tests, two thermocouples are utilized to measure temperature changes: one is attached at the center of the battery and the other one sticks on the corner (5 mm from the edge). During nail

tests, one more thermocouple is attached to the nail (5 mm from the battery surface), and the thermocouple located at the battery center is 5 mm apart from the nail site. Besides temperatures, the voltages of batteries and battery packs are also recorded in all tests.

Table 6.1. Specifications of batteries used in short circuit tests.

Battery type No.	1	2	3	4
Thickness [mm]	3.8	4.5	8.2	8.5
Width [mm]	30	28	45	45
Length [mm]	52	82	133	133
Initial voltage [V]	4.19	4.19	4.19	4.19
Nominal capacity [mAh]	650	1200	5000	5000
Maximum discharge rate [C]	5	25	25	65

6.3 Model Description

An electrochemical-thermal coupling model is modified and employed in this study [144]. In the coupling model, the heat generated from the electrochemical part is applied to the transient thermal part as a portion of the battery heat source, while the temperature obtained by the transient thermal model is, in turn, input to the electrochemical model. The schematic illustration for the pseudo-2D electrochemical model of a Li-ion cell is given in Fig. 6.1b. The electrode region consists of a mixture of active insertion material particles, electrolyte, binder, and conductive filler, while the separator consists of polymer and electrolyte. Li_xCoO_2 and Li_yC_6 are used as the positive and negative active materials in this study, respectively. LiPF_6 salt in a non-aqueous liquid mixture of 1:2 v/v ethylene and dimethyl carbonate is employed as the binary electrolyte, which permeates in both the separator and the electrodes. Since the total number of current collectors in the battery is half of the number of electrodes and separators, and electrochemical reactions take place on both sides of a current collector, the thicknesses of the current collectors of the cell used in the thermal analysis are half that of the actual current collectors.

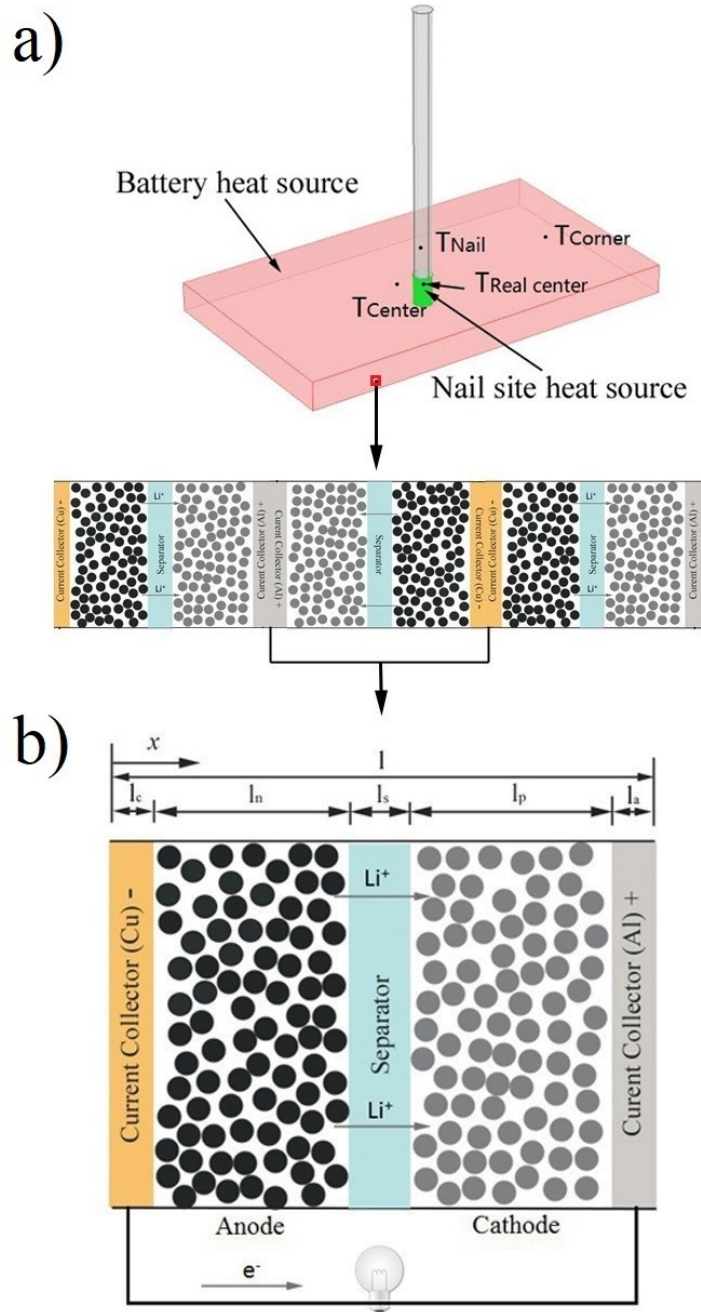


Figure 6.1. Schematics of the nail penetration model: a) A thermal model that includes heat sources from both the battery and the nail location; b) A pseudo-2D electrochemical model.

6.3.1 Electrochemical Model

The electrochemical model used in this work is from [144]. In the binary electrolyte phase, the material balance is given by Fick's second law coupled with a source term:

$$\varepsilon_e \frac{\partial c_e}{\partial t} = \frac{\partial}{\partial x} \left(D \frac{\partial c_e}{\partial x} \right) + \frac{(1 - t_+^0)}{F} j^{Li} \quad (6.1)$$

Since no mass flux of lithium ions exists at the boundary of the electrode/current collector, the boundary condition for these sites yields:

$$-D \frac{\partial c_e}{\partial x} \Big|_{x=0} = -D \frac{\partial c_e}{\partial x} \Big|_{x=l_n+l_s+l_p} = 0 \quad (6.2)$$

At the interfaces between anode and separator, as well as separator and cathode, the concentration of the electrolyte is continuous, that is:

$$c_e \Big|_{x=l_n^-} = c_e \Big|_{x=l_n^+} \quad (6.3)$$

$$c_e \Big|_{x=(l_n+l_s)^-} = c_e \Big|_{x=(l_n+l_s)^+} \quad (6.4)$$

The charge balance in the electrolyte phase based on Ohm's law is given by:

$$-\left(k^{\text{eff}} \frac{\partial \Phi_e}{\partial x} \right) + \frac{2RT(1 - t_+^0)}{F} \left(k^{\text{eff}} \frac{\partial (\ln c_e)}{\partial x} \right) = i_e \quad (6.5)$$

where the effective ionic conductivity k^{eff} , calculated by $k^{\text{eff}} = k\varepsilon_e^{1.5}$, is the Bruggeman correction for the tortuosity effect. The value of k is given by [144]:

$$k = 15.8c_e \exp(-13472c_e^{1.4}) \quad (6.6)$$

A zero gradient boundary condition restricts the solution of (6.5) at the two electrode/current collector interfaces:

$$k^{\text{eff}} \frac{\partial \Phi_e}{\partial x} \Big|_{x=0} = k^{\text{eff}} \frac{\partial \Phi_e}{\partial x} \Big|_{x=l_n+l_s+l_p} = 0 \quad (6.7)$$

In the solid phase of electrodes, the material and charge balances are given by:

$$\frac{\partial c_s}{\partial t} = \frac{D_s}{r^2} \frac{\partial}{\partial r} \left(r^2 \frac{\partial c_s}{\partial r} \right) \quad (6.8)$$

and

$$-\sigma^{\text{eff}} \frac{\partial \Phi_s}{\partial x} = i_s \quad (6.9)$$

where the effective conductivity is determined by $\sigma^{\text{eff}} = \varepsilon_s \sigma$, where s refers to the positive

and negative electrodes. The boundary conditions for the solid electrode particle are:

$$\frac{\partial c_s}{\partial r} \Big|_{r=0} = 0 \quad (6.10)$$

$$-D_s \frac{\partial c_s}{\partial r} \Big|_{r=R_s} = \frac{j^{Li}}{a_s F} \quad (6.11)$$

where a_s denotes the solid electrode surface area per unit volume, which is calculated by:

$$a_s = \left(\frac{3}{R_s}\right) (1 - \varepsilon_e - \varepsilon_p - \varepsilon_f) \quad (6.12)$$

At the interface of current collector/electrode, the charge flux is the same as the current density applied on the electrode:

$$-\sigma^{\text{eff},n} \frac{\partial \Phi_{s,n}}{\partial x} \Big|_{x=0} = \sigma^{\text{eff},p} \frac{\partial \Phi_{s,p}}{\partial x} \Big|_{x=l_n+l_s+l_p} = \frac{I_{app}}{A} \quad (6.13)$$

While for the interfaces between the separator and electrodes, no charge flux exists:

$$\sigma^{\text{eff},n} \frac{\partial \Phi_{s,n}}{\partial x} \Big|_{x=l_n} = \sigma^{\text{eff},p} \frac{\partial \Phi_{s,p}}{\partial x} \Big|_{x=l_n+l_s} = 0 \quad (6.14)$$

The reaction current density j^{Li} in the above equations is determined by the Butler-Volmer equation:

$$j^{Li} = a_s i_0 \left[\exp\left(\frac{0.5F}{RT} \eta\right) - \exp\left(-\frac{0.5F}{RT} \eta\right) \right] \quad (6.15)$$

The over-potential of the intercalation reaction, η , is defined as:

$$\eta = \Phi_s - \Phi_e - U \quad (6.16)$$

where U is the open circuit potential, which is given below for anode and cathode, respectively:

$$\begin{aligned} U_{\text{ref},-} = & 8.0023 + 5.0647x - 12.578x^{0.5} - 8.6322 \times 10^{-4}x^{-1} \\ & + 2.1765 \times 10^{-5}x^{1.5} - 0.4602 \exp[15(0.06 - x)] \\ & - 0.5536 \exp[(-2.4326(x - 0.92))] \end{aligned} \quad (6.17)$$

$$\begin{aligned} U_{\text{ref},+} = & 85.681y^6 - 357.7y^5 + 613.89y^4 - 555.65y^3 + 281.06y^2 \\ & - 76.648y - 0.30987 \exp(5.657y^{115}) + 13.1983 \end{aligned} \quad (6.18)$$

The positive electrode reference potential given above is for batteries 1 and 2, while for batteries 3 and 4, the cathode reference potential is adopted from Ref. [145]. All the parameters used in the electrochemical model are given in Table 6.2. An Arrhenius equation defines the temperature dependence of the properties, including exchange current density, solid and electrolyte phase diffusion coefficients, and electrolyte phase conductivity. A general form can be expressed as:

$$\Psi = \Psi_{\text{ref}} \exp\left[\frac{E_{\text{act}}^{\Psi}}{R} \left(\frac{1}{T_{\text{ref}}} - \frac{1}{T}\right)\right] \quad (6.19)$$

where Ψ_{ref} is a general property value at a reference temperature of 25°C. The property values at other temperatures are controlled by the activation energy E_{act}^{Ψ} , which have values of 3×10^4 , 4×10^3 , 2×10^4 , 1×10^4 , 2×10^4 J mol⁻¹ for the exchange current density, negative solid phase diffusion coefficient, positive solid phase diffusion coefficient, electrolyte phase diffusion coefficient, and electrolyte phase conductivity, respectively.

Table 6.2. Electrochemical and thermal parameters of the batteries used in the simulation.

Parameter	Cu foil	Negative electrode	Separator	Positive electrode	Al foil
$l_{\text{battery } 1}$ (μm)	15	71	18	49	17
$l_{\text{battery } 2}$ (μm)	14	50	18	40	16
$l_{\text{battery } 3}$ (μm)	12	38	18	27	16
$l_{\text{battery } 4}$ (μm)	10	27	18	20	14
R_s (μm)	-	1	-	1	-
D_s (m ² s ⁻¹)	-	3.9×10^{-14}	-	1×10^{-13}	-
ε_e	-	0.332	0.5	0.3	-
ε_s	-	0.58	-	0.6	-
$c_{s,\text{max}}$ (mol m ⁻³)	-	31858	-	49943	-
$c_{s,0}^{\text{battery } 1, 2}$ (mol m ⁻³)	-	22300	-	15982	-
$c_{s,0}^{\text{battery } 3, 4}$ (mol m ⁻³)	-	25486	-	20976	-
c_e (mol m ⁻³)	-	2000	2000	2000	-
σ (S cm ⁻¹)	-	1	-	0.06	-
t_+^0	-	0.363	0.363	0.363	-
k (W m ⁻¹ K ⁻¹)	398	5	0.334	5	238
ρ (kg m ⁻³)	8930	2500	1009	1500	2702
C_p (J kg ⁻¹ K ⁻¹)	385	700	1978	700	903

6.3.2 Thermal Model

The thermal model is governed by the energy conservation equation given in Chapter 2. In the equation, the density and specific heat capacity of Li-ion battery cell are calculated by averaging the values of each component inside the cell on a volume basis, while the thermal conductivity in series and parallel directions are calculated differently through equations (6.20) and (6.21), respectively. The parameters used in the coupling model are listed in Table 6.2.

$$k_s = \frac{\sum_i l_i}{\sum_i \frac{l_i}{k_i}} \quad (6.20)$$

$$k_p = \sum_i \frac{l_i}{l} k_i \quad (6.21)$$

The first term on the right-hand side of the energy conservation equation (2.1) describes the heat dissipation, which consists of two main sources in this study: convective heat and radiative heat, which can be expressed as follows in the x -direction:

$$-k \frac{\partial T}{\partial x} = h(T - T_{amb}) + \varepsilon \sigma (T^4 - T_{amb}^4) \quad (6.22)$$

The values of the convective coefficient h , surface emissivity ε , and ambient temperature T_{amb} are set at $7.9 \text{ W m}^{-2} \text{ K}^{-1}$, 0.9 , and 298.15 K , respectively. Similar equations can also be built in the y and z directions.

Compared to an external short circuit model and a conventional discharge model, the nail penetration model has one more source of heat generation contributing to the term “ q ”: the heat generated from the nail region due to localized resistance. Fig. 6.1a illustrates the nail penetration of a 0.65 Ah battery. Four probes represented as black dots in the figure are used to record temperature variations during simulation. Two origins of heat sources are indicated: battery heat source (red part) due to high rate discharge and nail location heat source (green part) due to joule heating, as detailed below:

- 1) Battery heat source:

$$q_r l = \int_0^{l_n+l_s+l_p} j^{Li} (\Phi_s - \Phi_e - U) dx \quad (6.23)$$

$$q_j l = \int_0^{l_n+l_s+l_p} \left[\sigma^{\text{eff}} \left(\frac{\partial \Phi_s}{\partial x} \right)^2 + k^{\text{eff}} \left(\frac{\partial \Phi_e}{\partial x} \right)^2 + \frac{2k^{\text{eff}} RT}{F} (1 - t_+^0) \frac{\partial (\ln c_e)}{\partial x} \frac{\partial \Phi_e}{\partial x} \right] dx \quad (6.24)$$

The battery heat sources are obtained from the electrochemical model, and they consist of two parts: reaction heat (q_r , (6.23)) due to reaction overpotential and ohmic heat (q_j , (6.24)) produced by charge transport in electrodes and electrolyte. Another part, reversible heat (or entropy heat), is ignored in simulations because it was proved to be negligible at high rate discharges in our previous work [51]. The term l in the equations indicates the overall thickness of a single electrochemical cell using half thickness current collectors.

2) Nail region heat source:

$$q_n = \frac{I_{dis}^2 R_n}{V} \quad (6.25)$$

In the equation, I_{dis} is the current during the nail penetration process, which is automatically updated in the coupling model when the nail site resistance, R_n , is input as the initial condition. The denominator V is the volume of the penetrated nail and can be calculated with $\pi D^2 t/4$, where D is the diameter of the nail, and t is the thickness of nailed battery. To obtain the resistance at the nail site, batteries were first discharged to “dead” using an external circuit and then penetrated. Batteries’ resistances were measured by an analyzer after penetration, which are taken as nail location resistances and utilized in the model. A summary of the resistance information of different batteries is given in Table 6.3, and a photograph of the “dead” batteries with nails is presented in Fig. 6.2.

To select a suitable time step for the simulations, time steps of 10 s, 1 s, and 0.1 s were first used to compare their effect on a 0.65 Ah battery nail penetration process. From the tests, it was found that a 10 s time step is not adequate to capture the quick temperature variations of the battery and lead to discrepancy from the other two time steps, while the 0.1 s time step is more computationally expensive (a solving time of 24420 s) than the 1 s time step (a solving time of 4966 s), identical temperature curves were obtained.

Consequently, a 1 s time step is selected in this work. For each time step, both the electrochemical and thermal model will re-evaluate their relevant parameters, e.g., current density, temperature, heat source, etc., prior to computation.

Table 6.3. Battery parameters used in the nail penetration model.

Battery No.	1	2	3	4
Layers of the electrochemical cells	23	40	72	102
1 C current density ($A\ m^{-2}$)	18.8	13.3	11.6	8.2
Internal resistance ($m\Omega$)	~ 102	~ 54	~ 10	~ 6
Nail site resistance ($m\Omega$)	~ 100	~ 50	~ 10	~ 10

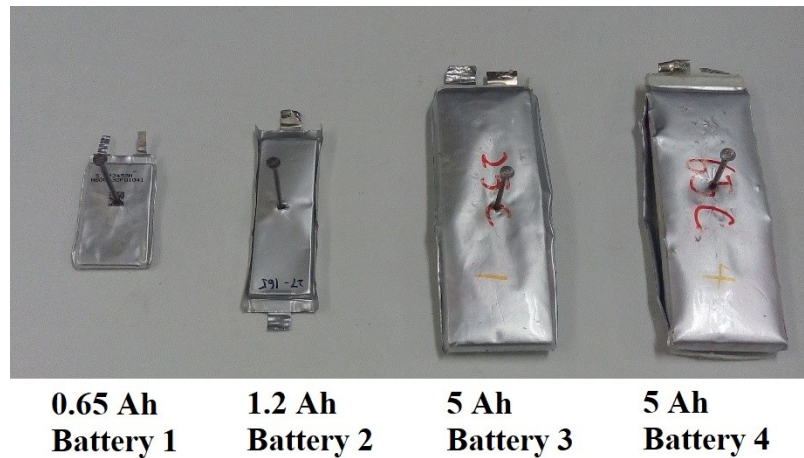


Figure 6.2. Photograph of nailed batteries used for determining nail site resistances.

This study places a special emphasis on predicting the occurrence of thermal runaway through examining temperature changes prior to thermal runaway. The chemical reactions and corresponding heat generations after thermal runaway taking place will not be calculated. As stated in Refs. [113, 133], the transition temperature or onset temperature for self-heating of the $LiCoO_2$ battery is at about $200^\circ C$ to $210^\circ C$. In this study, if the maximum temperature ($T_{real\ center}$ in Fig. 6.1a) exceeds $210^\circ C$ during simulation, the battery is considered at a great risk of thermal runaway. The method developed in this work can

also be applied to other types of batteries by changing the transition temperature according to the battery chemistry.

6.4 Results and Discussion

6.4.1 External Short Circuit

External short circuit tests were carried out on all batteries. The temperature and voltage curves of batteries No. 1 and 2 are plotted in Fig. 6.3. As can be seen, the connection of electrode tabs induces a dramatic drop in battery voltage. Meanwhile, the temperatures of the batteries increase significantly with maximum values of 115°C and 103°C observed at about 70 s at the centers of batteries No. 1 and 2, respectively. The inset shows that the temperature at the corner increases faster than the center temperature at the initial stage due to the earlier acquisition of current on the electrode tabs. Afterwards, because of the better heat dissipation environment at the battery corner, the temperature at the battery corner becomes relatively lower than the center temperature. Overall, the temperatures at different locations of the externally shorted batteries increase at a similar rate because of the evenly distributed heat generation in the battery.

The external short circuit simulation is then performed by setting the obtained voltage data as the cathode boundary condition in the coupling model. Only the heat generated from the battery itself, including ohmic heat and reaction heat, is considered in the thermal model. The simulation results of battery No. 1 and No. 2 are shown in Fig. 6.4a and b, respectively. As can be seen, the simulated temperatures are well consistent with the experimental results for the 0.65 Ah battery. For the 1.2 Ah battery, the simulated temperature is relatively lower than the experiment. This is because as the battery capacity increases and internal resistance decreases, the short circuit current becomes higher and more heat is generated on the external circuit, especially on the battery tabs after clamping the wire. During tests, it was found that the contact region between the clamps and 1.2 Ah battery tabs became red and hot for several seconds after the short. In simulation, the heat transferred from external heat sources was not considered, which can slightly increase the battery temperature.

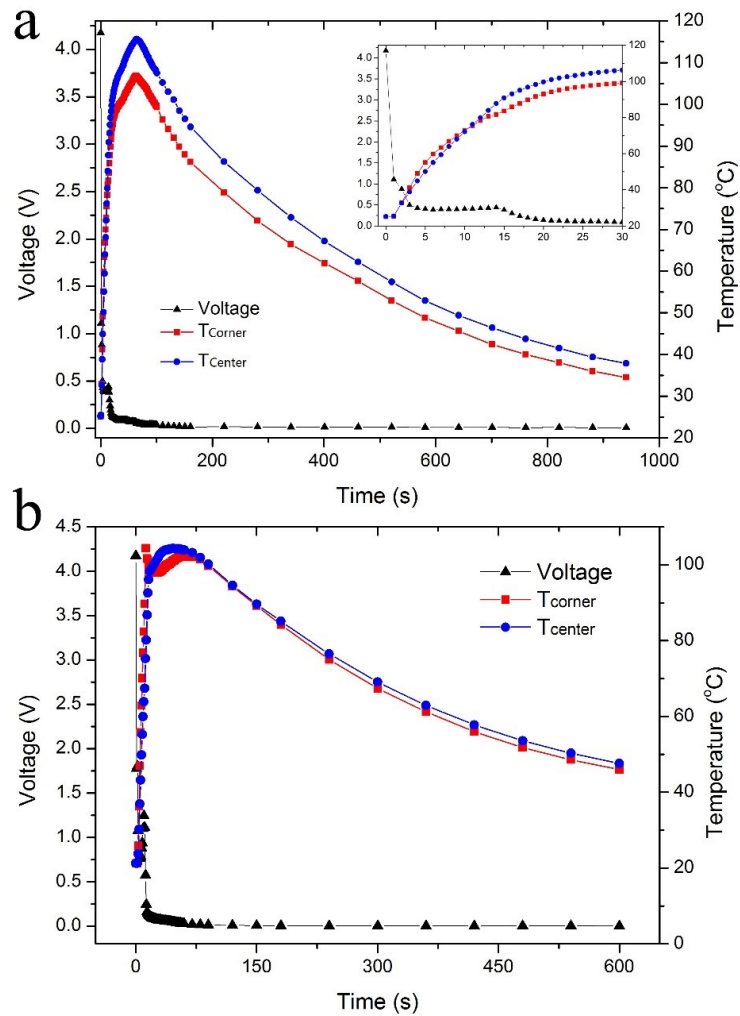


Figure 6.3. Temperature and voltage curves of a) 0.65 Ah and b) 1.2 Ah batteries externally shorted in ambient conditions.

During the external short circuit tests, a portion of heat is generated on the 20 m Ω connecting wire. As the battery capacity increases, the internal resistance of batteries No. 3 and 4 drop to 10 m Ω and 6 m Ω , respectively, causing a more considerable heat production on the external wire. As a result, the contact regions between the clamps and positive tabs (aluminum) of batteries No. 3 and 4 were broken during the tests. Thus, it can be concluded that the external short circuit has a greater impact on low capacity batteries due to their high internal resistance, and in real life applications, the external short circuit can be hindered with the use of fuses, which can automatically cut off the discharge process when the current exceeds a pre-set limit.

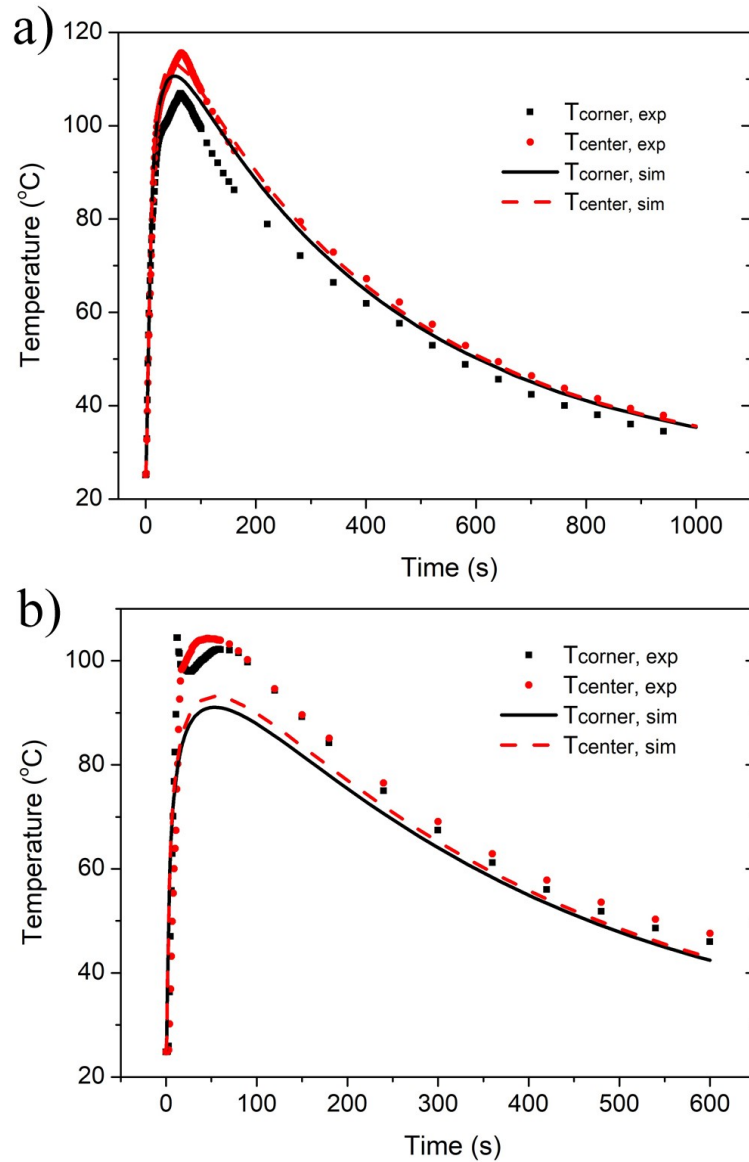


Figure 6.4. Simulated temperature curves of the externally shorted a) 0.65 Ah battery and b) 1.2 Ah battery.

6.4.2 Nail Penetration

Nail tests and simulations were first conducted on 0.65 Ah batteries. The experimentally obtained temperature and voltage curves are compared with simulation results in Fig. 6.5, and the electrode current density during the simulation is plotted in Fig. 6.6. It is seen that the simulation results agree well with the experimental data, and both have a maximum temperature of 118°C. The peak temperature of the nail is higher than that of the other recorded locations on the battery because the high thermal conductivity of

the nail makes it more prompt in reflecting the temperature at the nail region. In comparison, the temperature at corner has the lowest value, and this is attributed to its preferable cooling environment.

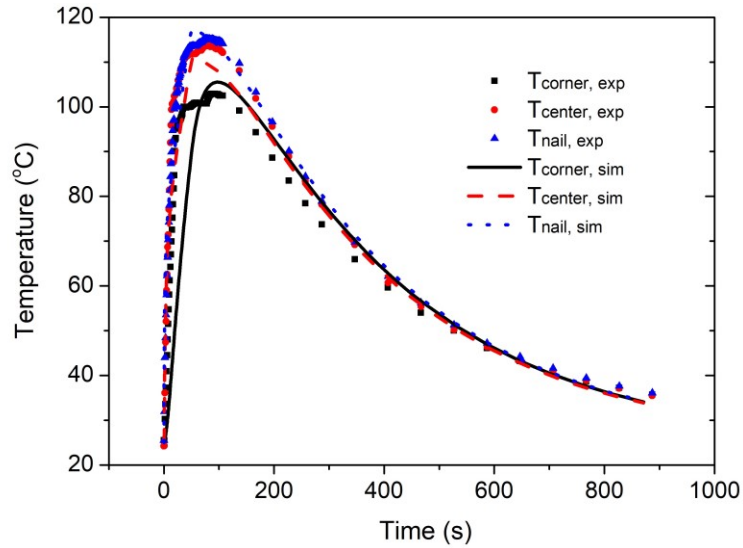


Figure 6.5. Comparison of the experimental and simulated temperature curves of the nailed 0.65 Ah battery.

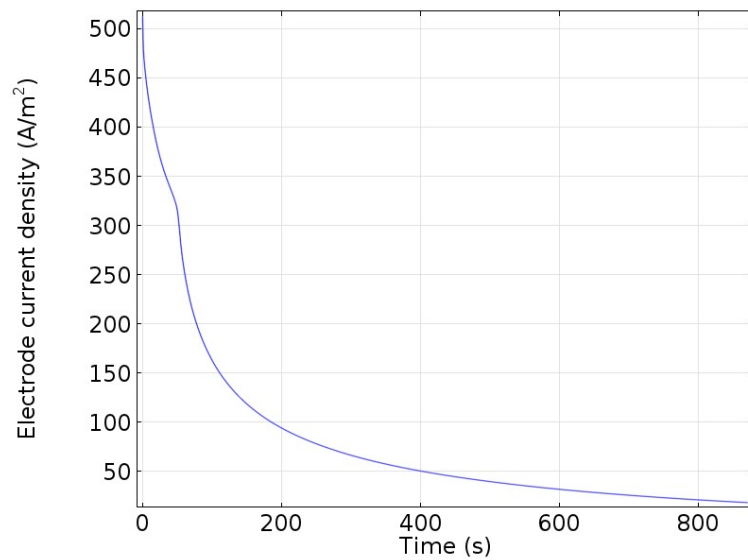


Figure 6.6. The simulated electrode current density of the nailed 0.65 Ah battery.

Fig. 6.7 shows the simulated temperature contours of the 0.65 Ah battery at different times after the nail penetration. The graphs indicate that more heat is generated at the nailed

region and the heat produced in that region quickly distributes to the whole cell. The maximum temperature, 405.23 K (132.08°C), is reached at 50 s at the center of the nailed battery.

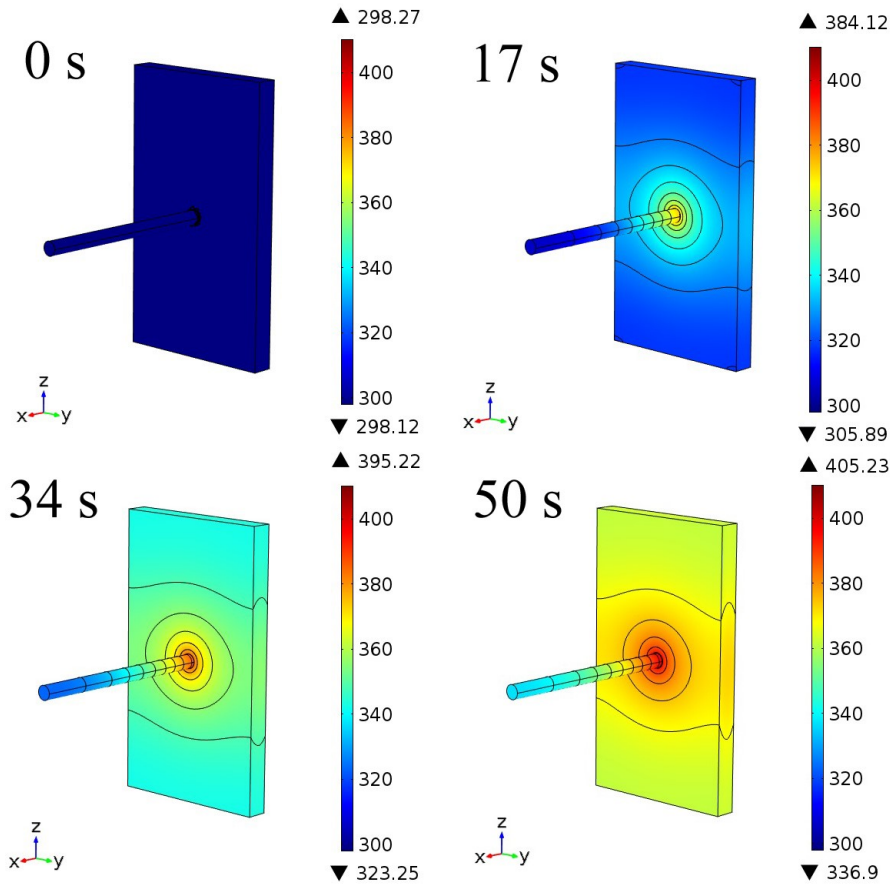


Figure 6.7. The temperature contours of the nailed 0.65 Ah battery at different times after penetration.

Three 1.2 Ah batteries were then penetrated and one of them experienced thermal runaway. Fig. 6.8a & b show the temperature and voltage curves of non-thermal runaway and thermal runaway batteries, respectively.

Similar to the case of the 0.65 Ah battery, the highest temperature of the non-thermal runaway battery is found at the nail, as shown in Fig. 6.8a, with a value of 183°C, and the lowest temperature is observed at the corner. Compared to the 0.65 Ah battery, a bigger temperature difference between the battery center and corner is found on the 1.2 Ah battery. This is due to the fact that the increase of battery capacity leads to a smaller internal

resistance and a larger battery size, which means more heat is generated at the nail location and a longer time is required to transfer the heat to the battery edges.

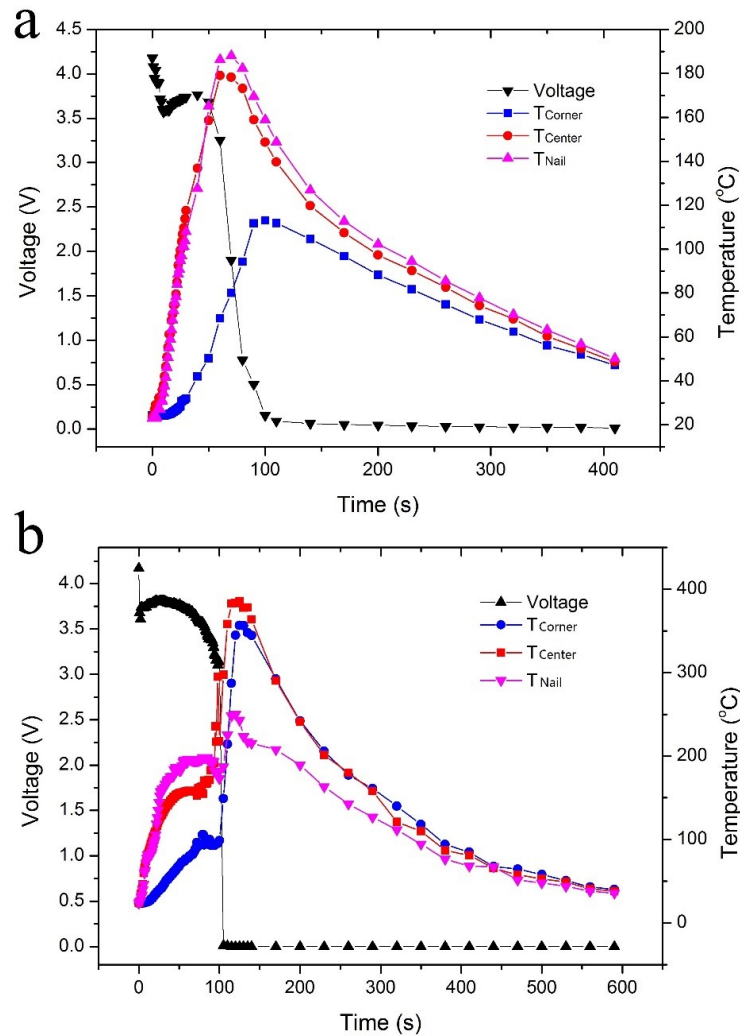


Figure 6.8. Experimentally recorded temperature and voltage curves of the 1.2 Ah batteries that a) did not experience and b) experienced thermal runaway during nail tests.

The 1.2 Ah battery shown in Fig. 6.8b experiences thermal runaway at 100 s. The heat accumulated at the nail location increases the internal temperature and triggers chemical reactions in the LiCoO₂ battery. To explain why the 1.2 Ah batteries have different temperature responses after being penetrated, a penetration simulation is performed and the results are plotted in Fig. 6.9. Besides the temperatures at the three sampling points, the temperature at the real center of the nail location is also presented, which has the highest value but is unable to be recorded during experiments. As can be seen, the temperatures at

the battery corner, battery center, and nail surface match well with those acquired experimentally in Fig. 6.8a. As for the temperature at the battery real center, it reaches 215°C and is right above the transition temperature, 210°C. The distinct thermal responses of these 1.2 Ah batteries can thus be explained: once penetrated, the maximum temperature of these batteries can reach the transition temperature. If the heat generated by the localized chemical reactions is well transferred and dissipated to its surroundings, the exothermic reaction may not spread over and the battery may not experience venting, but if the localized reactions are persistent, thermal runaway may be initiated. Slight variations between individual batteries, cooling environments, as well as nail tip geometries could make testing results different. Nevertheless, attentions should be paid on the 1.2 Ah battery due to its ability to trigger thermal runaway.

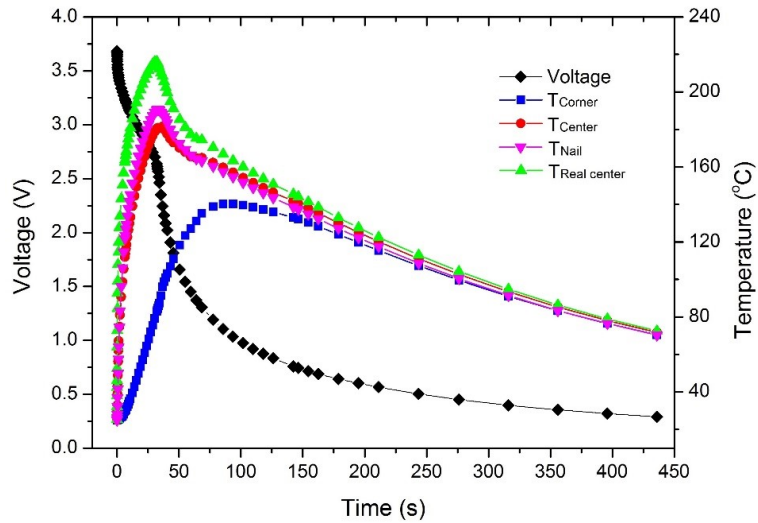


Figure 6.9. Simulated temperature and voltage curves of the nailed 1.2 Ah battery.

Lastly, nail tests were performed on 5 Ah batteries No. 3 and 4. These two batteries have different electrode thicknesses, and two of each battery were nailed. All the 5 Ah batteries suffered from thermal runaway in tests, and one of the batteries, No. 4, even caught fire. The temperature and voltage curves of batteries No. 3 and 4 during nail tests are plotted in Fig. 6.10a & c, and the corresponding simulation results are shown in Fig. 6.10b & d, respectively. As stated earlier, the exothermic chemical reactions and corresponding heat generation during thermal runaway will not be included in this study. Since thermal runaway completely changes the origin of the heat source from Joule heating

to chemical reaction heating and from the nail region to the entire battery, the temperature profiles obtained experimentally and numerically are different.

Nevertheless, the model accurately predicts the occurrences of thermal runaway and their approximate start times. During experiments, battery No. 3 and 4 went into thermal runaway at 3 s and 2 s, respectively. To clearly compare the simulation and experimental data, horizontal lines of $T = 215^{\circ}\text{C}$ are plotted in Fig. 6.10b and d to indicate the transition temperature, which is modified on the basis of the earlier nail tests on the 1.2 Ah batteries. In Fig. 6.10b and d, batteries No. 3 and 4 reach the transition temperature at 2.5 s and 0.6 s, respectively, which are close to the occurrence times of the thermal runaways in the nail experiments. The time of thermal runaway in experiments is a bit longer than the simulations, which is probably because it would take some time to trigger the thermal runaway after the batteries reach the onset temperature.

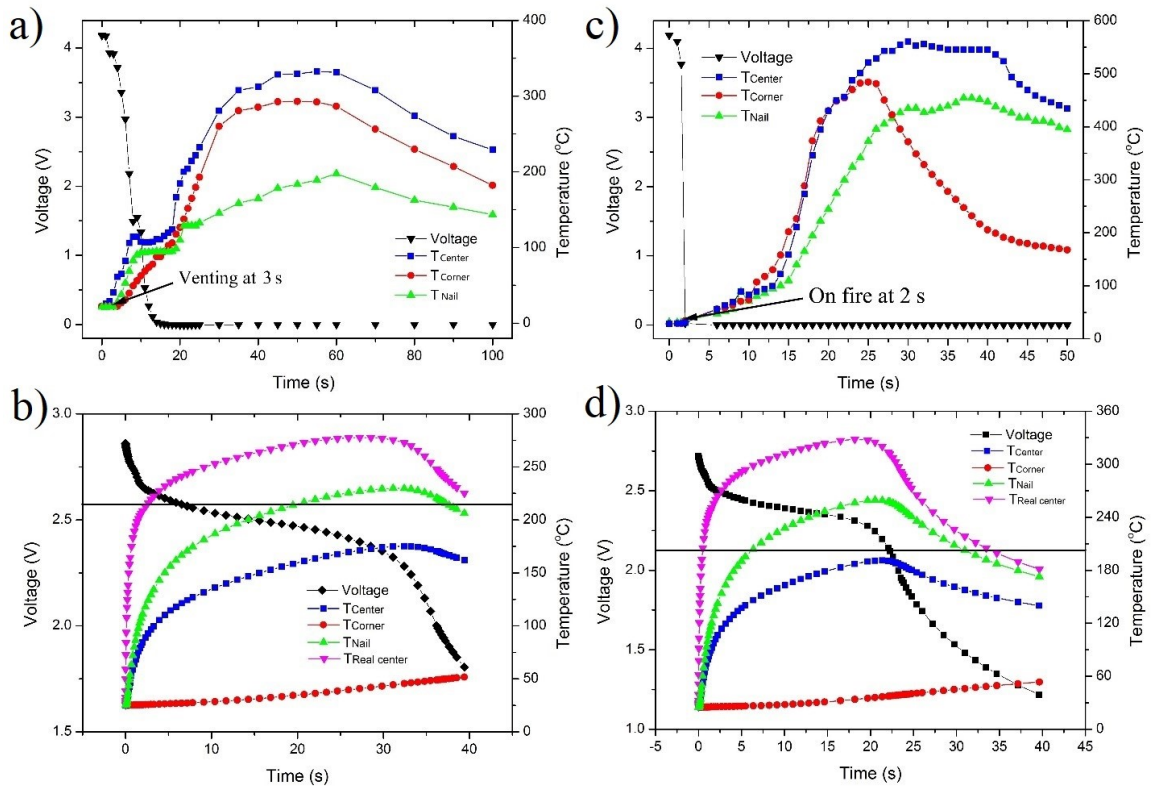


Figure 6.10. Temperature and voltage curves of the 5 Ah batteries during nail penetration tests: thick electrode battery (battery No. 3) in a) experiment and b) simulation, and thin electrode battery (battery No. 4) in c) experiment and d) simulation.

The impact of electrode thickness on the performance of nailed batteries can be determined by comparing Fig. 6.10b and d. When having the same capacity, the thin electrode battery has a lower internal resistance and a larger short circuit current than the thick electrode battery. Therefore, the thin electrode battery releases all the energy quicker and reaches a higher temperature during nail tests. As shown in Fig. 6.10b and d, battery No. 4 reaches its peak temperature of 328.2°C in only 18 s, while it takes 27 s for battery No. 3 to reach its peak temperature of 277.6°C. The low internal resistance is an advantage of the thin electrode battery during normal charges and discharges, but special attention should be paid to safety issues of the battery.

During the design process of Li-ion batteries, technicians and engineers can implement the coupling model developed in this work to evaluate the safety performance of the batteries. Through understanding the electrode chemistry of batteries, measuring their internal parameters, and testing the resistance at the nail location, the safety and the thermal responses of the batteries during internal short circuits can be determined with the model. One should also consider the effects of states of charge and cooling environments while performing the evaluation.

6.5 Summary

In this Chapter, external short circuit tests and nail penetration tests were performed on batteries of different capacities. In external short tests, 0.65 Ah and 1.2 Ah batteries experienced a dramatic temperature rise and voltage drop, which is attributed to their high internal resistance. As for larger capacity batteries that have lower internal resistances, more heat was concentrated at the contact region between the clamp and battery tabs, resulting in the automatic shutdown of the external short processes. In contrast, during the nail penetration tests, as the battery capacity increases, a higher current flow was generated at the nailed region and triggered the accumulated heat generation, which finally led to the occurrence of thermal runaway.

A modified electrochemical-thermal coupling model was also developed to simulate the short circuits. Simulated temperature curves of the externally shorted battery are in good consistence with the experiment when the battery voltage is set as the cathode

boundary condition. In simulating the nail penetrations, a Joule heat source from the nail region is added to the model. The model has been proved reliable in predicting the temperature changes of non-thermal runaway batteries and estimating the occurrence and approximate start time of thermal runaway of unsafe batteries.

Chapter 7. A Comprehensive Study on Li-ion Battery Nail Penetrations and the Possible Solutions

7.1 Overview

Li-ion batteries are the state-of-the-art power sources for portable electronics, electric vehicles, and aerospace applications. Safety issues regarding Li-ion batteries have aroused particular attention lately after several accidents reported in recent years. As can be revealed from Chapter 6, external short circuits can be managed with the use of fuses, while the internal short circuits cannot be blocked due to the short circuit loop is inside the battery. Nail penetration test is typically taken to simulate the internal short circuits of Li-ion batteries, and it is one of the most dangerous abuse conditions for Li-ion batteries due to the accumulated heat generation, which could give rise to thermal runaway and could damage the entire energy storage system. This type of abuse condition can be correlated to the damaged Li-ion batteries equipped on EVs during crashes. In this Chapter, the electrochemical-thermal coupling model developed in Chapter 6 is implemented to study the nail penetration process of Li-ion batteries. A comprehensive parametric study is carried out to investigate the effects of battery capacity, internal resistance, and nail diameter on the electrochemical and thermal behaviors of Li-ion batteries during the penetration process. Three possible solutions including decreasing the state of charge, improving the heat dissipation, and increasing the contact resistance, are numerically studied in preventing thermal runaway. In addition, the effectiveness of a hydrogel-based BTM system in suppressing thermal runaway and preventing thermal runaway propagation is experimentally verified on Li-ion batteries and battery packs.

7.2 Experiments

The experiments consist of two parts: contact resistance tests, and nail tests. In the contact resistance tests, a total of 40 batteries were used, which include twenty 0.65 Ah batteries, ten 3 Ah batteries, and ten 5 Ah batteries, and their specifications are summarized in Table 7.1. During the tests, the batteries were discharged to “dead” using an external

circuit and penetrated by polished steel nails with different diameters. A multimeter (HP 4263B LCR Meter) was then used to measure the resistance between two electrode tabs, which is taken as the contact resistance at the short circuit region. After the tests, the recorded contact resistances were plotted vs. the contact area between nail and battery (πDt , where D is the nail diameter, and t is the battery thickness) in Fig. 7.1. The expression, $16.3 \text{ m}\Omega/A$, given in Ref. [43], is found to have derivations from the obtained data, which is because the specific contact resistance of $16.3 \text{ m}\Omega \text{ cm}^2$ is from estimations. In real conditions, some factors could affect the results, for example, the penetration of the nail will push a part of the battery pouch in and might alter the contact between the nail and electrochemical cells. A logistic fit on OriginPro was used to express the experimental data as follows:

$$R_n = 6.75 + \frac{546}{1 + \left(\frac{A}{8.77}\right)^{2.69}} \quad (7.1)$$

where R_n is the contact resistance, in $\text{m}\Omega$, and A is the contact area between the nail and battery, in mm^2 . The R-squared value of this logistic fit is 0.906, which is closest fit that can be obtained from the given options in the OriginPro, such as linear fit and polynomial fit.

The systematic uncertainty during the resistance measurement is mainly due to the accuracy of the multimeter, while the random uncertainties consists of the contact resistance between the terminals of the multimeter and the batteries, as well as the difference between the geometry of the nail tips and the surface roughness of the nails. The multimeter was operated strictly according to the manual, and the multimeter has an accuracy of $\pm \left(0.85 + \frac{12}{R_n} + \frac{R_n}{2.8 \times 10^8}\right)\%$. To minimize the contact resistance, bolts were used to fasten the battery tabs and the multimeter terminals. To reduce the differences between nails, smooth finishing nails with the same tip geometry were used in the tests. Meanwhile, the nails were cleaned with ethanol and dried with fibre cloth prior to use.

Table 7.1. Specifications of LiCoO₂ batteries used in short circuit simulations or tests*.

Battery No.	1	2	3	4	5
Thickness [mm]	3.8	4.5	5 (20)	8.5	41
Width [mm]	30	28	45	45	45
Length [mm]	52	82	133	133	175
Initial voltage [V]	4.19	4.19	4.19 (16.78)	4.19	16.78
Nominal capacity [Ah]	0.65	1.2	3	5	8
Internal resistance at 25°C [mΩ]	100	54	14	6	-
Layers of electrochemical cells	23	40	44	102	-

* Battery 1, 3, and 4 are numerically studied; All batteries undergo nail tests.

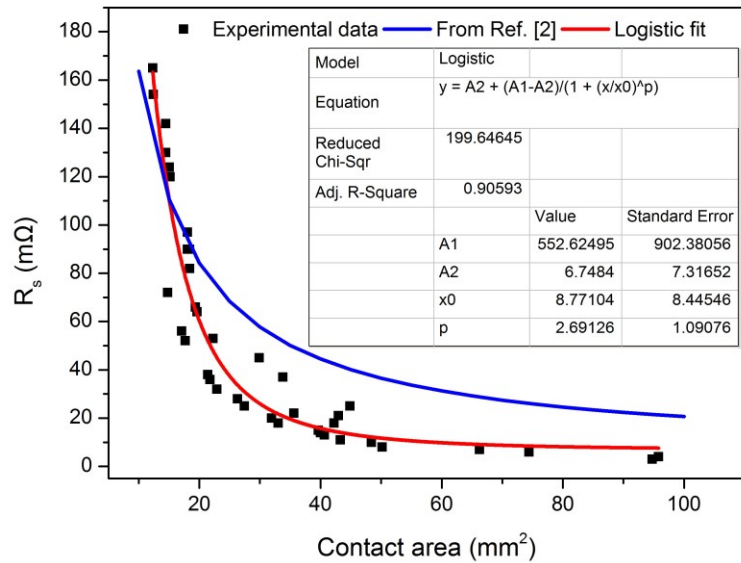


Figure 7.1. A plot of contact resistance R_n vs. contact area between nail and battery.

To validate one of the solutions, improve heat dissipation, in preventing thermal runaway and its propagation in battery pack, nail tests were carried out on the batteries and battery packs with and without a hydrogel BTM system. Hydrogel is made of more than 99 wt. % of water and high-molecular weight polymers that can retain the water in solid state. The hydrogel BTM system has been studied by Zhang et al. [13] in managing the heat of Li-ion batteries during normal high-rate discharges. Since water can absorb a

significant amount of heat during evaporation, the hydrogel-based BTM system was considered to manage the heat generated by batteries during battery nail penetrations.

The nail implemented during the tests is stainless-steel nails with a diameter of 2.5 mm. For tests on battery packs, only the top battery in the battery pack was penetrated to investigate the thermal runaway propagation phenomena. In the tests, two thermocouples were utilized to measure the battery temperature: one was attached at the center of the battery and the other thermocouple was located at the battery corner, and one more thermocouple was used to measure of nail temperature. During nail tests on battery packs, thermocouples were placed at the center of each battery. Besides temperatures, the voltages of batteries and battery packs were also recorded in all tests.

The hydrogel thermal management system used in this study was obtained by directly injecting deionized water into containers where batteries were placed in the center and sodium polyacrylate (PAAS) particles were evenly spread. The containers have similar lengths and widths as the batteries but are twice as thick. The mass fraction of PAAS in the hydrogel was 1%.

7.3 Results and Discussion

7.3.1 Simulations on Batteries of Difference Capacities

With the validated model, the thermal responses of Battery 1, 3 and 4 listed in Table 7.1 are simulated and compared in the nail penetration tests using 1.8 mm nails. The 1.8 mm nails were used in the simulations because they could cause the most severe temperature increase, as explained in Section 7.3.2. Fig. 7.2a-c show the temperature, battery heat source, and boundary (nail region) heat source curves of the three batteries as a function of time.

In Fig. 7.2a, the hollow symbols represent the maximum temperatures inside the batteries, and the solid symbols indicate the temperatures at the battery surface center. It is seen that among the three batteries, the 0.65 Ah battery has the lowest temperatures in both locations. The explanations are given from both the battery level and the electrochemical

cell level. From the battery level, the 0.65 Ah battery has the highest internal resistance and contact resistance of 100 m Ω and 52 m Ω , respectively. Since a battery penetration can be treated as a high-rate discharge process, and the discharge current is dependent on the sum of the battery and contact resistances. Thus, with the same initial electric potential of 4.2 V, the 0.65 Ah battery will generate the lowest short-circuit current. Meanwhile, a relatively low capacity is also helpful in reducing the total heat generation. On the electrochemical cell level, the 0.65 Ah battery has the thickest electrodes among the three batteries, as given in Table 6.2. The thick electrodes could lead to severe diffusion limitation, concentration overpotential, and finally restrain the nail penetration process [53]. In comparison, both the 3 Ah and 5 Ah batteries experience dramatic temperature rises after penetrations, with the maximum temperature soaring up to 439°C and 492°C, respectively, which have already exceeded the transition temperature, 215°C, and which give rise to thermal runaway. With using thinner electrodes, both the 3 Ah and 5 Ah batteries have significantly lower internal resistance as compared to the 0.65 Ah battery. Furthermore, both of the batteries are thicker than the 0.65 Ah battery, thus leading to low contact resistances of 29.18 m Ω and 12.3 m Ω for the 3 Ah and 5 Ah batteries, respectively. As a result, high short-circuit currents are produced during penetrations and give rise to the rapid temperature rise.

Besides the maximum temperatures, the temperature distributions on the three batteries are very different. As shown in Fig. 7.2a, the difference between the maximum and surface temperatures becomes bigger as the battery capacity increases. For the 0.65 Ah battery, the battery resistance is higher than the contact resistance, which will generate more heat on the battery instead of at the nail location. Consequently, a more uniform temperature distribution will be achieved. In contrast, the internal resistances of the 3 Ah and 5 Ah batteries are 14 m Ω and 6 m Ω , respectively. These values are much smaller than the contact resistances, which will engender concentrated heat generation at the nail location instead of an even battery heat generation. Fig. 7.2b and c compare the heat generation rates of the battery level and at the contact region. It can be seen that the 0.65 Ah battery generates more heat at the battery level due to its thicker electrodes and higher internal resistance, while the 3 Ah and 5 Ah batteries have much higher localized heat generation due to the higher short-circuit currents.

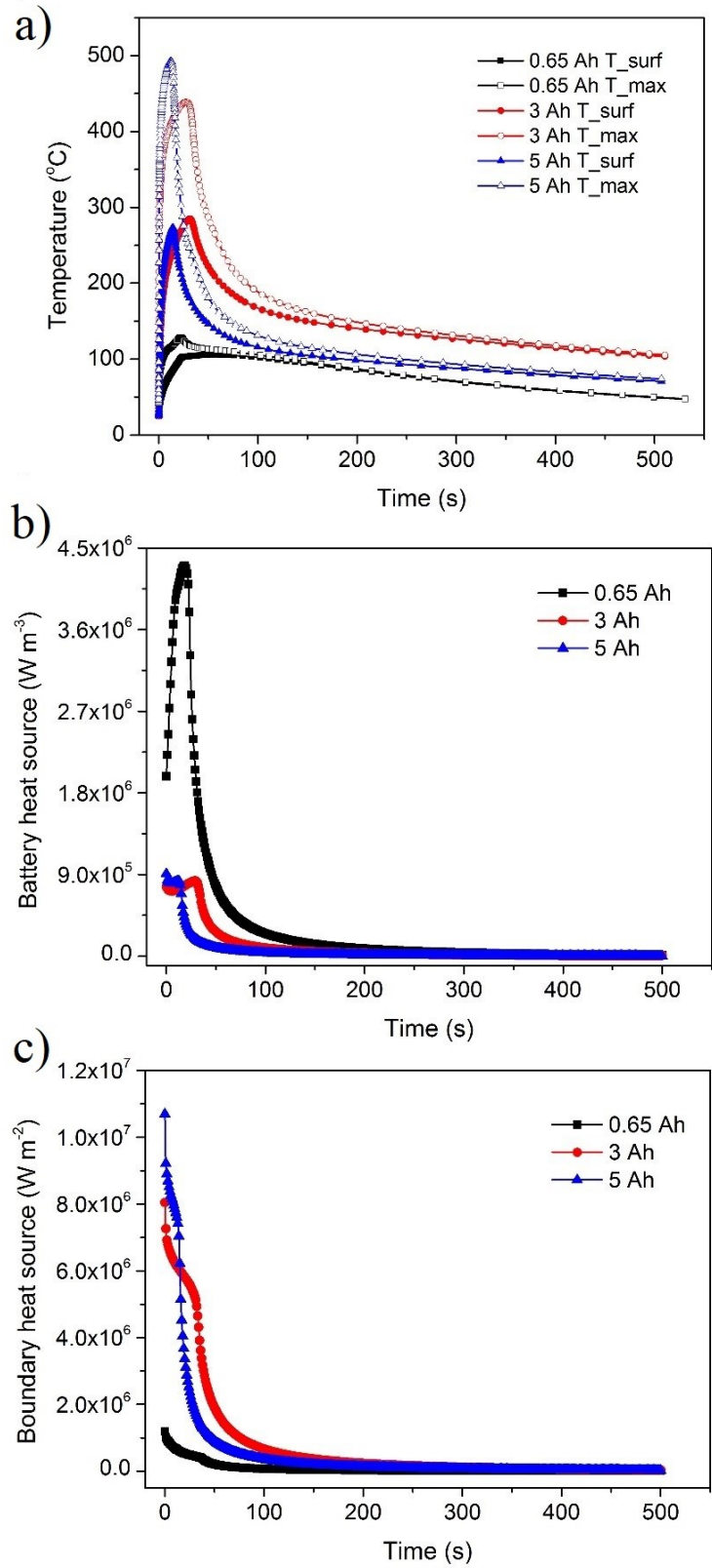


Figure 7.2. Comparison of the a) temperature, b) battery heat source, and c) boundary heat source curves of the three batteries during the 1.8 mm-nail penetration simulations.

It is thus concluded that in battery penetrations, thick electrodes will be helpful in hindering thermal runaway, and a battery level heat generation is preferable than localized heat generation in improving battery safety.

7.3.2 Effects of Battery Resistance and Nail Diameter

After comparing the simulation results of the three batteries, it is seen that both the 3 Ah and 5 Ah batteries experience strong thermal responses due to the accumulated heat generation at the nail region, which is found to be closely related to their internal resistance and the contact resistance (a function of nail diameter).

In order to investigate the effects of the internal resistance and nail diameter on the thermal behaviors of Li-ion batteries during nail penetrations, the internal resistances of the 3 Ah and 5 Ah batteries, as well as the nail diameter are adjusted in appropriate ranges in simulations, 5-60 mΩ for the 3 Ah battery, 2.5-40 mΩ for the 5 Ah battery, and 0.5-3.6 mm for the nail diameter. One can also regard the change of battery resistance as the battery's aging effect. With the change in battery resistance, (6.23) and (6.24) will be unable to accurately simulate the battery heat source. As a result, a battery heat source from Ref. [13, 50] is used, which takes into account the effect of battery resistance, and can give more reasonable solutions.

$$Q = I(U - V) - I \left(T \frac{dU}{dT} \right) \approx IR_b^2 \quad (7.2)$$

where Q is the total heat generation. The first term on the right-hand side of Q includes the ohmic loss inside battery, charge transfer overpotential at the interface, and the mass transfer limitations, where U and V are the open circuit potential and battery operating potential, respectively. The second term is the reversible heat and is neglected due to the high discharge current. Because the overpotential, diffusion limitation, and the ohmic loss can be reflected in the battery internal resistance, the rightmost term is capable of giving an accurate battery heat source.

Fig. 7.3a and b show the maximum temperature contours of the 3 Ah and 5 Ah batteries, respectively. 72 simulations were carried out for each battery using different battery resistance and nail diameter combinations, and the maximum temperature from

each simulation was taken and used to generate the contour. It is seen that for battery penetrations with a specific nail diameter, the decrease of battery internal resistance yields higher maximum temperatures. This is because as the battery resistance becomes lower a higher short circuit current will be produced to generate more heat in the nail region. Afterward, the effect of nail size on the simulation results is studied. From the projection diagram of the 3 Ah battery, it is seen that the peaks of parabolas are shifting from 1.75 mm to 1 mm nail as the battery resistance increases from 5 mΩ to 55 mΩ, which indicates that a low internal resistance battery is more dangerous with thicker nails. A similar trend is also observed with the 5 Ah battery.

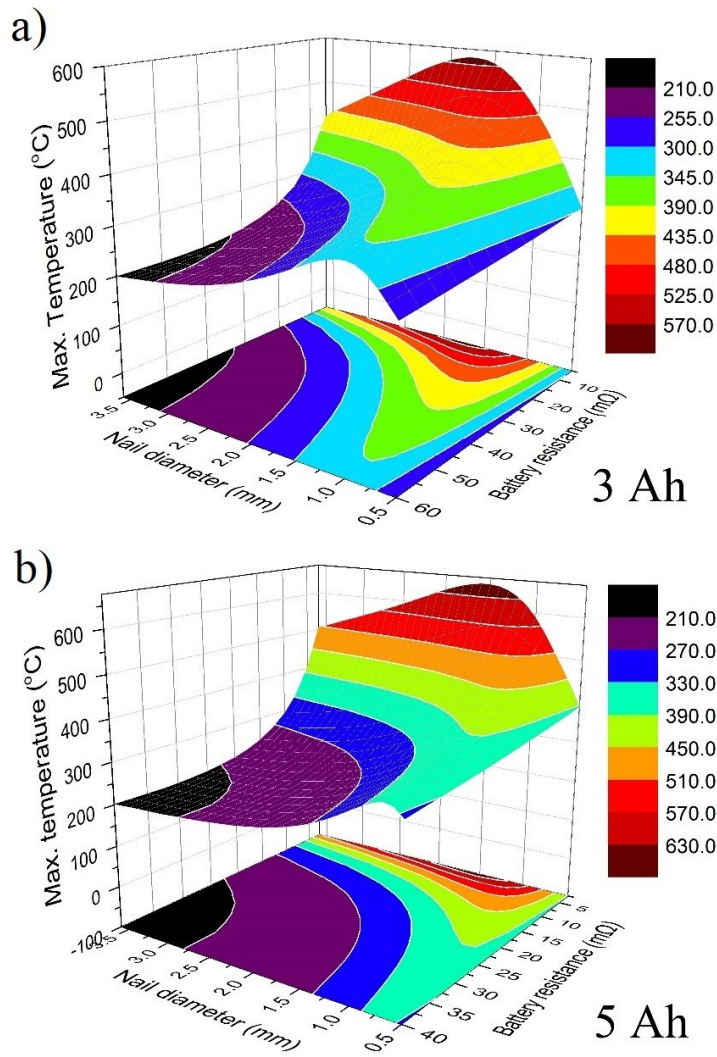


Figure 7.3. The maximum temperature contours of the a) 3 Ah and b) 5 Ah batteries in penetration simulations using different nail diameters and battery internal resistance.

In both contours, the lowest temperature regions are located at the bottom left, penetrations of high internal resistance batteries using thick nails. In this region, due to the low contact resistance and high battery resistance, most of the heat will be generated on the battery, which eliminates the concentrated heat and favors heat dissipation. However, in real cases, the combination of high battery resistance and thick nails cannot totally guarantee batteries are free of thermal runaway. Because the nail penetration is a process where the contact area changes from small to large, i.e., contact resistance varies from high to low, which is not considered in the simulations, different results may be obtained as the penetration speed changes.

7.3.3 Comparison of Strategies to Prevent Thermal Runaway

Although current Li-ion batteries have been assembled with advanced separators that can automatically close the porous membrane at high temperatures to prevent the ion transfer and thus to shut down the electrochemical reactions [146], the temperature inside the nailed battery will soar up and exceed the transition temperature of thermal runaway before the closure of all separators. As a result, a series of exothermic chemical reactions will take place in the region close to the nail and propagate to the entire battery.

Three possible solutions: decreasing state of charge (SOC), improving heat dissipation, and increasing contact resistance, are investigated on the 3 Ah and 5 Ah batteries during the 1.8 mm-nail penetration simulations, and the feasibility of each strategy is discussed in detail.

7.3.3.1 Decrease State of Charge

The state of charge is an indication of the available capacity stored in a Li-ion battery as a percentage of the rated capacity. For both batteries, the SOC is 100% at 4.2 V, and 0% at 3 V. Table 7.2 lists the anode and cathode stoichiometry of the 3 Ah and 5 Ah batteries at the assigned SOC's used in simulations. In Fig. 7.4a, the maximum temperatures of both nailed batteries at different SOC's are plotted. As can be seen, the maximum temperature drops as the SOC decreases. However, at the selected SOC's, only the fully discharged

batteries, SOC = 0%, have a maximum temperature below the thermal runaway transition temperature. Fig. 7.4b and c compare the boundary heat sources of the 3 Ah and 5 Ah batteries at different SOC, respectively. With a higher SOC, more energy is produced at the nail region, as represented by the area below the heat generation rate curve. It is also seen that the initial heat generation rates are similar at different SOC, which is due to the high voltage of the Li-ion batteries. As a result, the available energy in the battery is rapidly converted to heat at the nail region before the heat is efficiently dissipated through convection and radiation. Therefore, decreasing the SOC is not a feasible approach to prevent Li-ion batteries from thermal runaway in nail penetrations.

Table 7.2. The stoichiometry of 3 Ah and 5 Ah batteries at the assigned SOC.

SOC		100%	80%	60%	40%	20%	0%
3 Ah battery	Anode stoichiometry	0.8	0.678	0.556	0.434	0.312	0.19
	Cathode stoichiometry	0.42	0.526	0.632	0.738	0.844	0.95
5 Ah battery	Anode stoichiometry	0.8	0.674	0.548	0.422	0.296	0.17
	Cathode stoichiometry	0.42	0.523	0.627	0.730	0.834	0.937

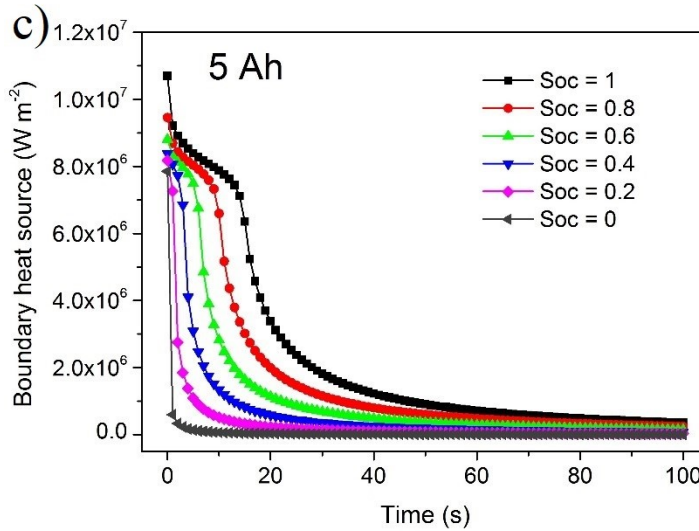
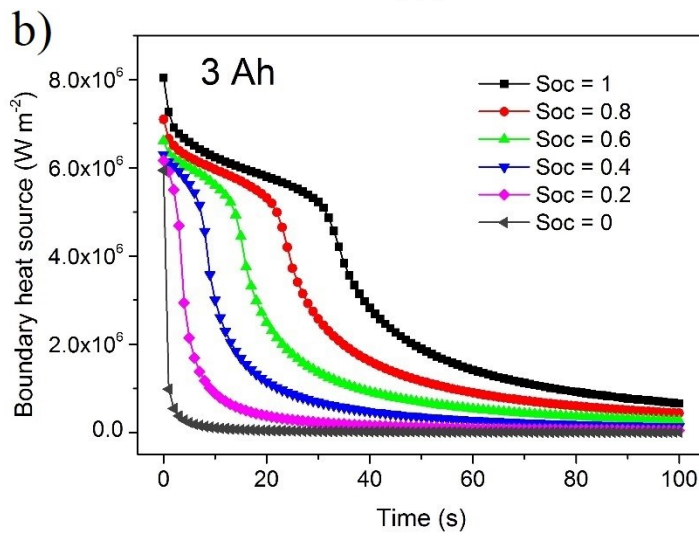
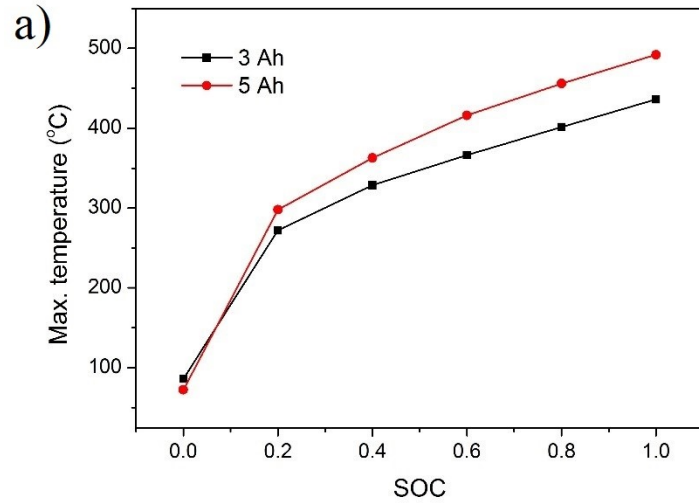


Figure 7.4. a) The maximum temperatures of the 3 Ah and 5 Ah batteries with different SOCs during the 1.8 mm-nail penetration simulations; The boundary heat sources of the b) 3 Ah, and c) 5 Ah batteries at different SOCs.

7.3.3.2 Improve Heat Dissipation

According to the energy conservation equation, the heat dissipation term can affect the temperature change of the Li-ion batteries. In this section, the convective heat transfer coefficient is adjusted in a range from 1 to 200 $\text{W m}^{-2} \text{K}^{-1}$ to study the thermal responses of the Li-ion batteries under different cooling conditions. A cooling environment with a convective heat transfer coefficient of 1 $\text{W m}^{-2} \text{K}^{-1}$ is similar to the condition where a battery is enveloped by insulating materials, and the heat transfer with a coefficient of 200 $\text{W m}^{-2} \text{K}^{-1}$ can represent an effective liquid cooling condition.

Fig. 7.5 plots the maximum and surface temperatures of the 3 Ah and 5 Ah batteries under different cooling conditions. For the 3 Ah battery, the maximum temperature experiences a 32.3°C drop from 438.5°C to 406.2°C as the h value increases from 1 to 200 $\text{W m}^{-2} \text{K}^{-1}$, which is about half the value of the surface temperature changes, from 284.8°C to 208.7°C. In comparison, the change of the maximum temperature of the 5 Ah battery is much smaller than the surface temperature drop, with values of 2.7°C vs. 56.9°C, respectively. Having a larger thickness, 8.5 mm vs. 5 mm, the reduction in the maximum temperature of the 5 Ah battery is much smaller than that of the 3 Ah battery. Because Li-ion batteries have a very low thermal conductivity in the thickness direction, as calculated from (6.20), the thicker the battery is, the longer time it will spend transferring the concentrated heat from the battery center to the surface for dissipation. Overall, it can be seen that the increase of heat dissipation at the battery surface has an insignificant effect on decreasing the maximum temperature, especially for thicker batteries. Nevertheless, effective cooling can lower the battery surface temperature, thus can hinder the propagation of thermal runaway in Li-ion battery packs. The relevant experimental results are given below.

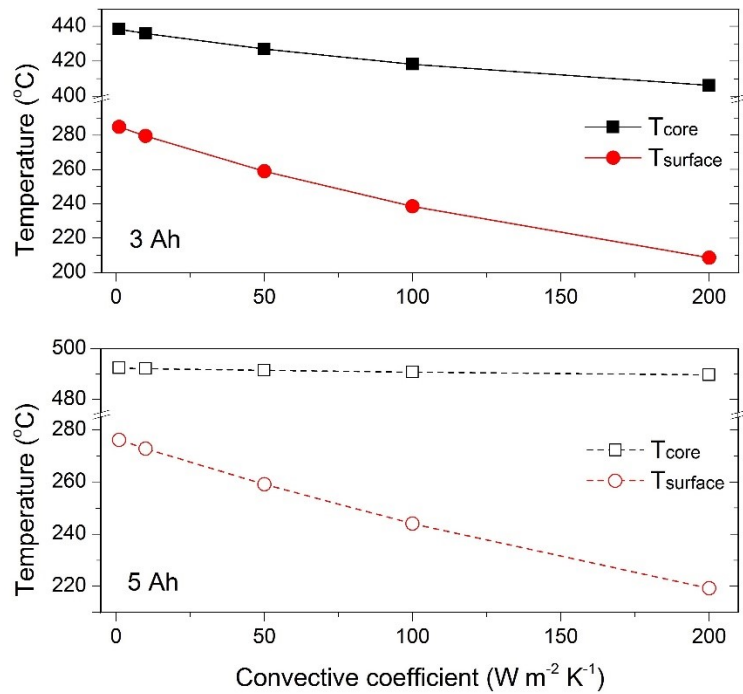


Figure 7.5. Plots of the maximum and surface temperatures of the 3 Ah and 5 Ah batteries under different cooling conditions during 1.8-mm nail penetration simulations.

Nail tests were first conducted on single batteries surrounded with hydrogel. The temperature and voltage data of Battery No. 1, 2, and 4 during tests are shown in Fig. 7.6 a, b and c, respectively. During the tests, thermal runaway did not occur on the 0.65 Ah (Battery 1) and 1.2 Ah (Battery 2) batteries, whereas the 5A (Battery 4) battery vented after penetration. Owing to the excellent ability of hydrogel in absorbing heat during evaporation, the maximum surface temperature of the batteries were maintained below 100°C. The battery safety is significantly improved when compared to the vented 1.2 Ah battery and a fire 5 Ah battery tested in Chapter 6.

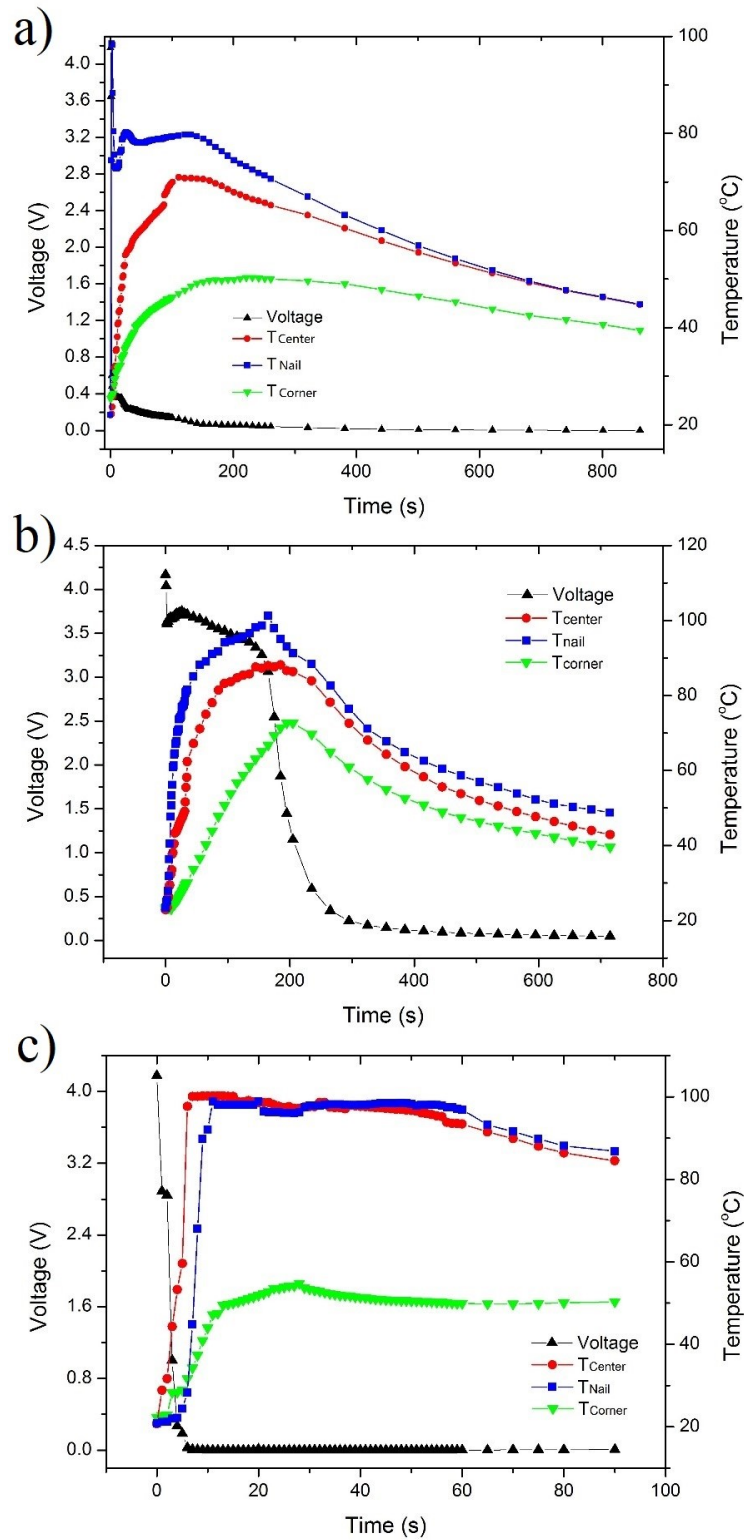


Figure 7.6. Temperature and voltage curves of the a) 0.65 Ah, b) 1.2 Ah, and c) 5 Ah batteries during nail penetration tests in a hydrogel-based BTM system.

The ability of the hydrogel-based BTM system in preventing thermal runaway propagation is also investigated through nail tests on battery packs. In this test, only the top surface battery was penetrated. Two battery packs, 4S1P 3Ah pack and 4S1P 8 Ah pack, were tested under ambient conditions and in the hydrogel system, respectively. Thermocouples were attached at the center of each battery in the pack to record the temperature changes, as shown in Fig. 7.7a.

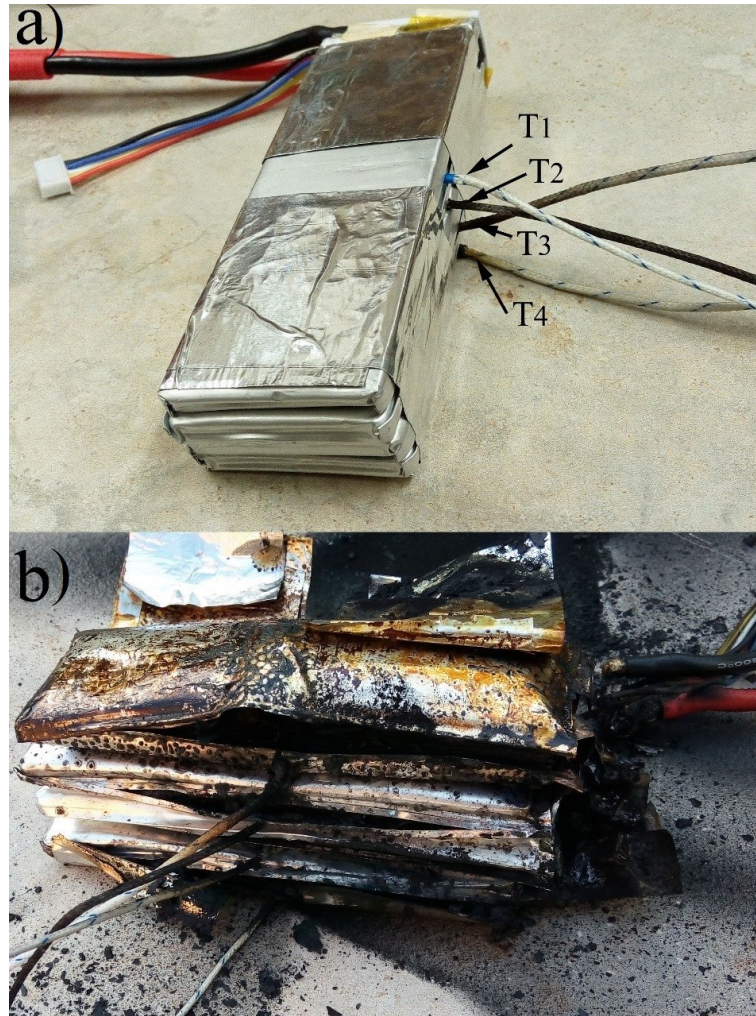


Figure 7.7. Photographs of the 3 Ah battery pack a) before and b) after thermal runaway propagation test.

Fig. 7.8a and b provide the temperature and voltage curves of the 3 Ah battery pack nailed under ambient conditions and the 8 Ah battery pack nailed in the hydrogel system, respectively. After the penetration of the 3 Ah battery pack, thermal runaway occurred at

the surface battery, and its temperature dramatically increased to as high as 344°C. Due to the close contact between the batteries, the heat generated from the first battery was effectively transferred to the second battery and gave rise to its thermal runaway, and the temperature of the second battery soared to 627°C. One after another, all the batteries in the 3 Ah pack went into thermal runaway. A photograph of the 3 Ah battery pack after the thermal runaway propagation is shown in Fig. 7.7b.

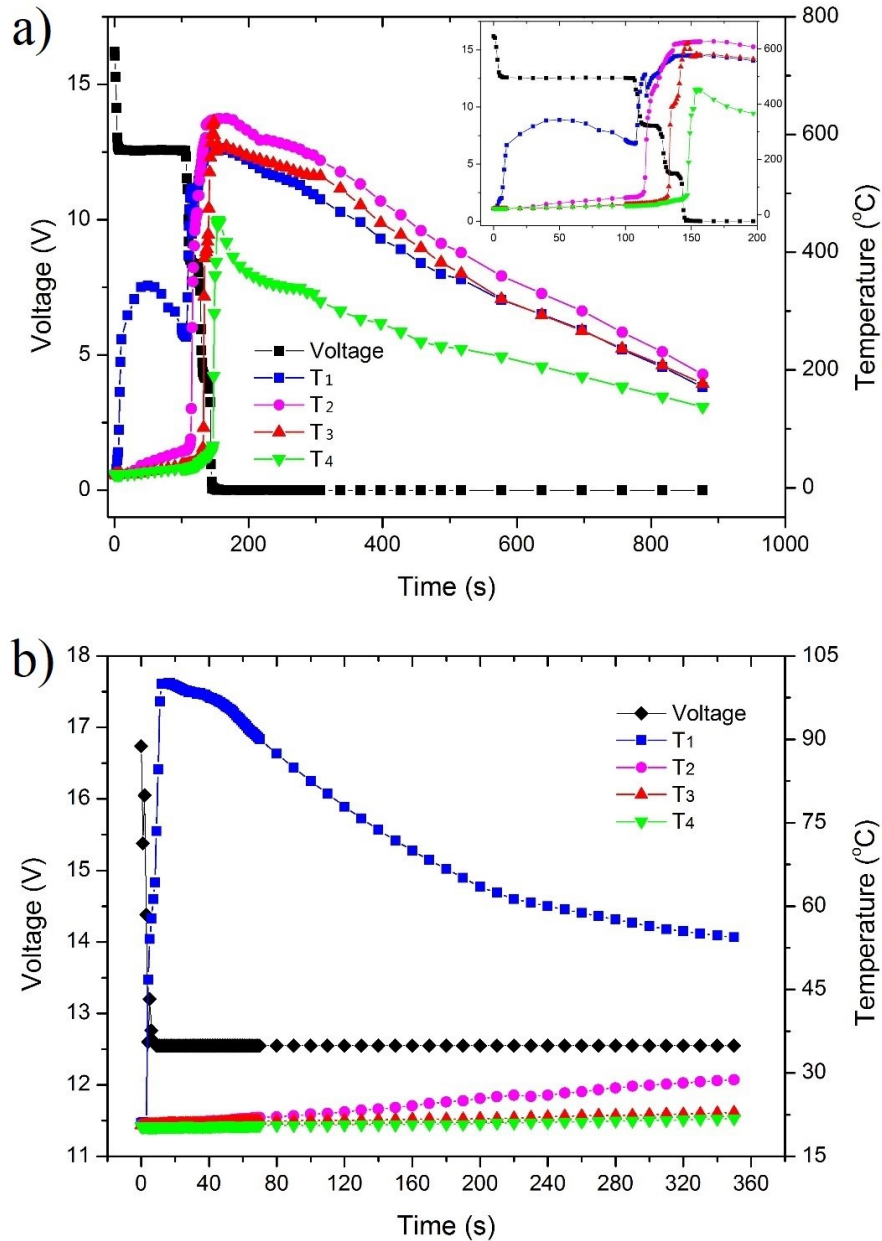


Figure 7.8. Temperature and voltage curves of a) the 3 Ah battery pack nailed in ambient and b) the 8 Ah battery pack nailed in a hydrogel-based BTM system.

The hydrogel-based BTM system effectively prevented the nailed 8 Ah battery pack from thermal runaway propagation. During the test, only the surface battery underwent thermal runaway, and the maximum surface temperature was maintained below 100°C, as shown in Fig. 7.8b. Not only are the safety concerns addressed by the proposed BTM system, the reliability of the entire battery system is improved. The battery pack nailed in the hydrogel retained a higher voltage of 12.58 V after penetration compared to a voltage of 0 V in the 3 Ah battery pack.

In real life applications, retaining moisture in the hydrogel is probably the most critical prerequisite for the BTM system to function properly. To address the evaporation issue, an open structure or a closed structure can be employed. The open structure is designed with a refilling inlet and a venting outlet in the hydrogel system. The inlet enables the hydrogel system to be periodically refilled with water while the outlet allows vapor to vent directly outside, thereby reducing humidity around battery tabs and alleviating relevant safety concerns. In practice, the use of the open structure calls for several important considerations such as hydrogel amount monitoring, determination of refilling frequency, and optimization of size and shape of the inlet and outlet. The complexity involved in implementing such a structure makes it more suitable for large and stationary battery systems, wherein fully automated online supervision systems can be built. As for small-scale and/or mobile applications, a closed structure rather than an open one is more preferred. As the name implies, in a closed structure, the batteries packed with hydrogel cooling systems are completely sealed, excluding the battery tabs left outside.

7.3.3.3 Increase Contact Resistance

In previous simulations, the most abusive conditions were studied, in which polished steel nails were used to induce the internal short circuit. Consequently, high short-circuit currents were produced to generate the concentrated heat at the nail region and finally lead to thermal runaway. In order to prevent thermal runaway, some safety measures could be implemented to create imperfection or bad contact between the nail and electrochemical cells, and thus hindering the current flow. The feasible ways to partially insulate the electrical contact between the nail and electrochemical cells include using flexible

separators or high viscosity protection films. In this section, by proportionally increasing the contact resistance in the penetration model, the feasibility of this method is studied.

Fig. 7.9a shows the maximum temperatures of the 3 Ah and 5 Ah batteries in penetrations using different contact resistances. R_n is the original contact resistance, 29.18 m Ω for 3 Ah battery and 12.3 m Ω for 5 Ah battery, and R_n' represents the modified contact resistance. In the simulations, the value of R_n'/R_n was adjusted from 1 to 200. As can be seen, for both batteries, the increase of the contact resistance can effectively reduce the maximum temperature, for example, a temperature drop from 492°C to 147°C is observed in the 5 Ah battery as the contact resistance increases to 1.459 Ω (50 times the original contact resistance).

Fig. 7.9b-d compares the temperature, voltage, and C-rate curves of the 3 Ah battery in simulations using different contact resistances. As shown in Fig. 7.9c, the voltage has a dramatic drop in the original penetration scenario due to the low contact resistance. Consequently, a high short-circuit current is produced, as can be seen from the black curve in Fig. 7.9d. As a result, all of the battery energy is quickly released, which gives rise to the significant temperature elevation in a very short time. With the increase of the nail contact resistance, the penetration process behaves more like a normal discharge, and the energy stored in the battery can be gradually released at the nail location. For instance, when R_n'/R_n increases to 50, the short-circuit current stays at around 1 C, as shown in Fig. 7.9d. Consequently, the 3 Ah battery can be prevented from thermal runaway, with the maximum temperature kept below 100°C.

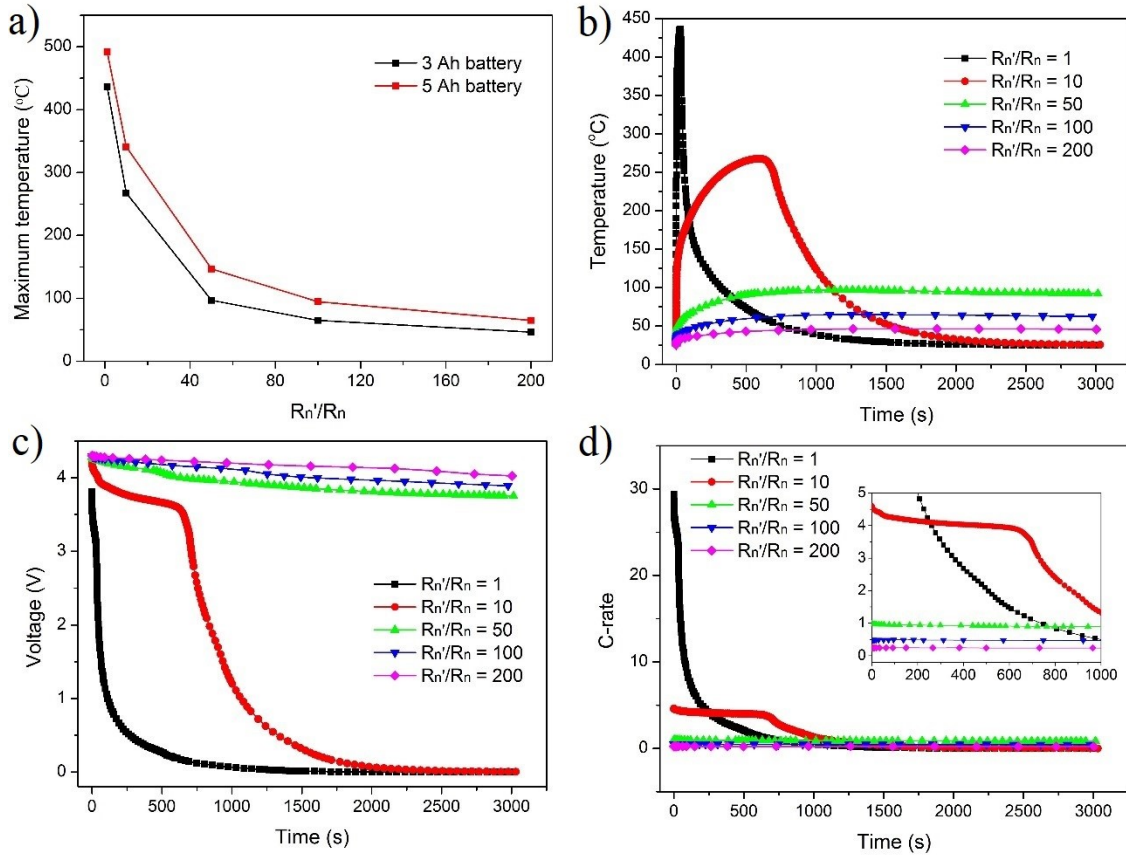


Figure 7.9. a) The maximum temperatures of the 3 Ah and 5 Ah batteries in penetrations using different contact resistances; The b) temperature, c) voltage, and d) C-rate curves of the 3 Ah battery during penetrations using different contact resistances.

7.4 Summary

In this Chapter, the thermal responses of Li-ion batteries in different nail penetration scenarios are studied. An electrochemical-thermal coupling model that incorporates the localized boundary joule heat is employed for simulations.

By adjusting the parameters in the coupling model, simulations are carried out on three commercial Li-ion batteries with capacities of 0.65 Ah, 3 Ah, and 5 Ah. It is found that thermal runaway is prone to occur on high capacity batteries due to the accumulated heat generation at nail locations. It is also observed that the battery internal resistance and the nail diameter have significant influences on the thermal behaviors of Li-ion batteries during nail penetrations. In penetrations with a specific nail size, a lower battery resistance will cause a more severe thermal response. In comparison, penetration of high resistance

batteries with thick nails can shift the accumulated boundary heat generation to a uniform battery heat generation, which is beneficial to battery safety.

Three possible solutions in preventing thermal runaway are also investigated. Although decreasing SOC can reduce the energy stored in the battery, it is unable to eliminate thermal runaway due to the rapid heat generation induced by high voltage. An effective heat dissipation is helpful in cooling the battery surfaces, but it is insufficient to prevent thermal runaway. Nevertheless, an efficient heat transfer can inhibit thermal runaway propagation, as verified experimentally in a hydrogel-based BTM system. Among the solutions, increasing contact resistance is the most effective way in preventing thermal runaway. A high contact resistance can ensure the battery energy slowly releases at the nail region.

Chapter 8. Conclusions and Future Work

8.1 Conclusions

Lithium-ion (Li-ion) batteries have emerged as an important power source for portable devices and electric vehicles due to their excellence over other energy storage technologies. Due to the temperature sensitivity of Li-ion batteries, a uniform temperature distribution and an appropriate operating temperature range are essential for Li-ion batteries to operate properly. Otherwise, the batteries may experience faster capacity fading and even safety issues.

The overheating issues exist in Li-ion batteries during both normal and abnormal discharges. During normal discharges, the battery temperature can be generally maintained within the safe operating temperature range when charge and discharge properly. However, higher operating temperatures within the safe range could shorten the lifespan of Li-ion batteries. For abnormal discharges, the overheating issues are more severe, and the battery temperature can far exceed the safe range, which could give rise to several safety concerns, such as thermal runaway and fire.

The theme of this thesis is to develop robust battery thermal management (BTM) systems to maintain the temperature of both prismatic and cylindrical Li-ion batteries at low levels, as well as to provide techniques to improve the Li-ion battery safety under abnormal operating conditions.

Cylindrical Li-ion batteries are commonly used in pure electric vehicles due to their high energy density, and they tend to operate at low rates. To manage the heat of cylindrical Li-ion batteries, a passive phase change material (PCM)-based internal BTM system is developed. The proposed BTM system embeds a PCM filled core inside the battery to achieve the cooling effect. It is simple in design, and pure PCMs can be directly used in the core, which increases the latent heat of the system and reduces the relevant cost of preparing thermally conductive matrices, which are generally used in PCM-based external BTM systems. Results based on simulation results on 4-layer battery packs showed that the PCM-based internal BTM system consumes less PCM (36.7 % less) and achieves a

lower temperature rise (2.57°C lower) and temperature difference (2.26°C lower) than an external PCM/EG-based BTM system.

The PCM-based internal BTM system can be further improved for better cooling effects. It is found that lower temperature differences can be obtained in battery packs when embedding relatively thicker PCM cores in the interior batteries. Furthermore, the PCM-embedded cylindrical Li-ion batteries have the same external geometry as the original batteries. They can be further integrated with active BTM systems and are ready for operation under some extreme conditions. Simulation results showed that the cooling performance of the hybrid cooling design is significantly improved when compared to an air cooling design, having an 8°C lower peak temperature and 6.1°C lower temperature difference.

Comparatively, prismatic Li-ion batteries are commonly used in hybrid electric vehicles and racing electric vehicles due to their high power density, and they tend to operate at higher rates. In this regard, an active heat pipe-wet cooling combined BTM system is developed for prismatic Li-ion batteries. By attaching ultrathin heat pipes between batteries, the heat generated from the batteries can be efficiently transferred to the condenser side, where water evaporation can quickly dissipate the heat. The proposed BTM system has dramatically improved cooling ability compared to other BTM systems tested. For example, during 3 C rate discharges on a 3 Ah battery pack, the heat pipe-wet cooling combined BTM system achieved 10.3°C and 1.0°C lower peak temperature and temperature difference, respectively, than the heat pipe BTM system cooled by fan only.

Lastly, the overheating issues of abnormally discharged batteries are studied. An electrochemical-thermal coupling model that incorporates localized Joule heating is developed to simulate the thermal responses of Li-ion batteries during short circuits. A contact resistance-contact area plot was obtained experimentally, which can facilitate the process of calculating an accurate localized Joule heat when the battery thickness and nail size is known. The model is proved reliable in predicting the temperature changes of non-thermal runaway batteries and estimating the occurrence and approximate start time of thermal runaway of unsafe batteries.

Among various short circuits, nail penetration is extremely dangerous for Li-ion batteries due to the accumulated heat generation at the nailed region. It is found that thermal runaway is prone to occur on large capacity batteries during nail tests. Besides, the internal resistances of batteries and nail sizes can affect the thermal behaviors of Li-ion batteries during nail penetrations. To suppress thermal runaway and its propagation in battery packs, a hydrogel-based cooling system can be equipped, and the increase of the battery-nail contact resistance is also found to be a feasible approach.

8.2 Future Work

Future work should be conducted on the following subjects:

- 1) The PCM-based internal BTM system should be manufactured inside authentic Li-ion batteries to test their cooling effectiveness.
- 2) The cooling performance of the PCM-based internal BTM system should be tested during abnormal discharge scenarios.
- 3) The core size distribution of the PCM-based internal BTM system should be further optimized through multi-valued decision diagrams.
- 4) The wet cooling process of the heat pipe-based BTM system can be achieved by using automatically controlled water pipes for convenience.
- 5) The effects of relative humidity on the cooling performance of the heat pipe-wet cooling combined BTM system should be studied.
- 6) A numerical model should be developed to simulate the heat pipe-based BTM system, and it should be used to find optimized battery and heat pipe size combinations.
- 7) The developed coupling model should be further modified to simulate more short circuit scenarios, such as pinch tests and crash tests.
- 8) Flexible separators and battery protection films that can form insulation layers between the battery and nail during nail penetrations should be researched.

Bibliography

- [1] Etcheri V, Marom R, Elazari R, Salitra G, Aurbach D. Challenges in the development of advanced Li-ion batteries: a review. *Energy Environ Sci* 2011; 4: 3243-3262.
- [2] Pesaran A, Keyser M, Kim GH, Santhanagopalan S, Smith K. Tools for designing thermal management of batteries in electric drive vehicles. In *Proceedings of Advanced Automotive Battery Conference*. 2013. Pasadena, CA.
- [3] Samadani E, Mastali M, Farhad S, Fraser RA, Fowler M. Li-ion battery performance and degradation in electric vehicles under different usage scenarios. *Int J Energy Res* 2016; 40: 379-392.
- [4] Leng F, Tan CM, Pecht M. Effect of temperature on the aging rate of Li-ion battery operating above room temperature. *Sci Rep* 2015; 5: 12967.
- [5] Zhao R, Zhang S, Liu J, Gu J. A review of thermal performance improving methods of lithium ion battery: Electrode modification and thermal management system. *J Power Sources* 2015; 299: 557-577.
- [6] Park H. A design of air flow configuration for cooling lithium ion battery in hybrid electric vehicles. *J Power Sources* 2013; 239: 30-36
- [7] Shah K, Drake SJ, Wetz DA, Ostanek JK, Miller SP, Heinzl JM, Jain A. Modeling of steady-state convective cooling of cylindrical Li-ion cells. *J Power Sources* 2014; 258: 374-381.
- [8] Yang N, Zhang X, Li G, Hua D. Assessment of the forced air-cooling performance for cylindrical lithium-ion battery packs: A comparative analysis between aligned and staggered cell arrangements. *Appl Therm Eng* 2015; 80: 55-65.
- [9] Wang T, Tseng KJ, Zhao J, Wei Z. Thermal investigation of lithium-ion battery module with different cell arrangement structures and forced air-cooling strategies. *Appl Energy* 2014; 134: 229-238.
- [10] Li X, He F, Ma L. Thermal management of cylindrical batteries investigated using

- wind tunnel testing and computational fluid dynamics simulation. *J Power Sources* 2013; 238: 395-402.
- [11] Huo Y, Rao Z, Liu X, Zhao J. Investigation of power battery thermal management by using mini-channel cold plate. *Energ Convers Manage* 2015; 89: 387-395.
- [12] Wang C, Zhang G, Meng L, Li X, Situ W, Lv Y, Rao M. Liquid cooling based on thermal silica plate for battery thermal management system. *Int J Energy Res.* 2017; 41: 2468-2479.
- [13] Zhang S, Zhao R, Liu J, Gu J. Investigation on a hydrogel based passive thermal management system for lithium ion batteries. *Energy* 2014; 68: 854-861.
- [14] Chen K, Li X. Accurate determination of battery discharge characteristics – A comparison between two battery temperature control methods. *J Power Sources* 2014; 247: 961-966.
- [15] Zhao R, Zhang S, Gu J, Liu J, Carkner S, Lanoue E. An experimental study of lithium ion battery thermal management using flexible hydrogel films. *J Power Sources* 2014; 255: 29-36.
- [16] Al-Hallaj S, Selman JR. A novel thermal management system for electric vehicle batteries using phase-change material. *J Electrochem Soc* 2000; 147: 3231-3236.
- [17] Zhang X, Kong X, Li G, Li J. Thermodynamic assessment of active cooling/heating methods for lithium-ion batteries of electric vehicles in extreme conditions. *Energy* 2014; 64: 1092-1101.
- [18] Mills A, Farid M, Selman JR, Al-Hallaj S. Thermal conductivity enhancement of phase change materials using a graphite matrix. *Appl Therm Eng* 2006; 26: 1652-1661.
- [19] Wang Z, Zhang Z, Li J, Yang L. Paraffin and paraffin/aluminum foam composite phase change material heat storage experimental study based on thermal management of Li-ion battery. *Appl Therm Eng* 2015; 78: 428-436.
- [20] Samimi F, Babapoor A, Azizi M, Karimi G. Thermal management analysis of a Li-

- ion battery cell using phase change material loaded with carbon fibers. *Energy* 2016; 96: 355-371.
- [21] Wu MS, Liu KH, Wang YY, Wan CC. Heat dissipation design for lithium-ion batteries. *J Power Sources* 2002; 109: 160-166.
- [22] Tran TH, Harmand S, Desmet B, Filangi S. Experimental investigation on the feasibility of heat pipe cooling for HEV/EV lithium-ion battery. *Appl Therm Eng* 2014; 63: 551-558.
- [23] Rao Z, Wang S, Wu M, Lin Z, Li F. Experimental investigation on thermal management of electric vehicle battery with heat pipe. *Energy Convers Manage* 2013; 65: 92-97.
- [24] Malik M, Dincer I, Rosen M, Fowler M. Experimental investigation of a new passive thermal management system for a Li-ion battery pack using phase change composite material. *Electrochim. Acta* 2017; 257: 345-355.
- [25] Xie Y, Tang J, Shi S, Xing Y, Wu H, Hu Z, Wen D. Experimental and numerical investigation on integrated thermal management for lithium-ion battery pack with composite phase change materials. *Energy Convers Manag* 2017; 154: 562-575.
- [26] Kim D, Jung J, Kim Y, Lee M, Seo J, Khan SB. Structure and thermal properties of octadecane/expanded graphite composites as shape-stabilized phase change materials. *Int J Heat Mass Transfer* 2016; 96: 735-741.
- [27] Jiang G, Huang J, Fu Y, Cao M, Liu M. Thermal optimization of composite phase change material/expanded graphite for Li-ion battery thermal management. *Appl Therm Eng* 2016; 108: 1119-1125.
- [28] Wu MS, Chiang PCJ, Lin JC, Jan YS. Correlation between electrochemical characteristics and thermal stability of advanced lithium-ion batteries in abuse tests-short-circuit tests. *Electrochim Acta* 2004; 49: 1803-12.
- [29] Lamb J, Orendorff CJ. Evaluation of mechanical abuse techniques in lithium ion batteries. *J Power Sources* 2014; 247: 189-96.

- [30] Lamb J, Orendorff CJ, Steele LAM, Spangler SW. Failure propagation in multi-cell lithium ion batteries. *J Power Sources* 2015; 283: 517-23.
- [31] Feng X, He X, Ouyang M, Lu L, Wu P, Kulp C, Prasser S. Thermal runaway propagation model for designing a safer battery pack with 25 Ah $\text{LiNi}_x\text{Co}_y\text{Mn}_z\text{O}_2$ large format lithium ion battery. *Appl Energy* 2015; 154: 74-91.
- [32] Feng X, Lu L, Ouyang M, Li J, He X. A 3D thermal runaway propagation model for a large format lithium ion battery module. *Energy* 2016; 115: 194-208.
- [33] Liu YH, Okano M, Mukai T, Inoue K, Yanagida M, Sakai T. Improvement of thermal stability and safety of lithium ion battery using SiO anode material. *J Power Sources* 2016; 304: 9-14.
- [34] Matsumoto K, Inoue K, Utsugi K. A highly safe battery with non-flammable triethyl-phosphate-based electrolyte. *J Power Sources* 2015; 273: 954-8.
- [35] Hatchard TD, MacNeil DD, Basu A, Dahn JR. Thermal model of cylindrical and prismatic lithium-ion cells. *J Electrochem Soc* 2001; 148: A755-61.
- [36] Zhang C, Santhanagopalan S, Sprague MA, Pesaran AA. Coupled mechanical-electrical-thermal modeling for short-circuit prediction in a lithium-ion cell under mechanical abuse. *J Power Sources* 2015; 290: 102-13.
- [37] Kim GH, Pesaran AA, Spotnitz RM. A three-dimensional thermal abuse model for lithium-ion cells. *J Power Sources* 2007; 170: 476-89.
- [38] Guo G, Long B, Cheng B, Zhou S, Xu P, Cao B. Three-dimensional thermal finite element modeling of lithium-ion battery in thermal abuse application. *J Power Sources* 2010; 195: 2393-8.
- [39] Spotnitz RM, Weaver J, Yeduvaka G, Doughty DH, Roth EP. Simulation of abuse tolerance of lithium-ion battery packs. *J Power Sources* 2007; 163: 1080-6.
- [40] Zhao R, Liu J, Gu J. Simulation and experimental study on lithium ion battery short circuit. *Appl Energy* 2016; 173: 29-39.
- [41] Zavalis TG, Behm M, Lindbergh G. Investigation of short-circuit scenarios in a

- lithium-ion battery cell. *J Electrochem Soc* 2012; 159: A848-59.
- [42] Chiu KC, Lin CH, Yeh SF, Lin YH, Chen KC. An electrochemical modeling of lithium-ion battery nail penetration. *J Power Sources* 2014; 251: 254-63.
- [43] Zhao W, Luo G, Wang CY. Modeling nail penetration process in large-format Li-ion cells. *J Electrochem Soc* 2015; 162: A207-17.
- [44] Xu M, Zhang Z, Wang X, Jia L, Yang L. A pseudo three-dimensional electrochemical-thermal model of a prismatic LiFePO₄ battery during discharge process. *Energy* 2015; 80: 303-317.
- [45] Xu M, Zhang Z, Wang X, Jia L, Yang L. Two-dimensional electrochemical-thermal coupled modeling of cylindrical LiFePO₄ batteries. *J Power Sources* 2014; 256: 233-243.
- [46] Inui Y, Kobayashi Y, Watanabe Y, Watase Y, Kitamura Y. Simulation of temperature distribution in cylindrical and prismatic lithium ion secondary batteries. *Energy Convers Manage* 2007; 48: 2103-2109.
- [47] Hu H, Argyropoulos SA. Mathematical modeling of solidification and melting: a review. *Model Simul Mater Eng* 1996; 4: 371-396.
- [48] Bandhauer TM, Garimella S, Fuller TF. A critical review of thermal issues in lithium-ion batteries. *J Electrochem Soc* 2011; 158: R1-R25.
- [49] Bernardi D, Pawlikowski E, Newman J. A general energy balance for battery systems. *J Electrochem Soc* 1985; 132: 5-12.
- [50] Gu WB, Wang CY. Thermal-electrochemical modeling of battery systems. *J Electrochem Soc* 2000; 147: 2910-2922.
- [51] Zhao R, Gu J, Liu J. An investigation on the significance of reversible heat to the thermal behavior of lithium ion battery through simulations. *J Power Sources* 2014; 266: 422-432.
- [52] Srinivasan V, Wang CY. Analysis of electrochemical and thermal behavior of Li-ion cells. *J Electrochem Soc* 2003; 150: A98-A106.

- [53] Zhao R, Liu J, Gu J. The effects of electrode thickness on the electrochemical and thermal characteristics of lithium ion battery. *Appl Energy* 2015; 139: 220-229
- [54] Vetter J, Novak P, Wagner MR, Veit C, Moller KC, Besenhard JO, Winter M, Wohlfahrt-Mehrens M, Vogler C, Hammouche A. Ageing mechanisms in lithium-ion batteries. *J Power Sources* 2005; 147: 269-281.
- [55] Kim JH, Pieczonka NPW, Li Z, Wu Y, Harris S, Powell BR. Understanding the capacity fading mechanism in $\text{LiNi}_{0.5}\text{Mn}_{1.5}\text{O}_4$ /graphite Li-ion batteries. *Electrochimica Acta* 2013; 90: 556-562.
- [56] Markovsky B, Rodkin A, Cohen YS, Palchik O, Levi E, Aurbach D, Kim HJ, Schmidt M. The study of capacity fading processes of Li-ion batteries: major factors that play a role. *J Power Sources* 2003; 119: 504-510.
- [57] Goers D, Spahr ME, Leone A, Markle W, Novak P. The influence of the local current density on the electrochemical exfoliation of graphite in lithium-ion battery negative electrodes. *Electrochimica Acta* 2011; 56: 3799-3808.
- [58] Liu P, Wang J, Hicks-Garner J, Sherman E, Soukiazian S, Verbrugge M, Tataria H, Musser J, Finamore P. Ageing mechanisms of LiFePO_4 batteries deduced by electrochemical and structural analyses. *J Electrochem Soc* 2010; 157: A499- A507.
- [59] Shim J, KostECKI R, Richardson T, Song X, StriEBel KA. Electrochemical analysis for cycle performance and capacity fading of a lithium-ion battery cycled at elevated temperatures. *J Power Sources* 2002; 112: 222-230.
- [60] Tan L, Zhang L, Sun Q, Shen M, Qu Q, Zheng H. Capacity loss induced by lithium deposition at graphite anode for LiFePO_4 /graphite cell cycling at different temperatures. *Electrochimica Acta* 2013; 111: 802-808.
- [61] Ramadass P, Haran B, White RE, Popov BN. Mathematical modeling of the capacity fade of Li-ion cells. *J Power Sources* 2003; 123: 230-240.
- [62] Santhanagopalan S, Zhang Q, Kumaresan K, White RE. Parameter estimation and life modeling of lithium-ion cells. *J Electrochem Soc* 2008; 155: A345-A353.

- [63] Doi T, Inaba M, Tsuchiya H, Jeong SK, Iriyama Y, Abe T, Ogumi Z. Electrochemical AFM study of LiMn_2O_4 thin film electrodes exposed to elevated temperatures. *J Power Sources* 2008; 180: 539-545.
- [64] Zhao J, Wang Y. Atomic layer deposition of epitaxial ZrO_2 coating on LiMn_2O_4 nanoparticles for high-rate lithium ion batteries at elevated temperature. *Nano Energy* 2013; 2: 882-889.
- [65] Chang HH, Chang CC, Su CY, Wu HC, Yang MH, Wu NL. Effects of TiO_2 coating on high-temperature cycle performance of LiFePO_4 -based lithium-ion batteries. *J Power Sources* 2008; 185: 466-472.
- [66] Deng B, Nakamura H, Yoshio M. Capacity fading with oxygen loss for manganese spinels upon cycling at elevated temperatures. *J Power Sources* 2008; 180: 864-868.
- [67] Fan L, Khodadadi JM, Pesaran A. A parametric study on thermal management of an air-cooled lithium-ion battery module for plug-in hybrid electric vehicles. *J Power Sources* 2013; 238: 301-312.
- [68] Xun J, Liu R, Jiao K. Numerical and analytical modeling of lithium ion battery thermal behaviors with different cooling designs. *J Power Sources* 2013; 233: 47-61.
- [69] Mahamud R, Park C. Reciprocating air flow for Li-ion battery thermal management to improve temperature uniformity. *J Power Sources* 2011; 196: 5685-5696.
- [70] Yu K, Yang X, Cheng Y, Li C. Thermal analysis and two-dimensional air flow thermal management for lithium-ion battery pack. *J Power Sources* 2014; 270: 193-200.
- [71] Sun H, Dixon R. Development of cooling strategy for an air-cooled lithium-ion battery pack. *J Power Sources* 2014; 272: 404-414.
- [72] Liu Z, Wang Y, Zhang J, Liu Z. Shortcut computation for the thermal management of a large air-cooled battery pack. *Appl Therm Eng* 2014; 66: 445-452.
- [73] Xu XM, He R. Research on the heat dissipation performance of battery pack based

- on forced air cooling. *J Power Sources* 2013; 240: 33-41.
- [74] Giuliano MR, Prasad AK, Advani SG. Experimental study of an air-cooled thermal management system for high capacity lithium-titanate batteries. *J Power Sources* 2012; 2016: 345-352.
- [75] Pesaran AA. Battery thermal management in EVs and HEVs: Issues and Solutions. *Advanced Automotive Battery Conference*. 2001. Las Vegas, Nevada.
- [76] Zhang T, Gao C, Gao Q, Wang G, Liu M, Guo Y, Xiao C, Yan YY. Status and development of electric vehicle integrated thermal management from BTM to HVAC. *Appl Therm Eng* 2015; 88: 398-409.
- [77] Jin LW, Lee PS, Kong XX, Fan Y, Chou SK. Ultra-thin mini-channel LCP for EV battery thermal management. *Appl Energy* 2014; 113: 1786-1794.
- [78] Jarrett A, Kim IY. Influence of operating conditions on the optimum design of electric vehicle battery cooling plates. *J Power Sources* 2014; 245: 644-655.
- [79] Jarrett A, Kim IY. Design optimization of electric vehicle battery cooling plates for thermal performance. *J Power Sources* 2011; 196: 10359-10368.
- [80] Bandhauer TM, Garimella S. Passive, internal thermal management system for batteries using microscale liquid-vapor phase change. *Appl Therm Eng* 2013; 61: 756-769.
- [81] Tong W, Somasundaram K, Birgersson E, Mujumdar AS, Yap C. Numerical investigation of water cooling for a lithium-ion bipolar battery pack. *Int J Therm Sci* 2015; 94: 259-269.
- [82] Nieto N, Diaz L, Gastelurrutia J, Blanco F, Ramos JC, Rivas A. Novel thermal management system design methodology for power lithium-ion battery. *J Power Sources* 2014; 272: 291-302.
- [83] Hirano H, Tajima T, Hasegawa T, Hasegawa T, Sekiguchi T, Uchino M. Boiling liquid battery cooling for electric vehicle. *ITEC Asia-Pacific*. 2014. Beijing.
- [84] van Gils RW, Danilov D, Notten PHL, Speetjens MFM, Nijmeijer H. Battery

- thermal management by boiling heat-transfer. *Energ Convers Manage* 2014; 79: 9-17.
- [85] Karimi G, Dehghan AR. Thermal management analysis of a lithium-ion battery pack using flow network approach. *Int J Mech Eng Mechatron* 2012; 1: 88-94.
- [86] Gaugler RS. Heat transfer device. 1944. US2350348A.
- [87] Zhao R, Gu J, Liu J. An experimental study of heat pipe thermal management system with wet cooling method for lithium ion batteries. *J Power Sources* 2015; 273: 1089-1097.
- [88] Rao Z, Huo Y, Liu X. Experimental study of an OHP-cooled thermal management system for electric vehicle power battery. *Exp Therm Fluid Sci* 2014; 57: 20-26.
- [89] Tran TH, Harmand S, Sahut B. Experimental investigation on heat pipe for hybrid electric vehicle and electric vehicle lithium-ion battery. *J Power Sources* 2014; 265: 262-272.
- [90] Wang Q, Jiang B, Xue QF, Sun HL, Li B, Zou HM, Yan YY. Experimental investigation on EV battery cooling and heating by heat pipes. *Appl Therm Eng* 2015; 88: 54-60.
- [91] Burban G, Ayel V, Alexandre A, Lagonotte P, Bertin Y, Romestant C. Experimental investigation of a pulsating heat pipe for hybrid vehicle applications. *Appl Therm Eng* 2013; 50: 94-103.
- [92] Greco A, Cao D, Jiang X, Yang H. A theoretical and computational study of lithium-ion battery thermal management for electric vehicles using heat pipes. *J Power Sources* 2014; 257: 344-355.
- [93] Zalba B, Marin JM, Cabeza LF, Mehling H. Review on thermal energy storage with phase change: materials, heat transfer analysis and applications. *Appl Therm Eng* 2003; 23: 251-283.
- [94] Sharma A, Tyagi VV, Chen CR, Buddhi D. Review on thermal energy storage with phase change materials and applications. *Renew Sust Energ Rev* 2009; 13: 318-345.

- [95] Zhou D, Zhao CY, Tian Y. Review on thermal energy storage with phase change materials (PCMs) in building applications. *Appl Energy* 2012; 92: 593-605.
- [96] Waqas A, Din Zu. phase change material (PCM) storage for free cooling of buildings-A review *Renew Sust Energ Rev* 2013; 18: 607-625.
- [97] Khudhair AM, Farid MM. A review on energy conservation in building applications with thermal storage by latent heat using phase change materials. *Energ Convers Manage* 2004; 45: 263-275.
- [98] Al-Hallaj S, Selman JR. Thermal modeling of secondary lithium batteries for electric vehicle/hybrid electric vehicle applications. *J Power Sources* 2002; 110: 341-348.
- [99] Ramandi MY, Dincer I, Naterer GF. Heat transfer and thermal management of electric vehicle batteries with phase change materials. *Heat Mass Transfer* 2011; 47: 777-788.
- [100] Khateeb SA, Amiruddin S, Farid MM, Selman JR, Al-Hallaj S. Thermal management of Li-ion battery with phase change material for electric scooters: experimental validation. *J Power Sources* 2005; 142: 345-353.
- [101] Li WQ, Qu ZG, He YL, Tao YB. Experimental study of a passive thermal management system for high-powered lithium ion batteries using porous metal foam saturated with phase change materials. *J Power Sources* 2014; 255: 9-15.
- [102] Khateeb SA, Farid MM, Selman JR, Al-Hallaj S. Design and simulation of a lithium-ion battery with a phase change material thermal management system for an electric scooter. *J Power Sources* 2004; 128: 292-307.
- [103] Qu ZG, Li WQ, Tao WQ. Numerical model of the passive thermal management system for high-power lithium ion battery by using porous metal foam saturated with phase change material. *Int J Hydrogen Energy* 2014; 39: 3904-3913.
- [104] Goli P, Legedza S, Dhar A, Salgado R, Renteria J, Balandin AA. Graphene-enhanced hybrid phase change materials for thermal management of Li-ion batteries. *J Power Sources* 2014; 248: 37-43.

- [105] Babapoor A, Azizi M, Karimi G. Thermal management of a Li-ion battery using carbon fiber-PCM composites. *Appl Therm Eng* 2015; 82: 281-290.
- [106] Jiang G, Huang J, Liu M, Cao M. Experiment and simulation of thermal management for a tube-shell Li-ion battery pack with composite phase change material. *Appl Therm Eng* 2017; 120: 1-9.
- [107] Ling Z, Wang F, Fang X, Gao X, Zhang Z. A hybrid thermal management system for lithium ion batteries combining phase change materials with forced-air cooling. *Appl Energy* 2015; 148: 403-409.
- [108] Hemery CV, Par F, Robin JF, Marty P. Experimental performances of a battery thermal management system using a phase change material. *J Power Sources* 2014; 270: 349-358.
- [109] Javani N, Dincer I, Naterer GF, Yilbas BS. Heat transfer and thermal management with PCMs in a Li-ion battery cell for electric vehicles. *Int J Heat Mass Transfer* 2014; 72: 690-703.
- [110] Mills A, Al-Hallaj S. Simulation of passive thermal management system for lithium-ion battery packs. *J Power Sources* 2005; 141: 307-315.
- [111] Kizilel R, Sabbah R, Selman JR, Al-Hallaj S. An alternative cooling system to enhance the safety of Li-ion battery packs. *J Power Sources* 2009; 194: 1105-1112.
- [112] Lin C, Xu S, Chang G, Liu J. Experiment and simulation of a LiFePO₄ battery pack with a passive thermal management system using composite phase change material and graphite sheets. *J Power Sources* 2015; 275: 742-749.
- [113] Doughty D, Roth EP. A general discussion of Li-ion battery safety. *Electrochem Soc Interface* 2012; 21: 37-44.
- [114] Kitoh K, Nemoto H. 100 Wh Large size Li-ion batteries and safety tests. *J Power Sources* 1999; 81-82: 887-890.
- [115] Zeng Y, Wu K, Wang D, Wang Z, Chen L. Overcharge investigation of lithium-ion polymer batteries. *J Power Sources* 2006; 160: 1302-1307.

- [116] Leising RA, Palazzo MJ, Takeuchi ES, Takeuchi KJ. A study of the overcharge reaction of lithium-ion batteries. *J Power Sources* 2001; 97-98: 681-683.
- [117] Maleki H, Howard JN. Internal short circuit in Li-ion cells. *J Power Sources* 2009; 191: 568-574.
- [118] Cai W, Wang H, Maleki H, Howard JN, Lara-Curzio E. Experimental simulation of internal short circuit in Li-ion and Li-ion-polymer cells. *J Power Sources* 2011; 196: 7779-7783.
- [119] Matsumoto K, Martinez M, Gutel T, Mailley S, De vito E, Patoux S, Inoue K, Utsugi K. Stability of trimethyl phosphate non-flammable based electrolyte on the high voltage cathode (LiNi_{0.5}Mn_{1.5}O₄). *J Power Sources* 2015; 273: 1084-1088.
- [120] Lombardo L, Brutti S, Navarra MA, Panero S, Reale P. Mixtures of ionic liquid – alkylcarbonates as electrolytes for safe lithium-ion batteries. *J Power Sources* 2013; 227: 8-14.
- [121] Matsumoto K, Inoue K, Utsugi K. A highly safe battery with a non-flammable triethyl-phosphate-based electrolyte. *J Power Sources* 2015; 273: 954-958.
- [122] Benmayza A, Lu W, Ramani V, Prakash J. Electrochemical and Thermal Studies of LiNi_{0.8}Co_{0.15}Al_{0.05}O₂ under Fluorinated Electrolytes. *Electrochimica Acta* 2014; 123: 7-13.
- [123] Feng J, Lu L. A novel bifunctional additive for safer lithium ion batteries. *J Power Sources* 2013; 243: 29-32.
- [124] Belov DG, Shieh DT. A study of tetrabromobisphenol A (TBBA) as a flame retardant additive for Li-ion battery electrolytes. *J Power Sources* 2014; 247: 865-875.
- [125] Wu B, Pei F, Wu Y, Mao R, Ai X, Yang H, Cao Y. An electrochemically compatible and flame-retardant electrolyte additive for safe lithium ion batteries. *J Power Sources* 2013; 227: 106-110.
- [126] Zeng Z, Jiang X, Wu B, Xiao L, Ai X, Yang H, Cao Y. Bis(2,2,2-trifluoroethyl)

- methylphosphonate: An Novel Flame-retardant Additive for Safe Lithium-ion Battery. *Electrochimica Acta* 2014; 129: 300-304.
- [127] Feng J, Ma P, Yang H, Lu L. Understanding the interactions of phosphonate-based flame-retarding additives with graphitic anode for lithium ion batteries. *Electrochimica Acta* 2013; 114: 688-692.
- [128] Chen YS, Hu CC, Li YY. The importance of heat evolution during the overcharge process and the protection mechanism of electrolyte additives for prismatic lithium ion batteries. *J Power Sources* 2008; 181: 69-73.
- [129] Kim CS, Yoo JS, Jeong KM, Kim K, Yi CW. Investigation on internal short circuits of lithium polymer batteries with a ceramic-coated separator during nail penetration. *J Power Sources* 2015; 289: 41-49.
- [130] Kim M, Park JH. Inorganic thin layer coated porous separator with high thermal stability for safety reinforced Li-ion battery. *J Power Sources* 2012; 212: 22-27.
- [131] Woo JJ, Nam SH, Seo SJ, Yun SH, Kim WB, Xu T, Moon SH. A flame retarding separator with improved thermal stability for safe lithium-ion batteries. *Electrochem Commun* 2013; 35: 68-71.
- [132] Yeon D, Lee Y, Ryou MH, Lee YM. New flame-retardant composite separators based on metal hydroxides for lithium-ion batteries. *Electrochimica Acta* 2015; 157: 282-289.
- [133] Golubkov AW, Fuchs D, Wagner J, Wiltsche H, Stangl C, Fauler G, Voitic G, Thaler A, Hacker V. Thermal-runaway experiments on consumer Li-ion batteries with metal-oxide and olivin-type cathodes. *RSC Advances* 2014; 4: 3633-3642.
- [134] Jhu CY, Wang YW, Wen CY, Shu CM. Thermal runaway potential of LiCoO_2 and $\text{Li}(\text{Ni}_{1/3}\text{Co}_{1/3}\text{Mn}_{1/3})\text{O}_2$ batteries determined with adiabatic calorimetry methodology. *Appl Energy* 2012; 100: 127-131.
- [135] Gnanaraj JS, Zinigrad E, Asraf L, Gottlieb HE, Sprecher M, Schmidt M, Geissler W, Aurbach D. A detailed investigation of the thermal reactions of LiPF_6 solution in organic carbonates using ARC and DSC. *J Electrochem Soc* 2003; 150: A1533-

A1537.

- [136] Roth EP, Doughty DH. Thermal abuse performance of high-power 18650 Li-ion cells. *J Power Sources* 2004; 128: 308-318.
- [137] Roth EP. Abuse Response of 18650 Li-Ion Cells with Different Cathodes Using EC:EMC/LiPF₆ and EC:PC:DMC/LiPF₆ Electrolytes. *ECS Transactions* 2008; 11: 19-41.
- [138] Mendoza-Hernandez OS, Ishikawa H, Nishikawa Y, Maruyama Y, Umeda M. Cathode material comparison of thermal runaway behavior of Li-ion cells at different state of charges including over charge. *J Power Sources* 2015; 280: 499-504.
- [139] Vélez C, Khayet M, Ortiz de Zárate JM. Temperature-dependent thermal properties of solid/liquid phase change even-numbered n-alkanes: n-Hexadecane, n-octadecane and n-eicosane. *Appl. Energy* 2015; 143: 383-394.
- [140] Shah K, Mckee C, Chalise D, Jain A. Experimental and numerical investigation of core cooling of Li-ion cells using heat pipes. *Energy* 2016; 113: 852-860.
- [141] He F, Ma L. Thermal management of batteries employing active temperature control and reciprocating cooling flow. *Int J Heat Mass Transfer* 2015; 83: 164-172.
- [142] Tang H, Tang Y, Wan Z, Li J, Yuan W, Lu L, Li Y, Tang K. Review of applications and developments of ultra-thin micro heat pipes for electronic cooling. *Appl Energy* 2018; 223: 383-400.
- [143] Hong JS, Maleki H, Al-Hallaj S, Redey L, Selman JR. Electrochemical-calorimetric studies of lithium-ion cells. *J Electrochem Soc* 1998; 145: 1489-1501.
- [144] Smith K, Wang CY. Power and thermal characterization of a lithium-ion battery pack for hybrid-electric vehicles. *J Power Sources* 2006; 160: 662-673.
- [145] Kumaresan K, Sikha G, White RE. Thermal model for a Li-ion cell. *J Electrochem Soc* 2008; 155: A164-A171.
- [146] Hennige V, Hying C, Hoerpel G. Lithium battery separator having a shutdown

function. 2002. US7691529B2.